Mean Motion Resonances in a Resonance Lock

Stability and Evolution

Danny Gasman

Technische Universiteit Delft

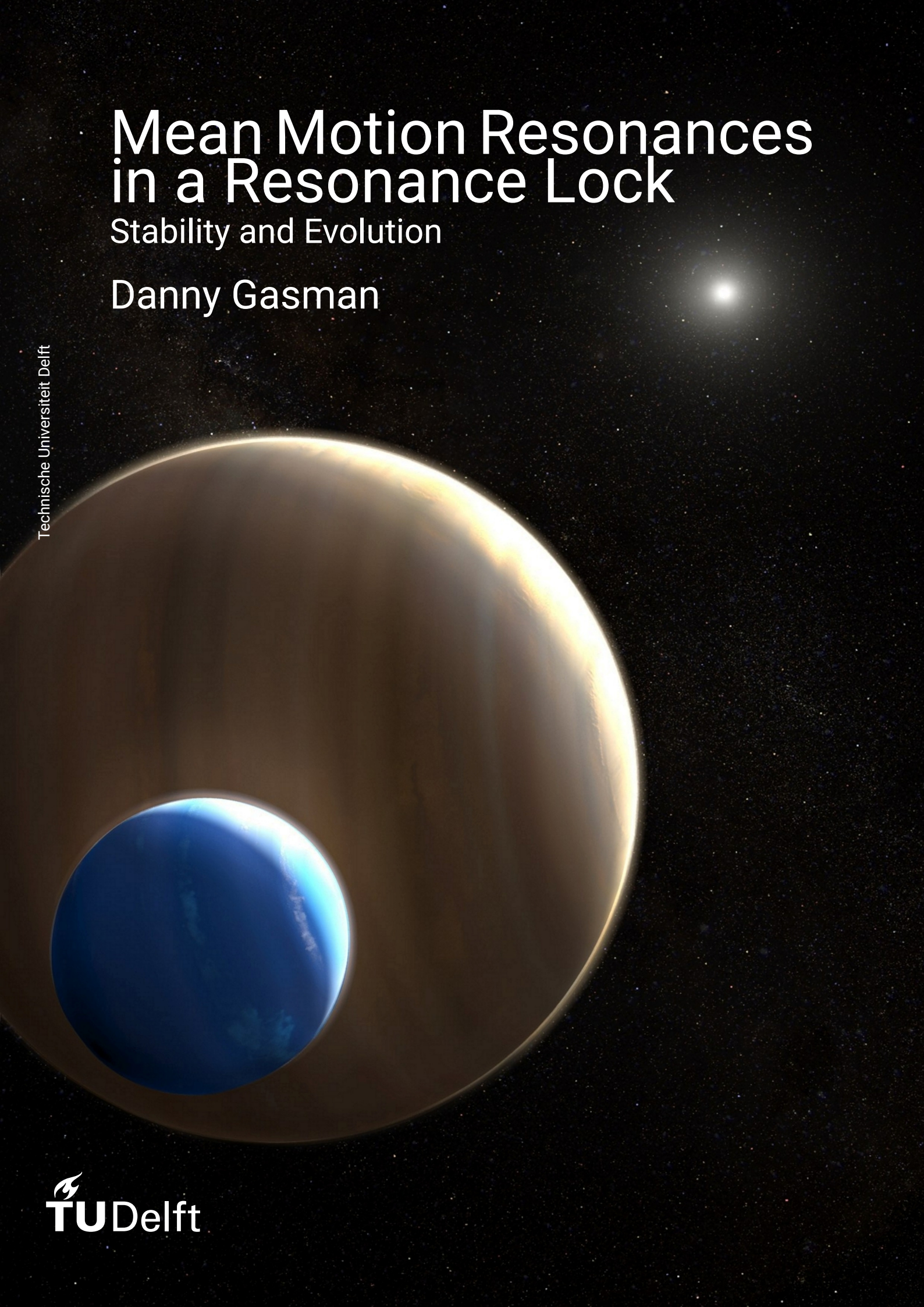

TU Delft

Mean Motion Resonances in a Resonance Lock

Stability and Evolution

by

Danny Gasman

to obtain the degree of Master of Science
at the Delft University of Technology.

Cover image from https:
//sci.esa.int/web/hubble/-/60712-exomoon-orbiting-its-planet-artists-impression

Student number: 4537351
Project duration: 26 October, 2020 – 27 August, 2021
Thesis committee: Dr. S.M. Cazaux, Committee chair
Dr. ir. D. Dirkx, Supervisor
Dr. A. Menicucci, External examinator
E. Kleisioti (MSc), Additional examinator

TU Delft

Abstract

The combined effects of tidal dissipation and mean motion resonances (MMRs) have widely been employed in attempts to explain orbital and surface features of a variety of Solar System moons. While a range of features and mechanisms can be attributed to these two processes, the specific conditions are often still up for debate, and for some features no plausible explanation has been found yet. All of the past models and evolution scenarios have until recently assumed a constant planetary quality factor Q, that characterises migration and dampening of the eccentricity. However, recent observations support the theory that this parameter is not constant. This theory describes steep dips in Q_p or peaks in $|\mathrm{Im}(k_{2,p})|$ at different tidal frequencies that evolve in time, allowing a satellite to evolve along with them: resonance locking. Therefore, in this thesis a model is developed that includes this new mechanism, such that its influence on the behaviour of moons can be examined.

The model developed is an orbital evolution model, accurate up to fourth-order in eccentricity, and assumes the orbits are not inclined. By doing so, the 2:1 and 3:1 MMRs are supported. The resonance locking mechanism is included as a narrow bell-curve, allowing for the $|\mathrm{Im}(k_{2,p})|$ to be calculated as the frequency changes. The properties of the peak were changed to examine its effects on the evolution of the two moons in resonance. For the 2:1 resonance sets of nine different initial conditions were used, while for the 3:1 resonance four different sets were studied. The conditions required to lock with the peak were identified, as well as the strength of the wave required to break the MMRs. Finally, some sets were integrated for a longer period of time, to study the long term effects.

It was found that the resonance locking mechanism in combination with an MMR can greatly increase the eccentricity of the moons' orbits, therefore causing a period of increased tidal heating. It could therefore provide an alternative explanation to some of the inexplicable features of Solar System moons, such as the high free eccentricity of Ganymede or Titan, but more specific studies for real systems should be conducted to confirm this per moon. Furthermore, the MMRs in our Solar System were likely not broken due to a resonance lock in the past. Data from future missions must be applied to current gas giant interior models to better constrain the mode characteristics.

Preface

Between graduating during the COVID-19 pandemic and catching said illness during this time, it has definitely been an eventful year. Keeping up morale would not have been possible without my friends and family, who convinced me to enjoy life outside of my thesis work from time to time. I would also like to thank Dominic and Marc, for their useful discussions and feedback throughout the process.

Contents

Nomenclature

List of Abbreviations

JUICE	JUpiter ICy moons Explorer
MMR	Mean Motion Resonance

List of Symbols

α	Fraction of semi-major axes
α	Ratio of semi-major axes
$\dot{\theta}_p$	Rotation rate of planet
$\dot{\theta}_p$	Rotation rate of primary
$\dot{\theta}_s$	Rotation rate of satellite
η_S	Maxwell viscosity
λ	Mean longitude of inner satellite
λ'	Mean longitude of outer satellite
$\mathscr{R}$	Disturbing function of inner satellite
$\mathscr{R}'$	Disturbing function of outer satellite
$\mathscr{R}_D$	Direct part of the disturbing function
$\mathscr{R}_E$	External indirect part of the disturbing function
$\mathscr{R}_I$	Internal indirect part of the disturbing function
μ	Gravitational parameter of (inner) satellite
μ'	Gravitational parameter of outer satellite
μ_p	Gravitational parameter of primary
ω	Forcing frequency
ω_α	Frequency of centre of the peak
ω_σ	Width of peak
$\phi_{2:1,1}$	Resonant angle inner 2:1 MMR
$\phi_{2:1,2}$	Resonant angle outer 2:1 MMR
$\phi_{3:1}$	Resonant angle 3:1 MMR
ρ_p	Density planet
ρ_s	Density satellite
τ_e	Eccentricity damping timescale
τ_n	Orbital migration timescale
$\tilde{\mu}$	Effective rigidity
$\tilde{\omega}$	Longitude of pericentre of inner satellite
$\tilde{\omega}'$	Longitude of pericentre of outer satellite
$\tilde{t}$	Model time
a	Semi-major axis of (inner) satellite
a'	Semi-major axis of outer satellite
A_n	Amplitude of mean motion
$b_s^{(j)}$	Laplace coefficient
C	Scaling factor
D	Differential operator
e	Eccentricity of (inner) satellite
e'	Eccentricity of outer satellite
f_k	Disturbing function coefficients
I	Moment of Inertia
i	Imaginary number
j	# of orbits outer moon
J_1	Angular momentum inner moon
J_2	Angular momentum outer moon
J_2	Planetary oblateness
J_U	Unrelaxed compliance
k_2	Potential Love number
M	Mass of primary
m	Mass of (inner) satellite
m'	Mass of outer satellite
m_mode	Mode azimuthal number
n	Mean motion of (inner) satellite
n'	Mean motion of outer satellite
p	Poincaré element of inner satellite
p'	Poincaré element of outer satellite
Q	Tidal quality factor

q	Complex conjugate of p
q	MMR order
R_p	Radius of primary
R_s	Radius of satellite
t_α	Modal migration timescale
t_p	Timescale of change in planetary rotation rate
t_{tide}	Semi-major axis migration timescale
ν	Difference between mean motions
V_1	Commensurable argument
$\text{Im}(k_{2,p})$	Planetary imaginary Love number
$\text{Im}(k_{2,s})$	Satellite imaginary Love number

1

Introduction

The moons of our Solar System show a great variety in characteristics and surface features. From volcanic activity on Io (e.g. Peale et al., 1979; Ojakangas and Stevenson, 1986), the subsurface oceans on Europa (e.g. Tittemore, 1990a; Pappalardo et al., 1999; Hussmann and Spohn, 2004) and Enceladus (e.g. Schubert et al., 2010); to the barren worlds Iapetus (e.g. Schubert et al., 2010; Polycarpe et al., 2018) and Callisto (e.g. Peale, 1999). This diversity is caused by differences in formation processes and past thermal activity, spanning from accretion heating during formation (Hillier and Squyres, 1991), radiogenic heating due to radioactive decay (Hussmann et al., 2010), to periods of strong tidal heating as the result of an eccentric or inclined orbit (e.g. Yoder and Peale, 1981; Segatz et al., 1988). This last process shows that the orbital history affects a moon's thermal history, and can therefore be used to explain some of its attributes.

Tidal heating within a moon is stronger the higher the eccentricity or inclination, but also depends on its interior properties. The gravitational pull of a satellite on its primary, and vice versa, causes a deformation in both: a tidal bulge. Due to the gradient of the gravitational field of the other body, the acceleration varies per location, leading to this distortion (Peale, 1999). The characteristics of the deformation depend on the internal properties of the primary and secondary and the forcing frequency. These factors are characterised by the two Love numbers (Love, 1909), k_2 and h_2, which control the period and amplitude of the response; and the tidal dissipation factor (Q), which is a quality factor that governs the phase of the response and is often used to summarise uncertainties regarding the dissipation mechanism (Goldreich and Soter, 1966). It is proportional to the angle between the position of the satellite behind or ahead of the axis of the tidal bulge of the planet. A lower Q corresponds to a larger lag, and thus more friction and dissipation within the body. For satellites, these two properties are generally found from rheology models (Renaud and Henning, 2018), while the planet's Q has typically been assumed to be constant throughout the system (e.g. Goldreich, 1965; Goldreich and Soter, 1966).

In an isolated primary-satellite system, tidal dissipation drives the orbit to an evolved state. The first aspect of this is despinning, which is, for circular orbits, a 1:1 spin-orbit resonance. In a perfectly circular and equatorial orbit, the heating and eccentricity damping processes stop once this synchronous motion is reached (Hussmann et al., 2010). The second aspect of the evolution is circularisation, which occurs over a longer timescale than despinning (Peale, 1999). Due to this, a satellite can be in a (semi-)synchronous orbit, while retaining an increased eccentricity. The tides raised on the satellite by the planet drive circularisation, while the tides raised on the planet by the satellite can maintain an increased eccentricity. The former is usually the largest effect in the giant planet systems, hence their satellites tend to have a near zero free eccentricity. Finally, the satellite's orbit expands when the planet's tidal bulge is ahead, or contracts when it lagging behind the satellite, a process known as tidal migration (Goldreich and Soter, 1966).

The circularisation process can be hindered by the interaction with other satellites in a system. A mechanism that affects this significantly is orbital resonance, which was first examined by Goldreich (1965) in the context of tidal migration. Two main types of resonance can be identified: *mean motion resonance* (MMR) —commensurability of orbital revolution frequency— and *secular resonance* —commensurability of orbital precession frequency. Satellites can get caught in resonance while their orbits evolve due to tidal interactions. The type of resonance most relevant to the conducted study is MMR. MMRs between bodies occur when the ratio of their orbital frequencies is close to $\frac{p+q}{p}$, where $\{p \wedge q\} \in \mathbb{Z}$; and $p \neq 0$, $q \geq 0$ (Malhotra, 2012). Here, $q > 0$ is the order of the resonance —i.e. the number of conjunctions before one occurs again at the same

longitude— and the strength of the potential is proportional to e^q and i^q for small eccentricities (e) and inclinations (i). Furthermore, while higher-order resonances do lead to higher equilibrium heating rates, the associated probability of capture is lower (Borderies and Goldreich, 1984; Dermott et al., 1988). The result of an MMR can be an increase in eccentricity for one or both bodies (e-type), or an increase in inclination (i-type, even-order resonances). The increased eccentricity results in more heating over longer periods of time, since circularisation is prevented.

The interactions of the previously described effects have been studied widely, and have served as explanations for some of the features mentioned above. However, uncertainties and mysteries remain. For example, Titania and Ariel's surface show signs of resurfacing, but so far no mechanism that provides sufficient heating has been identified (Tittemore, 1990b; Peterson et al., 2015), and Titan has an unexpectedly high free eccentricity (Schubert et al., 2010).

A possible explanation is given resulting from astrometric data and radio tracking in the Saturnian system, which demonstrate that there are large differences between the effective Q of a planet for different moons (Lainey et al., 2017, 2020). The cause for this variability is explained by Fuller et al. (2016), who argue that waves excited internally in a planet cause locations of resonance at certain frequencies, based on mechanisms previously described by Ioannou and Lindzen (1993a,b); Ogilvie and Lin (2004). A satellite can get caught in a so-called resonance lock with a low Q_p, evolving along with the location of resonance at a faster rate than before as the planet's internal properties change. Some consequences described are: (1) convergence of moons resulting in MMR may be avoided when both are caught in a resonance lock, since both would be migrating at similar rates; or (2) an outer moon in MMR can be caught in a resonance lock during its outward migration, escaping the MMR. However, no studies have explicitly included the resonance locking mechanism in their models of thermal-orbital evolution of moons. So far, it has only been included in the form of a point of discussion or a low assumed constant Q_p (e.g. Polycarpe et al., 2018; Celletti et al., 2019), or examined analytically to predict the stability of a pre-existing MMR (Luan and Goldreich, 2016). The mechanism could have great implications for the proposed evolution of a variety of bodies. As such, a more detailed study is required to uncover the possible effects of tidal migration, e-type MMRs, and resonance locking combined.

In order to better characterise the interactions between these effects, a numerical model is developed in this thesis that links the effects of tidal interactions, e-type MMRs of first- and second-order, and the resonance locking mechanism. Therefore, the general objective of this thesis is:

> To develop a model extendable to real systems in the Solar System that describe the influence of frequency-dependent tidal response of the primary on the capture, evolution, and escape mechanisms of e-type MMRs of the first- to second-order; by coupling the variation of the values of Q_p with tidal frequency with the classical thermal-orbital evolution approach in a numerical model.

The corresponding research question that was identified at the start of this study is follows:

> How does the frequency-dependent Q_p affect the history and future of moons in MMRs?

The sub-questions to be considered in order to answer the general research question are

1. What are the possible outcomes of the capture, evolution, and escape under the influence of tidal migration, e-type MMRs of first- to second-order, and resonance locking combined?

   Exploring the general behaviour of the resonance lock and the moons results in a better grasp on how the interactions affect the evolution of moons. Specifically since this numerical coupling has not been done, it will be interesting to see what exactly happens.

2. How do the capture, evolution, and escape mechanisms in the extended model differ from classical, constant Q_p results found in literature?

   The results from question 1 can be compared to classical results, to see what aspects of evolution are changed.

3. What are the implications of these differences on some of the explanations for currently observed features of real systems in the Solar System?

   By extrapolating the behaviour found to bodies in the Solar System, it can be seen whether some inexplicable features could potentially be caused by the resonance locking mechanism.

The report adheres to the following structure. First, the model development and results are summarised in paper form in Chapter 2. The answers to the research questions and further recommendations can be found in Chapter 3. Finally, Appendices A and B contain more detailed information regarding model development and choices made.[1]

[1] The entire model can be found in the *resonance_locking* branch of `https://github.com/mroviranavarro/evolve`.

Astronomy & Astrophysics manuscript no. output
August 13, 2021

Mean Motion Resonances in a Resonance Lock

Stability and Evolution

D. Gasman[1]

Delft University of Technology, Kluyverweg 1, 2629HS Delft, the Netherlands
e-mail: D.Gasman@student.tudelft.nl

ABSTRACT

Context. Interactions between tidal migration and the encounter of mean motion resonances (MMRs) have widely been used in attempts to explain unexpectedly young surfaces and high free eccentricities of moons. A driving variable in this process is the planetary quality factor (Q_p), which has so far been assumed to be constant throughout the system. However, data showing faster migration rates for moons farther from the primary indicate otherwise. The proposed mechanism behind this phenomenon is resonance locking, which uses steep localised dips in Q_p to explain why certain moons migrate faster than expected. These dips evolve along with the primary, and a secondary may reach the same migration rate, "locking" with a frequency mode.
Aims. We aim to provide a better understanding of the orbital evolution of pairs of moons in MMRs under the influence of the resonance locking mechanism, from the process of capture into a resonance lock, to the possibility of breaking the MMR. In this context, we examine differences between first- and second-order MMRs.
Methods. A higher order numerical model has been developed that combines the effects of tidal migration and MMRs with the newly proposed resonance locking mechanism. It is used to examine a variety of scenarios and test the behaviour of a pair of moons when the inner moon is in a resonance lock. Additionally, the stability of the 2:1 and 3:1 *e*-type resonances when encountering a mode are examined.
Results. It was found that the $|\mathrm{Im}(k_{2,p})|$ required to enter the resonance lock can reach values 50% higher than expected from theory, due to oscillations in mean motion caused by the interactions with the second moon. A substantial growth in eccentricity can be experienced, potentially growing indefinitely provided both the resonance lock and MMR are maintained. Finally, while it is unlikely that a resonance lock has caused an MMR to break in the past of our Solar System due to the lower masses, it may occur for heavier exoplanets.
Conclusions. We can conclude that resonance locking mechanism provides an alternative explanation for high free eccentricities and unexpected surface features. However, to better predict whether moons have been or are affected by a mode, for the Galilean moons data from the upcoming JUICE and Europa Clipper missions are needed. Finally, Juno has already helped constrain some of Jupiter's internal properties, and will continue to do so during the remainder of its mission, which may aid characterisation of the mode characteristics.

Key words. tidal dissipation – mean motion resonance – resonance locking

1. Introduction

The heating within a moon and its orbital evolution are intricately connected. While heat is produced in its early history by accretion during formation or by radioactive decay in the millions to billions of years after (Hussmann et al. 2010), the heat production due to the tidal interactions between a satellite and its primary can show significant changes throughout the body's lifetime depending on the evolution of its orbit (e.g. Yoder & Peale 1981; Segatz et al. 1988). A sufficient increase in a moon's internal heat production can result in resurfacing —which makes its surface much younger than expected— but also internal melting, which in turn affects the migration process (Peale et al. 1979).

As first examined in combination with tidal effects in Goldreich (1965), the encounter of mean motion resonances (MMRs) during satellite migration can have great consequences for the internal heating throughout its history. MMRs between bodies occur when the ratio of their orbital frequencies is close to an integer. These commensurabilities can drive the eccentricity (*e*-type, forced eccentricity) or inclination (*i*-type) to non-zero values. By increasing either of these two properties, tidal dissipation becomes more prominent and increases the heating within the moon. The higher the order of the resonance —i.e. the number of conjunctions before an encounter at the same longitude— the lower its stability, but the higher the eccentricities and inclinations that may be reached (Dermott et al. 1988).

The tides raised on the moon not only result in internal heating, but also drive the circularisation (reducing the free eccentricity) of the orbit and reduce its inclination (Peale 1999). The planetary tides cause the moon's migration outward (Goldreich & Soter 1966). Therefore, tidal interactions can act opposite to MMRs, and determine the sequential order of MMRs encountered. The properties of tidal deformation are determined by the Love numbers, originally introduced in Love (1909). The outward migration is governed by the Love number k_2 and the tidal dissipation factor (Q) of the planet; and the lower Q_p, the faster the outward migration of its moons. Additionally, for a constant Q_p, outward migration slows down for moons farther away from the primary. The assumed value of Q is related to k_2 such that they are analogous to a single variable: the imaginary Love number ($\mathrm{Im}(k_2)$) (Segatz et al. 1988), which for the moon is often determined using a rheology model (see Renaud & Henning (2018)

for an overview). This relation is:

$$\mathrm{Im}(k_2) = \frac{\mathrm{Re}(k_2)}{Q}, \quad (1)$$

and $\mathrm{Im}(k_2)$ has the opposite effect of Q alone: the higher, the stronger the dissipation. The exact value of $\mathrm{Im}(k_{2,s})$ depends on the satellite's interior, which changes over time as it experiences periods of melting (e.g. Peale et al. 1979; Segatz et al. 1988).

The two mechanisms have since been used in attempts to explain some of the most remarkable features on the moons in our Solar System; from volcanic activity on Io (e.g. Peale et al. 1979; Ojakangas & Stevenson 1986; Hussmann & Spohn 2004), to Enceladus' subsurface ocean (e.g. Meyer & Wisdom 2008; Zhang & Nimmo 2009). However, both Ariel and Titania show signs of resurfacing, but so far no mechanism that provides sufficient heating has been identified (e.g. Tittemore 1990b; Peterson et al. 2015); the origins of Tethys' surface features like Ithaca Chasma (e.g. Giese et al. 2007; Chen & Nimmo 2008; Hussmann et al. 2019) remain a mystery; and the mechanism behind Enceladus' subsurface ocean being maintained is yet to be confirmed (Souček et al. 2016; Nimmo et al. 2018). Therefore, undiscovered, yet essential mechanisms must play a role in forming these features.

Due to the connection between tidal interactions and MMRs, and their influence on the thermal history of moons, it is essential to know how fast the migration has been over the course of history —i.e. the value of Q_p. This factor is difficult to constrain and often disputed (see e.g. Tittemore (1990a); Malhotra (1991) for the Jovian system, or e.g. Charnoz et al. (2011) for Saturn), and has typically been assumed to be a constant. However, recent observations of the migration rates of the Saturnian moons (Lainey et al. 2017, 2020) suggest otherwise. Their results show that some of the moons of Saturn migrate at unexpectedly fast rates (e.g. Titan), corresponding to variations in Q_p.

To explain these observations, Fuller et al. (2016) propose a frequency dependency for the planetary Q due to excitation of inertial waves or g-modes within a gaseous planet due to periodic tidal forcing, causing dynamical tides. The result of these dynamical tides is a spectrum of narrow, but steep dips in Q_p at different frequencies (ω), illustrated in Fig. 1, as opposed to the constant Q_p from equilibrium tides. As the planet's interior evolves, the frequencies of these dips change as well. The rate at which this occurs is faster than the tidal migration caused by equilibrium tides, and will be similar to the planet's evolution timescale (Fuller et al. give 4.5-100 Gyr for Saturn). As a mode encounters the moon's frequency, this moon's Q_p decreases until its migration rate matches that of the mode, shown in the close-up of Fig. 1. They evolve together, and this "resonance lock" is maintained as the moon moves outward, until the Q_p required to match the evolution rate of the mode is lower than the minimum value of the dip. This results in much faster migration, and changes in MMRs encountered —or passed. Lainey et al. (2020, Supplementary information) argue that the pattern of inertial waves resulting in a constant migration timescale for all satellites in the system fits their observations better than g-modes, which result in increasing timescales with increasing semi-major axis. Inertial waves are also more likely to occur in the gas giants than g-modes (Ogilvie & Lin 2004), and are considered here. Therefore, the essential difference with the equilibrium tides is, aside from lower migration rates, that the migration timescale of the moons in a resonance lock is now constant, rather than Q_p.

Some additional consequences of the resonance lock given by Fuller et al. (2016) are: (1) an inner moon catching up with an outer moon resulting in MMR may be avoided when both

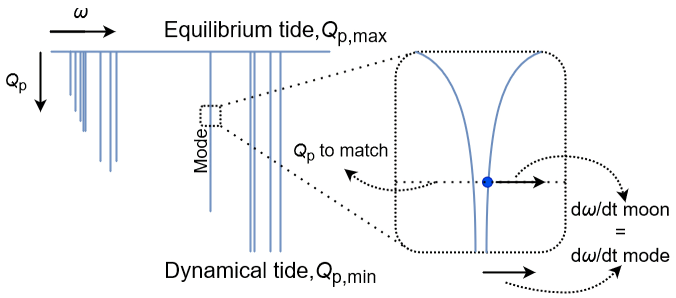

Fig. 1. Illustration of the dips in Q_p for different frequencies (ω), based on Fig. 1 of Fuller et al. (2016). The higher value of Q_p resulting from equilibrium tides corresponds to relatively slow migration of the moon. As the frequency of the moon encounters a dip, its Q_p decreases such that the rate at which its frequency changes matches that of the mode. This causes the moon to migrate outward faster than before. The fraction between the rate at which the dip's frequency evolves and the frequency itself (timescale) remains constant, meaning that when a moon is farther from the planet, a lower Q_p is required to match the mode's rate. Once this value is lower than the minimum of the dip, the resonance lock is broken.

are caught in a resonance lock, since they would be migrating at similar rates; or (2) an outer moon in MMR can be caught in a resonance lock during its outward migration, escaping the MMR. The mechanism has so far only been included in the form of a much lower constant Q_p (Polycarpe et al. 2018), or analytically in a discussion (Luan & Goldreich 2016), but no studies have explicitly included the resonance locking mechanism in their models of thermal-orbital evolution of moons. It could have great implications for the proposed evolution of a variety of bodies. Aside from a change in migration rate, the exact behaviour near and in a resonance lock is unknown, as are the consequences for the stability and outcome of MMRs. As such, a more detailed study is required to uncover the possible effects of tidal migration, e-type MMRs, and resonance locking combined.

In this paper, a description is given of a fourth-order numerical model that combines the three mechanisms introduced above, and is applicable to 2:1 and 3:1 e-type resonances. We aim to characterise the evolution before, during, and after encounter with a resonance lock, and find differences between the different order MMRs. To do so, the paper is structured as follows. First, the model set-up is given in Sec. 2. The results of the experiments are presented and elaborated upon in Sec. 3. Finally, a discussion of the results and the corresponding conclusions are given in Sec. 4 and Sec. 5, respectively.

2. Methodology

In order to examine the behaviour in a variety of scenarios in an MMR and a resonance lock, a numerical model is developed. This orbital evolution model uses the interior model of Rovira-Navarro et al. (2021), which built on the method of Jara-Orué & Vermeersen (2011) to include heat-piping (Moore 2001; Bierson & Nimmo 2016) and Andrade rheology (Efroimsky 2012), using the propagator matrix technique from Sabadini et al. (2016). Although it includes detailed calculations related to the satellite's interior properties, the orbital evolution equations are accurate up to $O(e^2)$ when assuming $\mathrm{Im}(k_{2,s}) \gg \mathrm{Im}(k_{2,p})$. Furthermore, only the 2:1 resonance is supported, and the fraction between semi-major axes (α) does not change. An advantage of this approach is the fast integration time, as smaller periodic changes that average out over extended periods of time are cancelled out, but it is not accurate enough when considering the fast changes

in mean motion and eccentricity caused by the sudden decrease in Q_p. When in an MMR, this can potentially drive the eccentricity to much higher values, thus requiring additional terms in e. Since the purpose of this paper is to examine the behaviour under the influence of a resonance lock for different order MMRs, higher order terms must be included in the tidal response of the orbit (Sec. 2.1) and the disturbing function (Sec. 2.3), in addition to adding the resonance locking mechanism (Sec. 2.2).

2.1. Tidal Effects

Following Rovira-Navarro et al. (2021), the equations used for tidal migration in the model are based on the derivations in Boué & Efroimsky (2019), which have removed certain errors that commonly occurred in previous works (see also e.g. Ferraz-Mello et al. (2008); Efroimsky & Makarov (2013); Makarov & Efroimsky (2013) for detailed discussions regarding frequently made errors). These equations are infinite sums in eccentricity and inclination. However, only terms in eccentricity up to fourth-order are considered, as all cases examined here are on orbits that are not inclined. The relations used by Rovira-Navarro et al. (2021) are accurate up to second-order in eccentricity for the moon's tidal response, but neglect the tidal contribution of the planet in $O(e)$ or higher. This results in Eqs. 23a-24b:

$$\frac{1}{\tau_n} = \frac{1}{n}\frac{\mathrm{d}n}{\mathrm{d}t} - \frac{57}{7}\frac{e^2}{\tau_e} = -\frac{9}{2}\frac{m}{M}\left(\frac{R_p}{a}\right)^5 |\mathrm{Im}(k_{2,p})| n \,, \tag{2}$$

$$\frac{1}{\tau_e} = -\frac{1}{e}\frac{\mathrm{d}e}{\mathrm{d}t} = \frac{21}{2}\frac{M}{m}\left(\frac{R_s}{a}\right)^5 |\mathrm{Im}(k_{2,s})| n \,. \tag{3}$$

Here, τ_n and τ_e are the evolution timescales of the mean motion (n) and eccentricity (e); M and m the masses of the primary and secondary, respectively; R is the body's radius; and $|\mathrm{Im}(k_2)|$ is the body's imaginary Love number. Note that the subscripts p and s are used to denote the primary and secondary.

The extended versions of these equations used in the model are as derived in Boué & Efroimsky (2019), which are accurate up to and including $O(e^4)$. First, it is assumed that the system is sufficiently evolved such that the moons are tidally locked, therefore the rotational rate of the moon can be set as equal to its mean motion. This results in slightly simplified versions of Eqs. 143 and 155 of Boué & Efroimsky. The full equations of motion can be found in App. A, and are presented up to second-order below, as a direct comparison to Eqs. 2 and 3. The terms up to $O(e^2)$ of the primary's tidal response ($K_2(\omega)$) are included here, as opposed to the equations presented above, where they are not present.

$$\begin{aligned}\left(\frac{\mathrm{d}a}{\mathrm{d}t}\right)_{l=2} = \\ -3an\left(1-5e^2\right)\left[\frac{m}{M}\left(\frac{R_p}{a}\right)^5 (K_2(2n-2\dot{\theta}_p))\right] \\ -\frac{9}{4}ane^2\left[\frac{m}{M}\left(\frac{R_p}{a}\right)^5 (K_2(n)) + \frac{M}{m}\left(\frac{R_s}{a}\right)^5 (K_2'(n))\right], \\ -\frac{3}{8}ane^2\left[\frac{m}{M}\left(\frac{R_p}{a}\right)^5 (K_2(n-2\dot{\theta}_p)) - \frac{M}{m}\left(\frac{R_s}{a}\right)^5 (K_2'(n))\right] \\ -\frac{441}{8}ane^2\left[\frac{m}{M}\left(\frac{R_p}{a}\right)^5 (K_2(3n-2\dot{\theta}_p)) + \frac{M}{m}\left(\frac{R_s}{a}\right)^5 (K_2'(n))\right] \\ +O(e^3) + O(i^2)\end{aligned} \tag{4}$$

$$\begin{aligned}\left(\frac{\mathrm{d}e}{\mathrm{d}t}\right)_{l=2} = \\ -ne\frac{m}{M}\left(\frac{R_p}{a}\right)^5\left[-\frac{3}{16}(K_2(n-2\dot{\theta}_p)) - \frac{3}{4}(K_2(2n-2\dot{\theta}_p))\right. \\ \left. +\frac{147}{16}(K_2(3n-2\dot{\theta}_p)) + \frac{9}{8}(K_2(n))\right], \\ -ne\frac{M}{m}\left(\frac{R_s}{a}\right)^5\left[\frac{3}{16}(K_2'(n)) + \frac{147}{16}(K_2'(n)) + \frac{867}{8}e^2(K_2'(2n))\right. \\ \left. +\frac{9}{8}(K_2'(n))\right] + O(e^3) + O(i^2)\end{aligned} \tag{5}$$

where $\dot{\theta}_p$ is the rotational rate of the planet, and the moon's Love numbers (denoted by $K_2'(\omega)$) will only have to be found for $K_2'(n)$ and $K_2'(2n)$. These quantities are proportional to the imaginary Love number ($\mathrm{Im}(k_2)$), which depends on the interior properties of the body and the specific forcing frequency (ω). For the moon, $|\mathrm{Im}(k_{2,s}(\omega))|$ results from the assumed rheology (in this study Maxwell, assuming an Io-like body with two layers), and the planetary $|\mathrm{Im}(k_{2,p}(\omega))|$ is typically assumed to be constant, but will here be frequency-dependent as described in Sec. 2.2. The variables K_2 then relate to the frequency as given in Eq. C3 of Rovira-Navarro et al. (2021):

$$K_2(\omega) = \mathrm{sign}(\omega)|\mathrm{Im}(k_2(\omega))|. \tag{6}$$

$K_2(\omega)$ is an odd function, as such $K_2'(-n)$=$-K_2'(n)$ and $K_2'(0)$=0 (Boué & Efroimsky 2019). Note that, while the model is capable of recalculating the interior properties of the moon along with the orbit, for simplicity and clarity in the results the $\mathrm{Im}(k_{2,s})$ is found only once at the start of integration.

In the model, the mean motion rather than the semi-major axis (a) is used. Since Eq. 143 of Boué & Efroimsky (2019) and Eq. A.1 express the evolution of the semi-major axis, it is converted to mean motion by

$$\frac{\mathrm{d}n}{\mathrm{d}t} = -\frac{3}{2}\frac{n}{a}\frac{\mathrm{d}a}{\mathrm{d}t}. \tag{7}$$

2.2. Resonance Locking

As mentioned in Sec. 2.1, $\mathrm{Im}(k_{2,p})$ is not kept constant, but allowed to vary along with the frequency, as depicted in Fig. 1. While Fuller et al. (2016) describe these as dips in Q_p, the tidal migration equations as discussed in Sec. 2.1 make use of $\mathrm{Im}(k_2)$, which has the opposite effect; the larger, the stronger the tidal terms. Therefore, rather than dips, peaks are considered here. This is simulated by adding a "wave" which allows the moon to migrate at faster rates. A graphical representation of the mechanism as implemented in the code is presented in Fig. 2.

As time passes, the frequency of the wave —in the figure denoted by ω_α— changes. As given in Eq. 3 of Fuller et al. (2016), the timescale with which the mode migrates is:

$$t_\alpha = \frac{\omega_\alpha}{\dot{\omega}_\alpha}\,, \tag{8}$$

with $t_\alpha > 0$. This means that the frequency of the mode will grow over time.

For resonance locking to occur within a reasonable time frame, the frequency at which the wave is placed should be close to the frequency at which the planetary $\mathrm{Im}(k_2)$ are evaluated. For the equations up to fourth-order, as fully included in App. A, the relevant frequencies are $2n-2\dot{\theta}_p$, n, $n-2\dot{\theta}_p$, $3n-2\dot{\theta}_p$, $4n-2\dot{\theta}_p$,

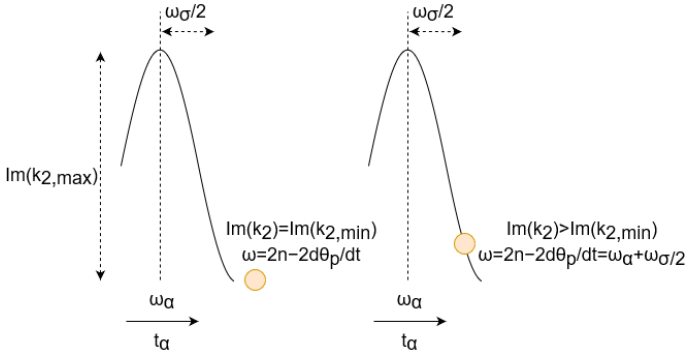

Fig. 2. Graphical representation of the resonance locking mechanism as implemented in the model. $\mathrm{Im}(k_{2,p})$ follows a bell curve, with ω_α the frequency of the maximum of the wave, ω_σ is used to give the curve a certain width (based on the standard deviation), and $\mathrm{Im}(k_{2,max})$ is the maximum value of the peak. The surrounding frequencies still result in the minimum $\mathrm{Im}(k_{2,min})$ corresponding to the equilibrium tide. Finally, ω_α changes over time, with the timescale t_α.

and $2n$. The most dominant of these terms in the migration equation is $2n-2\dot{\theta}_\mathrm{p}$, since this corresponds to the term in $O(e^0)$ in Eq. A.1. Therefore, the wave's frequency must be placed in vicinity to this frequency. Similarly to ω_α, $2n-2\dot{\theta}_\mathrm{p}$ also changes over time. In addition to the decrease in n due to tidal migration, $\dot{\theta}_\mathrm{p}$ can also vary. This generally increases, since giant planets experience a spin-up (Fuller et al. 2016; Lainey et al. 2020). While the option to adjust this value is present in the model, in this study this change has been assumed to be negligible compared to the secondary's migration rate, following Fuller et al..

The change in frequency of the wave is accounted for in Eq. 8 and the changes in mean motion result from the equations of motion (to be presented in Eq. 16). As a result, the different values for $\mathrm{Im}(k_{2,p})$ can now be calculated per frequency. In order to approximate the gradual change in $\mathrm{Im}(k_2)$ as time passes depicted in Fig. 1 of Fuller et al. (2016), the peaks are modelled using a narrow bell-curve. Following the same definition for the K_2 used in the tidal migration equations given in Eq. 6, this adjustment leads to:

$$K_2(\omega) = \mathrm{sign}(\omega) \cdot \left((\mathrm{Im}(k_{2,\max}) - \mathrm{Im}(k_{2,\min})) \cdot \exp\left(-\frac{(|\omega| - \omega_\alpha)^2}{(\omega_\sigma/2)^2} \right) + \mathrm{Im}(k_{2,\min}) \right). \tag{9}$$

Here, ω is the input frequency, $\mathrm{Im}(k_{2,\max})$ is the maximum value of the peak, $\mathrm{Im}(k_{2,\min})$ the minimum value dominant in the system, ω_α is the location of the peak at a certain point in time, and ω_σ parametrises its width.

2.3. Mean Motion Resonance

The periodic encounter of two moons at the same longitude allows for an increase in eccentricity or inclination. The focus here is on the eccentricity, and to match the $O(e^4)$ expansion of the tidal equations in Sec. 2.1, the equations here are of the same order. Following the approach in Yoder & Peale (1981), the time derivatives of the elements can be found from their Eqs. 18 and 19:

$$\frac{\mathrm{d}n_k}{\mathrm{d}t} = -\frac{3}{a_k^2}\frac{\partial \mathcal{R}_k}{\partial \lambda_k}, \tag{10}$$

$$\frac{\mathrm{d}p_k}{\mathrm{d}t} = -\frac{2i}{n_k a_k^2}\frac{\partial \mathcal{R}_k}{\partial q_k}, \tag{11}$$

where subscript k denotes the inner or outer moon, $p = e\exp(-i\tilde{\omega})$ is the Poincaré eccentric variable with q its complex conjugate, i is the imaginary number, and $\mathcal{R}$ the disturbing function. Using p over e directly has the advantage of removing singularities for small e. The disturbing function is derived for the 2:1 and 3:1 e-type resonances using Murray & Dermott (1999, App. B), and Eqs. 6.134 and 6.135 of Murray & Dermott (1999, Ch. 6):

$$\langle \mathcal{R} \rangle = \frac{\mu'}{a'}(\langle \mathcal{R}_D \rangle + \alpha \langle \mathcal{R}_E \rangle), \tag{12}$$

$$\langle \mathcal{R}' \rangle = \frac{\mu}{a}\left(\alpha \langle \mathcal{R}_D \rangle + \frac{1}{\alpha}\langle \mathcal{R}_I \rangle \right). \tag{13}$$

Here, μ is the gravitational parameter of the body. The resulting disturbing functions —presented and explained in App. B— are used in Eqs. 10 and 11 to find the equations of motion for the MMRs. These disturbing functions include the periodic variations due to the 2:1 or 3:1 MMR, and the long-periodic secular effects. Therefore, the relevant resonant angles for the 2:1 resonance are

$$\begin{aligned} \phi_{2:1,1} &= 2\lambda' - \lambda - \tilde{\omega} \\ \phi_{2:1,2} &= 2\lambda' - \lambda - \tilde{\omega}' \end{aligned}, \tag{14}$$

with $\tilde{\omega}$ the longitude of pericentre and λ is the mean longitude. For the 3:1 resonances $3\lambda'-\lambda-2\tilde{\omega}$, $3\lambda'-\lambda-2\tilde{\omega}'$, or $3\lambda'-\lambda-\tilde{\omega}'-\tilde{\omega}$ must librate, the last of which is further referenced as $\phi_{3:1}$:

$$\phi_{3:1} = 3\lambda' - \lambda - \tilde{\omega}' - \tilde{\omega}. \tag{15}$$

These equations only determine the change in elements due to the MMR itself, therefore the tidal contribution will have to be added still. For the mean motion, this is a simple addition of

$$\left(\frac{\mathrm{d}n}{\mathrm{d}t}\right)_\mathrm{tot} = \left(\frac{\mathrm{d}n}{\mathrm{d}t}\right)_\mathrm{MMR} + \left(\frac{\mathrm{d}n}{\mathrm{d}t}\right)_\mathrm{T}, \tag{16}$$

while for p this results in

$$\left(\frac{\mathrm{d}p}{\mathrm{d}t}\right)_\mathrm{tot} = \left(\frac{\mathrm{d}p}{\mathrm{d}t}\right)_\mathrm{MMR} + \left(\frac{\mathrm{d}e}{\mathrm{d}t}\right)_\mathrm{T} \exp(-i\tilde{\omega}) - ei\dot{\tilde{\omega}}_s \exp(-i\tilde{\omega}). \tag{17}$$

Here, $\dot{\tilde{\omega}}_s$ represents the primary's oblateness, a term that is ignored for the 2:1 resonance, but proves important for the 3:1 resonance. Due to its higher order different MMRs are in close proximity to each other and chaotic motion may occur, complicating the process of finding conditions for which the 3:1 resonance holds for extended periods of time. As shown by Dermott et al. (1988), when the oblateness is included, this problem is not encountered. Therefore, Eq. 15 from Yoder & Peale (1981) is used to calculate the effect of the oblateness for different conditions:

$$\dot{\tilde{\omega}}_s = \frac{3}{2} J_2 \left(\frac{R}{a}\right)^2 n. \tag{18}$$

Since the chaotic evolution did not occur for the 2:1 resonance, the term is not included for these cases. This means that the precession is ignored. This results in a slight overestimation in e

and e', but since $\dot{\tilde{\omega}}_s$ is typically 10^{-8}-10^{-9} rad/s, this effect is relatively small. Finally, the tidal contribution is not considered for the outer moons, due to its insignificance compared to the angular momentum change caused by the MMR.

The addition of terms up to fourth-order complicates further simplification as presented in Yoder & Peale (1981). By making the assumption that the free eccentricity is negligible compared to the forced eccentricity, they analytically solve the differential equations for the forced p to remove fast-changing variables, a method that becomes more complex for the more extensive equations used here. A relatively straightforward solution is to integrate all relevant angles and elements directly, but this does significantly increase the required run time. However, an advantage of this is that the behaviour during capture and escape can be examined more closely. Therefore, many of the situations analysed in this study will be for short time periods (in 10^4 yrs), and specific conditions are used to find the desired behaviour.

We define the commensurable argument (V_1) and its derivative the resonant variable (ν) as given by Yoder & Peale to integrate the elements:

$$\begin{aligned} V_1 &= -j\lambda' + \lambda \\ \frac{\mathrm{d}V_1}{\mathrm{d}t} &= \nu\,, \\ \nu &= n - jn' \end{aligned} \tag{19}$$

where $\nu = 0$ when the fraction of mean motions is exactly an integer, and $j = 2$ or 3 for the 2:1 and 3:1 MMRs, respectively.

Using Eq. 19, the final state to be integrated is

$$y = \begin{pmatrix} n \\ n' \\ p \\ p' \\ V_1 \end{pmatrix}, \qquad \frac{\mathrm{d}y}{\mathrm{d}t} = \begin{pmatrix} \frac{\mathrm{d}n}{\mathrm{d}t} \\ \frac{\mathrm{d}n'}{\mathrm{d}t} \\ \frac{\mathrm{d}p}{\mathrm{d}t} \\ \frac{\mathrm{d}p'}{\mathrm{d}t} \\ \nu \end{pmatrix}. \tag{20}$$

This is done using a Runge-Kutta 4 integration scheme with a time step of ∼7 hours, which is at the boundary of the transition from truncation to rounding errors and results in absolute errors of $\epsilon_{abs,n} \approx 3 \cdot 10^{-15}$ rad/s and $\epsilon_{abs,e} \approx 1 \cdot 10^{-9}$ after 1000 yrs. The satellite's interior can still be integrated at larger time steps as described in Rovira-Navarro et al. (2021), but as mentioned in Sec. 2.1, this is not done in this study.

Finally, it is not assumed that α is perfectly constant. This means that the corresponding Laplace coefficients (Murray & Dermott 1999, Eq. 6.67)

$$\frac{1}{2} b_s^{(j)}(\alpha) = \frac{1}{2\pi} \int_0^{2\pi} \frac{\cos j\psi \mathrm{d}\psi}{(1 - 2\alpha\cos\psi + \alpha^2)^s}, \tag{21}$$

are not constant, resulting in an additional set of variables to be found during integration time. Since only the e-type resonances are considered, $s = 1/2$. As this integral is best solved numerically, and the range of s, j, and α it is required for is large, a table with pre-calculated values is used to find the range of coefficients required in the disturbing functions. Due to relatively small variations in $b_s^{(j)}$ per α, the coefficients are only found when $\Delta\alpha > 10^{-6}$.

2.4. Initial Conditions

The aim of this thesis is not to perfectly simulate an existing system; instead, the physical properties of the bodies presented in Tab. 1 are kept constant, and only the orbital parameters of two identical moons and planetary imaginary Love numbers are varied. When discussing systems where the two moons start "in resonance," the initial conditions that will be used result in resonant behaviour sufficiently strong for the addition of the wave near the inner moon to cause both moons to migrate at a faster rate. Additionally, another condition for resonance is that the associated resonant angles, mentioned previously in Sec. 2.3, are librating for an extended period of time after the start of integration.

These sets of initial conditions for the 2:1 resonance were found by integrating a set of random initial conditions for a sufficiently long period of time: ν was assumed to be $1{\cdot}10^{-8}$ rad/s, $e = 1 \cdot 10^{-10}$ and $e' = 1 \cdot 10^{-11}$, while the other variables were allowed to change within a specific range; $[1{\cdot}10^{-5}, 3{\cdot}10^{-5}]$ rad/s for n, and $[0, 2\pi]$ for the angles V_1, ω, and ω'. To speed up the process, the scalability of Q —employed as well in e.g. Lari et al. (2020)— was used to extend the total time, while reducing run time. In this method, all values of Q are assumed to be 10^3 times lower than in reality, therefore showing the same behaviour in a thousandth of the time. Nine sets of initial conditions were found using this method, which can be found in Tab. C.1.

The 3:1 resonance proved more challenging to find, due to the lower probability of capture for higher order resonances (e.g. Borderies & Goldreich 1984; Dermott et al. 1988), and out of the 200 samples of the Monte Carlo simulation, only four sets of initial conditions were found for which resonance held for longer than 40,000 years. Here, the search space was the same as that of the 2:1 MMR mentioned above, with a few exceptions: ν was assumed to be $1{\cdot}10^{-11}$ rad/s, and e and e' were randomly selected within the ranges $[0, 1{\cdot}10^{-10}]$ and $[0, 1{\cdot}10^{-11}]$. Conditions for which one of the resonant angles (described in Sec. 2.3) shows phases of libration were investigated further. The resulting sets of initial conditions are summarised in Tab. C.2. All of these conditions correspond to a mixed ee'-resonance associated with the libration of $\phi_{3:1}$ (Eq. 15). This is likely due to the fact that ν was kept constant and the resonances are well separated, therefore the same resonance would be encountered first every time. Furthermore, the eccentricities are relatively large due to the chaotic phase preceding the capture into resonance. Since the range of initial conditions found is limited, trends with distance from the planet cannot be examined for the 3:1 MMRs, while this can be done for the 2:1 resonance. Therefore, a general comparison between the first- and second-order MMRs will be conducted.

A demonstration of the previously described behaviour for the 2:1 resonance can be found in Fig. 3, when using $t_\alpha = 100$ Myrs. The first row presents the behaviour without a resonance lock, while in the second row this effect is included. The bottom row shows the motion of the moon over the wave. This demonstrates that when the wave is included, the migration rate increases compared to the constant $\mathrm{Im}(k_{2,p})$ model. Both show oscillations due to the MMR. Note that the migration rate is relatively quick, and the peak height is chosen such that the motion over the wave is also depicted. Therefore, the approximate equilibrium value (around point 2) is high on the peak. In a more realistic scenario, the moon will likely lock with the wave for a far more extended period of time with a lower migration rate.

3. Results

The results in this section were generated using a selected set of initial conditions for which the two moons are approximately in resonance, as described in Sec. 2.4. The conditions for the inner moons are shown compared to the current orbits of Solar System moons in Fig. 4. The full set for the 2:1 resonance is given in Tab.

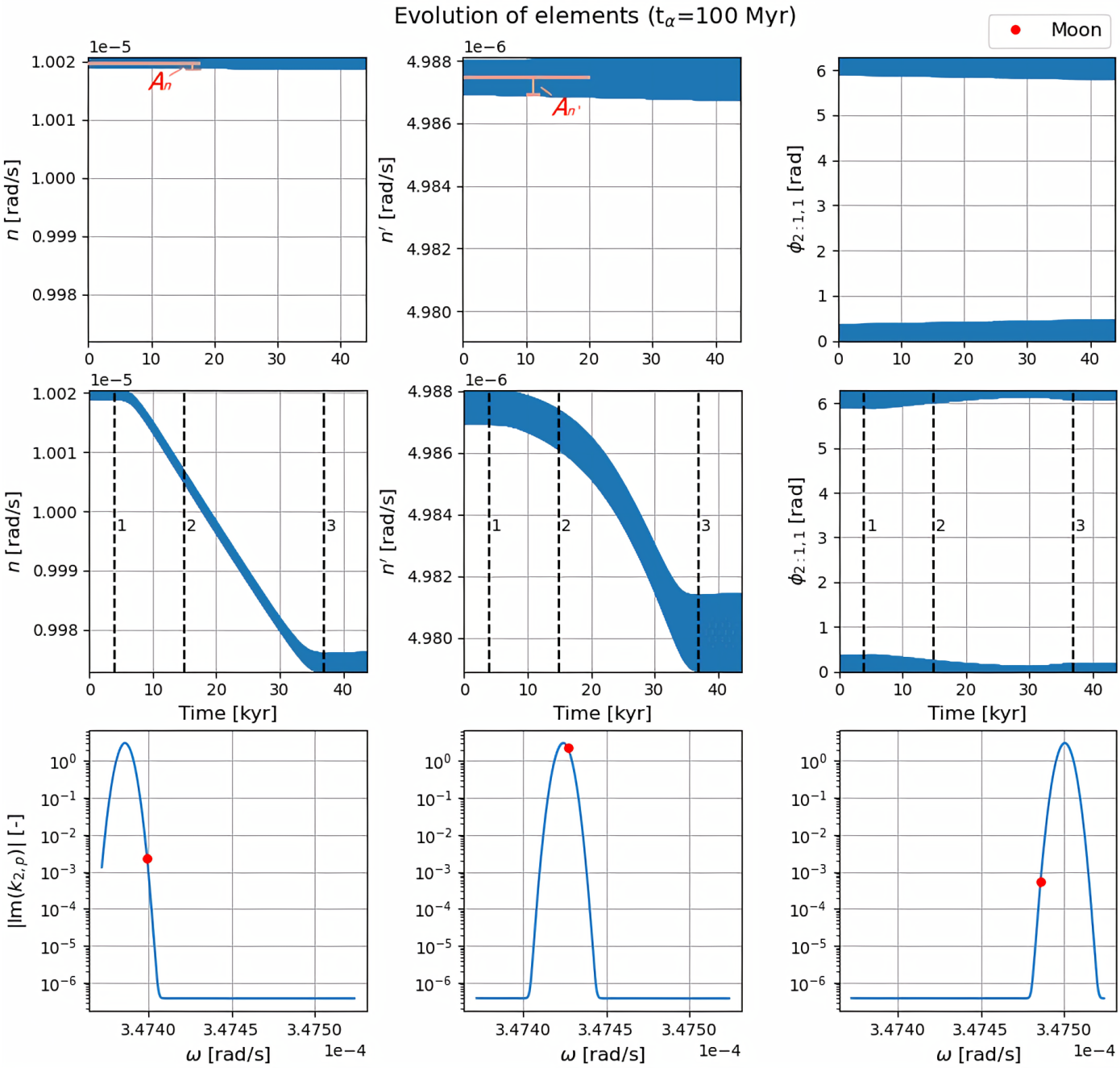

Fig. 3. Comparison of behaviour without the frequency dependent Im($k_{2,p}$) (top) and upon capture with the resonance lock (centre), for a 2:1 resonance and t_α = 100 Myrs. The top row demonstrates that equilibrium tides result in very slow migration, barely visible over this short period of time. In the second row the inner moon starts to migrate at a faster rate due to an encounter with a mode, and transfers its angular momentum to the outer moon to increase its migration rate as well. The movement of the moon over the peak is shown on the bottom row, where the first, second, and third plots correspond to time points 1, 2, and 3, respectively. Note that A_n indicates the amplitude of the mean motion of the inner moon, and $A_{n'}$ is the amplitude of the mean motion of the outer moon. The former will be discussed further in Sec. 3.1.

C.1, while the conditions for the 3:1 resonance can be found in Tab. C.2. The properties used for the planet and identical moons are summarised in Tab. 1. Note that $\omega_\sigma = 1 \cdot 10^{-8}$ rad/s, unless stated otherwise.

Fig. 3 presents three different points of interest during evolution. From this, a few interesting phases can be identified, that show the greatest deviation from the classical approach. These specifically are phases 1 and 2, since behaviour similar to the constant Im($k_{2,p}$) model is found once the wave is passed. During phase 1 the effect on the second moon is delayed, indicating that there may be conditions for which the outer moon is no longer able to follow the inner moon. As such, Sec. 3.1 and 3.2 are dedicated to the consequences of encountering the resonance lock, or phase 1. The former focuses on the required peak height to lock with the wave, while the latter uses varying t_α to find if or when a wave can break the MMR. Finally, in Sec. 3.3 we examine the evolution on the wave during phase 2 for a more extended period of time and more realistic t_α.

Table 1. Physical properties of the planet and moon.

	Planet	Moon
Mass [kg]	1.898e27	9.103916218090648e22
Rheology	-	Maxwell
Radius [km]	6.9911e4	1.821e3
Density [kg/m^3]	1.326e3	3.542e3
$\dot{\theta}$ **[rad/s]**	1.83719e-4	-
$\mathbf{J_2}$ **[-]**	1.4736e-10	-
Initial T_{mantle} [K]	-	1500

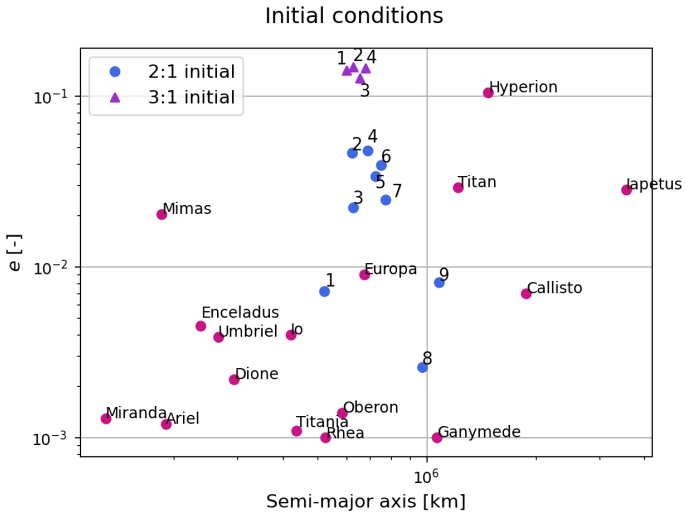

Fig. 4. Initial conditions used in this study in the context of Solar System moons. Since a Jupiter-like planet is considered, the initial conditions span the space between Io and Ganymede, with a wide range of eccentricities.

3.1. Entering the Resonance Lock

When considering a single moon affected by a resonance lock, the $\text{Im}(k_{2,p})$ required to remain on the wave —and reach the resonance locking scenario— can be found from the relation given in Eq. 13 of Fuller et al. (2016), which is based on the tidal migration equation up to $O(e)$ (see e.g. Eq. 4):

$$|\text{Im}(k_{2,p})|_{tide} = \frac{2}{9}\frac{M}{m}\left(\frac{a}{R}\right)^5\left[\frac{\omega_\alpha}{m_{\text{mode}} n^2 t_\alpha} - \frac{\dot{\theta}_\text{p}}{n^2 t_\text{p}}\right], \tag{22}$$

where m_{mode} is the azimuthal number of the mode and an integer larger than 0, here assumed to be 2, corresponding to the semi-diurnal tide on the planet. This relationship is relatively straightforward and can easily be related to the moon's position relative to the planet. However, the picture becomes more complicated when adding the second moon in resonance. Due to the resonant interaction, angular momentum is transferred from the inner to the outer moon, meaning that the $|\text{Im}(k_{2,p})|$ required to remain on the wave becomes higher. Fuller et al. also give an analytical approximation for this in Eq. 19, using the secondaries' orbital angular momentum:

$$|\text{Im}(k_{2,p})|_{MMR} = |\text{Im}(k_{2,p})|_{tide}\left[1 + \frac{J_2}{J_1}\right], \tag{23}$$

where J is the orbital angular momentum of the moon:

$$J_k = I_k n_k. \tag{24}$$

Note that the subscript MMR here indicates that *both* the tides and MMR are taken into account. Since the moons considered here are identical, their moment of inertia (I_k) is equal, and mean motion is the only factor that influences the angular momentum. Since for two moons in resonance $\frac{n}{n'} = j$ and using Eq. 24,

$$|\text{Im}(k_{2,p})|_{MMR} = |\text{Im}(k_{2,p})|_{tide}\left[1 + \frac{1}{j}\right]. \tag{25}$$

For a pair of moons in a 2:1 MMR, it is therefore expected that the $\text{Im}(k_{2,p})$ required to lock with the wave is approximately 1.5 times higher than for a single moon. Similarly, this factor becomes 1.33 for the 3:1 resonance.

Looking at Fig. 5 it can be seen that this is indeed approximately true, but only after the moon's oscillations have dampened and its position on the wave has stabilised. Therefore, when the libration width and the amplitude of the mean motion (denoted by A_n, see Fig. 3) of an MMR are still relatively wide, a phase prior to capture occurs where extreme variations in $\text{Im}(k_2)$ are experienced, pushing the moon far higher on or even past the wave. The oscillations in mean motion cause oscillations in the corresponding frequency (see Eq. 4 or A.1), resulting in variations in $\text{Im}(k_{2,p})$ as defined in Eq. 9. While the final value required to stay on the wave may be in line with the estimation from Eq. 25, the preceding phase of periodic changes results in the actual peak height required to stabilise and lock with the wave to be higher than expected. In case of a lower peak, the moons may still experience a short period of much faster migration, but this rate will never equal the rate of the wave and resonance locking does not occur. While the only two cases are shown in Fig. 5, this pattern was visible for all sets of initial conditions.

There is a slight difference in accuracy of the theory between the 2:1 (left) and 3:1 (right) MMRs. The results for the 3:1 resonance are less accurate, due to the much higher eccentricity and first-order expansion of the Eqs. 22 and 25. Since the estimation for the 2:1 MMR is so close to the true value, it is likely that the same would be true for 3:1 MMRs with lower eccentricities.

The peak height does not need to be such that the moon does not move past the highest point. In the top plot of Fig. 6 the $|\text{Im}(k_{2,p})|$ "folds" over itself, indicating that the left side of the wave is reached (see point 3 in Fig. 3). In this case, the moon still stabilises and locks with the wave. As long as the value reached on the left side of the wave is high enough to reduce the amplitude of the mean motion and keep the migration rate similar to that of the wave itself, resonance locking may still occur. However, as soon as the moon moves over the wave completely as shown in the bottom plot of Fig. 6 (which is also the case at the end of Fig. 3), it becomes impossible to remain on the wave for extended periods of time, and reach the same migration rate. This shows that values up to 50% higher than predicted may be required to initiate the resonance lock. The required value in this case remains uncertain, and more data is necessary to determine whether a prediction method exists.

What is certain, is that the absolute maximum of $|\text{Im}(k_{2,p})|$ required to lock with the wave is such that the highest point of the peak is not passed —i.e. no "folding" occurs. In this case, the amplitude of the oscillations may not exceed the frequency difference from ω_α of the wave until the frequency at which the predicted required value is reached. This is an upper bound, and will for large oscillations deviate significantly from the actual maximum required, due to the folding effect shown in Fig. 6. For cases with small amplitudes, the $|\text{Im}(k_{2,p})|$ to reach resonance locking will be relatively close to the predicted value. This is notably the case for the tested conditions for which $\omega_\sigma/2 > 2A_n$, i.e. sets 1 and 9 in Tab. C.1, where A_n represents the amplitude of the oscillations in n as presented in Fig. 3. The frequency at

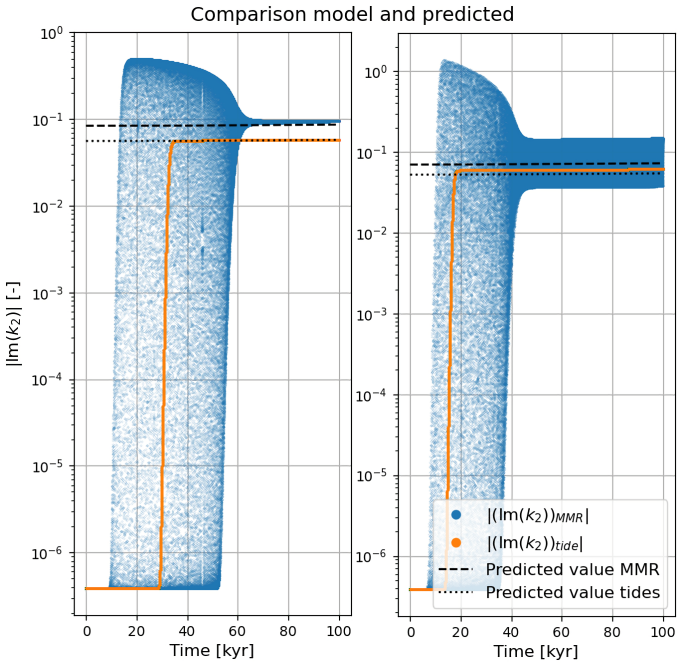

Fig. 5. Comparison between the predicted values for $|\mathrm{Im}(k_{2,p})|$ from Eqs. 22 and 25 for the 2:1 (left) and 3:1 (right) MMRs, and the results from the model. After a period of oscillating on and off the wave, the moons settle and continue to migrate along with the wave. $t_\alpha = 100$ Myr was used, resulting in relatively high $|\mathrm{Im}(k_{2,p})|$ reached, but the same fraction holds for slower waves as well.

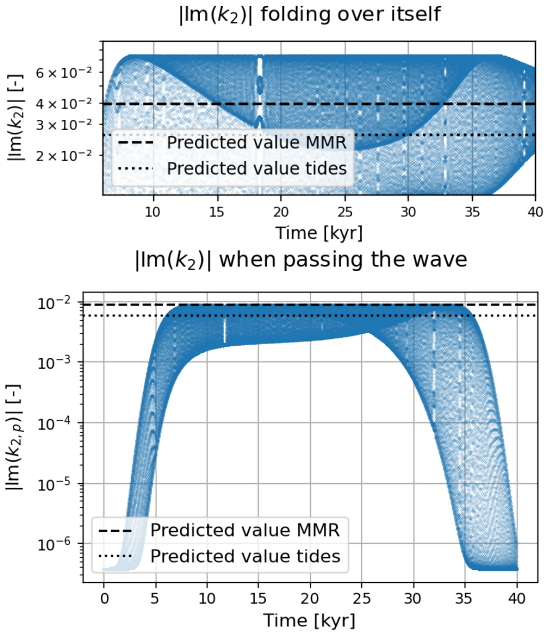

Fig. 6. The top plot shows $|\mathrm{Im}(k_{2,p})|$ "folding" over itself, therefore reaching values on the other side of the wave below the predicted values, while still locking with the wave in the end. The bottom plot shows that when the predicted required $|\mathrm{Im}(k_{2,p})|$ is assumed as a maximum, the wave is passed.

which the Love number is evaluated is $2n-2\dot{\theta}_p$, so the amplitude resulting from A_n is effectively twice as large. Therefore, it is required that

$$2A_n < \omega - \omega_\alpha \,, \tag{26}$$

where $\omega_\alpha < \omega$. The maximum of the wave, when knowing the value required at the width of the section $\omega - \omega_\alpha$, can be found starting from Eq. 9:

$$|\mathrm{Im}(k_{2,p})|_{\max,A} < (|\mathrm{Im}(k_{2,p})|_{MMR} - \mathrm{Im}(k_{2,\min})) \exp\left(\frac{(2A_n)^2}{\left(\frac{\omega_\sigma}{2}\right)^2}\right) + \mathrm{Im}(k_{2,\min}). \tag{27}$$

The true value required to initiate the resonance lock will lie between $|\mathrm{Im}(k_{2,p})|_{\mathrm{MMR}}|$ and $|\mathrm{Im}(k_{2,\max,A})|$. For small amplitudes the upper limit will be very close to the true maximum required (e.g. sets 1 and 9 of Tab. C.1). However, for $\omega_\sigma/2 < 2A_n$ the estimation breaks very quickly due to the nature of Eq. 9, and yields extremely high values. A_n fluctuates between different sets of conditions, from 10^{-8} rad/s for set 7 —for which Eq. 27 will not work— to 10^{-10} rad/s for set 9. Similarly, the true value of ω_σ is uncertain, but will be narrow, here assumed $1{\cdot}10^{-8}$ rad/s.

3.2. Passing Mode Breaking MMRs

A variety of mechanisms can break a resonance; from impact with another body (e.g. on Tethys, Zhang & Nimmo (2012)), to a slow divergence over time (e.g. as suggested for the Laplace resonance of the Galilean satellites, Lainey et al. (2009)). A premature end of an MMR is generally caused by a sudden change, and here we investigate whether the sudden "kick" of the wave can disturb the resonance in a similar fashion. This is done by reducing t_α until the MMR between the two identical moons is broken immediately upon encounter with the mode. To ensure that the inner moon locks with the wave rather than passing it (as examined in Sec. 3.1), the maximum peak height was chosen to be the extreme value of 10^5, but these values were not always reached.

First of all, it should be noted that the values for t_α required in this section greatly diverge from the range given for Saturn of 4.5-100 Gyr (Fuller et al. 2016). In fact, values as low as $7{\cdot}10^{-4}$ Myr were required to immediately pull the inner moon out of the resonance with the outer moon. Furthermore, data is used from three different widths: $\omega_\sigma = 1{\cdot}10^{-8}$, $1{\cdot}10^{-7}$, and $5{\cdot}10^{-7}$ rad/s. Although the results for these widths are relatively close together, at smaller peak widths the results can change significantly, as presented in Fig. 7. Smaller peak widths result in smaller $|\mathrm{Im}(k_{2,p})|$ required to break resonance, likely due to the increase in steepness of the wave, causing the "kick" to be more extreme.

The correlations between different factors at the moment the MMR is broken for the 2:1 resonances can be found in Fig. 8. The eccentricities show low correlation with the semi-major axis and clearly do not have a great influence, and neither does $\frac{\mathrm{d}|\mathrm{Im}(k_{2,p})|}{\mathrm{d}t}$ —the change in imaginary Love number at the point the resonance is broken. On the other hand, the resulting t_{tide}, defined as

$$t_{tide} = \frac{a}{\dot{a}}, \tag{28}$$

and $|\mathrm{Im}(k_2)|$ do show a high correlation. Therefore, it seems to be the sudden increase in migration rate of the inner moon that ends the MMR.

The $|\mathrm{Im}(k_{2,p})|$ with distance from the planet is shown in Fig. 9. The $|\mathrm{Im}(k_{2,p})|$ and the corresponding t_{tide} required to break resonance increase as the distance from the planet increases. From Eq. 2 we can see that

$$|\mathrm{Im}(k_{2,p})| \propto a^{2/15}, \tag{29}$$

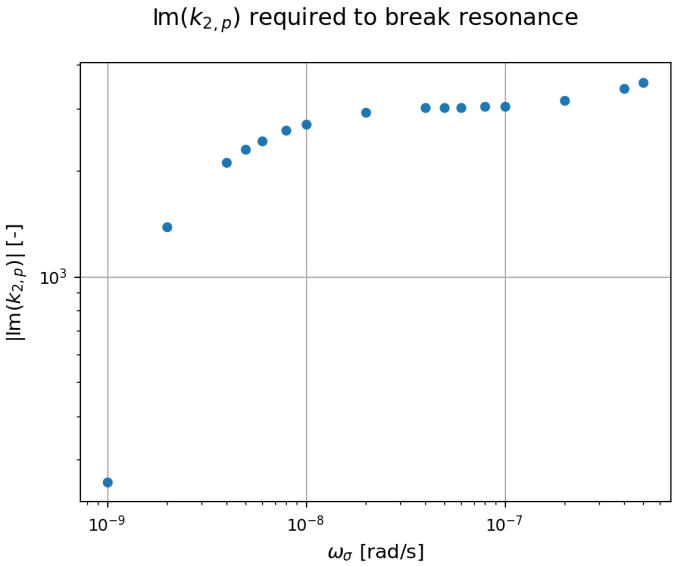

Fig. 7. $|\mathrm{Im}(k_{2,p})|$ required to break resonance as a function of peak width, for initial conditions 4 in Tab. C.1. While for wider peak widths the results do not vary much, they become highly width-dependent for $\omega_\sigma < 1 \cdot 10^{-8}$ rad/s.

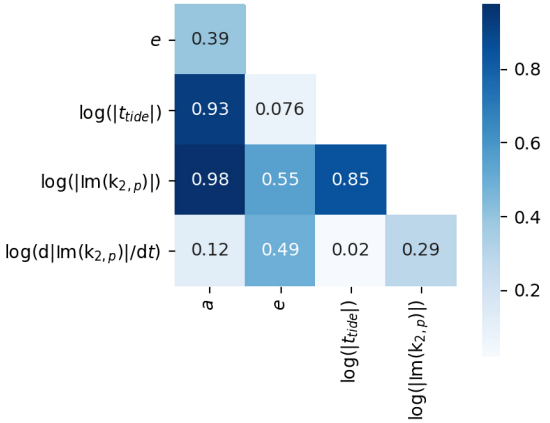

Fig. 8. Correlations between different conditions at the point that the MMR is broken, for the results of $\omega_\sigma = 1 \cdot 10^{-7}$ rad/s. While the eccentricity, despite varying significantly between initial conditions, does not influence the conditions for escape much, a strong correlation can be seen between semi-major axis and $|\mathrm{Im}(k_{2,p})|$ and t_{tide}, which are connected.

for constant t_{tide}; therefore this trend increases faster closer to the planet, and flattens farther away. The fit corresponding to this relation is shown in Fig. 9 and is able to approximate the data relatively well, but is unable to capture the seemingly steeper decline closer to the planet. This is due to the fact that t_{tide} to break resonance is not constant, but increases away from the planet similarly to $|\mathrm{Im}(k_{2,p})|$. This increase in t_{tide} required to break resonance suggests that the when the distance between the moons is larger, it becomes easier to destroy the MMR. Following the trend down to the Roche limit, approximated by

$$a_{RL} = AR_p \left(\frac{\rho_p}{\rho_s}\right)^{1/3}, \tag{30}$$

given in Charnoz et al. (2018), with $A = 2.45$ (Weidenschilling et al. 1984), and ρ_p and ρ_s the density of primary and secondary, respectively, the $|\mathrm{Im}(k_{2,p})|$ required does not quite reach realistic values. However, this is assuming a planet of Jupiter's mass, and

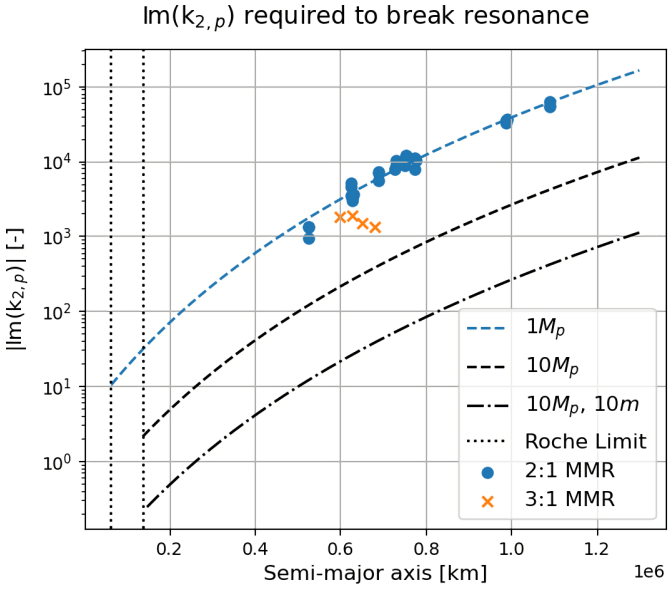

Fig. 9. $|\mathrm{Im}(k_{2,p})|$ required to break resonance, scaled for different moon and planet masses, with constant density. The inner limits for the semi-major axes are the respective Roche limits. The 3:1 resonance is broken slightly faster than the 2:1 resonance.

a moon slightly heavier than Io. Since the results for $|\mathrm{Im}(k_{2,p})|$ and t_{tide} are well-correlated with a, they can be scaled for different properties. As a simplification, we start from the equation accurate up to zeroth-order in e of $|\mathrm{Im}(k_{2,p}|$ presented in Eq. 2:

$$\frac{\tau_{n,1}}{\tau_{n,2}} = \frac{-\frac{9}{2}\frac{m_2}{M_2}\left(\frac{R_{p,2}}{a_2}\right)^5 |\mathrm{Im}(k_{2,p})|_2 n_2}{-\frac{9}{2}\frac{m_1}{M_1}\left(\frac{R_{p,1}}{a_1}\right)^5 |\mathrm{Im}(k_{2,p})|_1 n_1}. \tag{31}$$

Since the fraction is evaluated at the same positions, $a_1 = a_2$ and $\frac{n_2}{n_1} = \sqrt{\frac{M_2}{M_1}}$, the new $|\mathrm{Im}(k_{2,p})|$ required to break resonance can be found from

$$|\mathrm{Im}(k_{2,p})|_2 = \frac{\tau_{n,1}}{\tau_{n,2}}\frac{m_1}{m_2}\sqrt{\frac{M_2}{M_1}}\left(\frac{R_{p,1}}{R_{p,2}}\right)^5 |\mathrm{Im}(k_{2,p})|_1. \tag{32}$$

The results are scaled with $10M$ and/or $10m$, and represented by the black trends in Fig. 9. Note that both the Roche limit and R_p are scaled assuming constant densities, as presented in Tab. 1. The values of 10 times the mass of Jupiter and Io or more are required to reach more realistic values for $|\mathrm{Im}(k_{2,p})|$. The results of Lainey et al. (2020) indicate that values as high as 10^{-3} may be reached in the Saturnian system, while Fuller et al. (2016) predict that values of 10^{-1} could occur in the Jovian system. We can see in Fig. 9 that significantly higher masses are required to find these conditions. Since systems such as these are not present in our Solar System, it is unlikely that a resonance lock was once responsible for breaking an MMR around any of our planets. However, the mechanism may play a role for much heavier exoplanets, notably in the Brown Dwarf category (see e.g. Schneider (2018) for a discussion regarding the categorisation of bodies). The peak width may influence these results, since much more narrow peaks can reduce the $|\mathrm{Im}(k_{2,p})|$ required by a factor 10 (see Fig. 7), but this is not sufficient to reach realistic values for Jupiter or less massive planets.

Finally, the conditions for which the 3:1 resonances were broken are shown by the orange crosses in Fig. 9 as well, and require slightly lower values of $|\mathrm{Im}(k_{2,p})|$ to be broken apart. Since

higher order resonances tend to be less stable, this is as expected. While the 3:1 MMR is still difficult to destroy, when the same trend is followed as for the 2:1 MMR more realistic values will be reached quicker. Furthermore, resonances of even higher order may be broken more easily as well, perhaps reaching values realistic even for Solar System planets. However, the associated capture probability is generally much lower, and it becomes improbable that they have been responsible for high free eccentricities or resurfacing (Borderies & Goldreich 1984; Dermott et al. 1988).

3.3. Long-term Behaviour

The results presented previously are for relatively short time periods, and the assumed t_α was relatively low. In Sec. 3.1 this was done to examine the process of locking with the wave more quickly, reducing integration time; while in Sec. 3.2 these low values were required to break the MMRs. According to Fuller et al. (2016), a more realistic range for Saturn is between 4.5 and 100 Gyr, and the lower limit of this range has been assumed in this section, and integrated for 1 Myr.

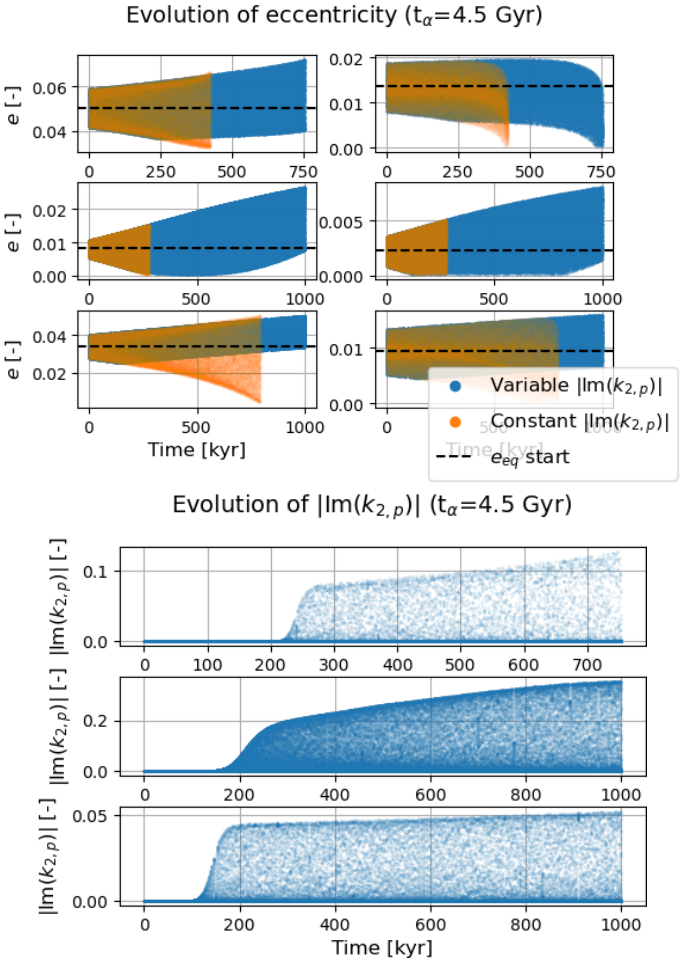

Fig. 10. Evolution of eccentricities (top set) and |Im($k_{2,p}$)| (bottom set) for conditions 1, 9, and 5 of Tab. C.1, from top to bottom. The evolution of the eccentricity of the inner moon is shown on the left, and the outer moon's eccentricity can be found on the right. As the wave encounters the moon, the eccentricity grows to much higher values than the MMR alone was able to excite. All data stops at the point the MMR is broken, which for the cases without resonance locking (orange) occurs at an earlier point in time.

Upon capture with the wave between 150-200 kyr, the migration rate of the inner and outer moon slowly increase, until the growth in frequency matches that of the mode. As already shown in Fig. 3, a delay occurs for the outer moon, which follows the faster migration at a later point in time. This persists until the peak height is not sufficient, which occurs due to the increasingly high |Im($k_{2,p}$)| required to match the constant higher rate of the wave. This value depends on a and n as presented in Eq. 22. In the time period preceding this point, the semi-major axis will continue to increase at a faster rate, and the eccentricity increases for as long as the resonance lock and the MMR persevere during the one million years examined, as presented in Fig. 10. When a single moon not in an MMR is considered, the eccentricity will instead be dampened slightly faster, due to the increase in the corresponding $|K_2(2n - 2\dot{\theta}_p)|$ term in Eq. A.2.

A comparison is shown to the constant |Im($k_{2,p}$)| model, which is plotted until the point the resonance is broken. Similarly, the MMR shown in the top row breaks prior to the end of the million years for the variable |Im($k_{2,p}$)| case as well. While in Sec. 3.1 the timescale was low enough to push the pair of moons deeper in MMR and reduce the amplitude of the oscillations relatively quickly, the more realistic value of 4.5 Gyr was not sufficient to provide a strong enough effect in set 4 of Tab. C.1, depicted in the uppermost pair of plots in Fig. 10. Therefore, for this specific set of initial conditions, the amplitude will continue to increase until the libration width is too wide and the resonance is broken, occurring at approximately 750 kyr. However, it is interesting to note that rather than dampening the oscillations entirely, instead the libration width increases at a slower rate once the moon is riding the wave. This results in the additional effect of prolonging the MMR, as is visible for all cases.

In these cases, |Im($k_{2,p}$)| reached values of $1{\cdot}10^{-1}$ and $3{\cdot}10^{-1}$ for the top two rows, to $5{\cdot}10^{-2}$ for the last, as presented in Fig. 10. Due to the outward motion these maxima are still increasing, and the same pattern of oscillations on and off the wave as discussed in Sec. 3.1 can be observed. Contrary to the Figs. 5 and 6 these plots are *not* on a logarithmic scale, so the growth in maximum |Im($k_{2,p}$)| is visible.

All initial eccentricities start in the order of 10^{-2} or lower, but they can grow until double the original value within a million years. An especially considerable growth is experienced by the last two sets of conditions where the MMR persists throughout the million years, presented on the last two rows of Fig. 10. t_α = 4.5 Gyr causes a larger change in migration rate, corresponding to much higher values for |Im($k_{2,p}$)|. Since the balance between the forced and damped eccentricity (equilibrium eccentricity, e_{eq}) reached depends on (e.g. Eq. 29 of Rovira-Navarro et al. (2021)):

$$e_{eq}^2 = -\frac{\tau_e}{\tau_n}\left(1 - \frac{\tau_n}{\tau_{n'}}\right)\left(\left(3 + \frac{57}{7}\right) + 12\frac{m}{m'}\alpha^2 + \frac{\tau_e}{\tau_{e'}}\left(\frac{m}{m'}\right)^2\left(\frac{C_2}{C_1}\right)^2\left(2\left(6 - \frac{57}{7}\right)\alpha^{5/2} + 3\frac{m'}{m}\alpha^{-1/2}\right)\right)^{-1}, \tag{33}$$

where $C_1 = -1.19$ and $C_2 = 0.43$; and we assume dissipation in the outer moon is negligible and the two moons are identical, we can substitute Eqs. 2 and 3 to find:

$$e_{eq}^2 = \frac{3}{78 + 84\alpha^2}\left(\frac{m}{M}\right)^2\left(\frac{R_p}{R_s}\right)^5\frac{\mathrm{Im}(k_{2,p})}{\mathrm{Im}(k_{2,s})}. \tag{34}$$

This implies that the eccentricity can be expected to increase as long as |Im($k_{2,p}$)| keeps growing. Therefore, theoretically, the eccentricity could increase indefinitely for as long as the MMR and

resonance lock persist. However, this must be balanced with the potential increase in $|\mathrm{Im}(k_{2,s})|$ due to internal heating and subsequent melting of material. By using the theoretical value for $|\mathrm{Im}(k_{2,p})|$ found from Eq. 25, e_{eq} of the inner moon can be found for different t_α and $|\mathrm{Im}(k_{2,s})|$, as a function of distance from the planet. This is presented in the top graph of Fig. 11, where it is shown that this perpetual growth can result in parabolic or hyperbolic eccentricities. However, the likelihood of this happening in reality is debatable, since the MMR could be broken beforehand due to the resulting instability from the increase in libration width (Dermott et al. 1988) or increase in significance of higher order terms.

Finally, the presence of α in Eq. 34 allows us to scale the eccentricities found in Fig. 11 for different order MMRs. We will refer to these using the integer q, where here $q = j - 1$. Since $\alpha = \left(\frac{1}{q+1}\right)^{2/3}$ and the $|\mathrm{Im}(k_{2,p})|$ reached scales with $1 + \frac{1}{q+1}$ (see Eq. 25), the bottom plot of Fig. 34 results from

$$\frac{e_{eq}^{q}}{e_{eq}^{j=2}} = \sqrt{\frac{78 + 84\left(\frac{1}{2}\right)^{4/3}}{78 + 84\left(\frac{1}{q+1}\right)^{4/3}} \frac{1 + \frac{1}{q+1}}{\frac{3}{2}}}\,. \tag{35}$$

This figure also includes a comparison to the constant $|\mathrm{Im}(k_{2,p})|$ model, which, in agreement with Dermott et al. (1988), shows that higher order MMRs can result in a higher excited eccentricity. Interestingly, this seems opposite for the variable $|\mathrm{Im}(k_{2,p})|$ model when $q \geq 8$, and even for $q < 8$ the fraction is greatly reduced. This indicates that the lower expected $|\mathrm{Im}(k_{2,p})|$ compensates for the smaller α, and approximately the same outcome can be expected for all orders.

Due to the limitations of the model, it becomes difficult to examine the evolution for significantly longer than a million years. However, it would be interesting to see the elements evolve further, and find how the eccentricities reached relate to the theory described above.

Once the $|\mathrm{Im}(k_{2,p})|$ required increases past the maximum of the wave, the satellite will escape from the resonance lock, and continue to evolve at the lower constant $|\mathrm{Im}(k_{2,p})|$ dominant in the system. Similarly, the motion over the wave does not show any notable features, and the oscillations reach approximately the same amplitude as prior to capture. This process was already presented in phase 3 of Fig. 3. The satellite's eccentricity will dampen at approximately the rate of Eq. 3 down to the equilibrium value from its resonant interaction.

4. Discussion

In Sec. 3, several things became clear: the required $|\mathrm{Im}(k_{2,p})|$ to lock with the wave may be higher than predicted by Fuller et al. (2016); it is unlikely that an MMR in our Solar System was ever broken by a passing wave; and the combined interactions of the MMR and the resonance lock can significantly increase the eccentricity of both moons involved. While the first two points are particularly interesting when the properties of the modes are known in more detail, the latter can be used to examine several interesting bodies to see whether the resonance lock could have been responsible for their features. This is examined more closely here, where some features of existing bodies will be considered in Sec. 4.1, after which detecting possible signs of resonance locking will be discussed in Sec. 4.2.

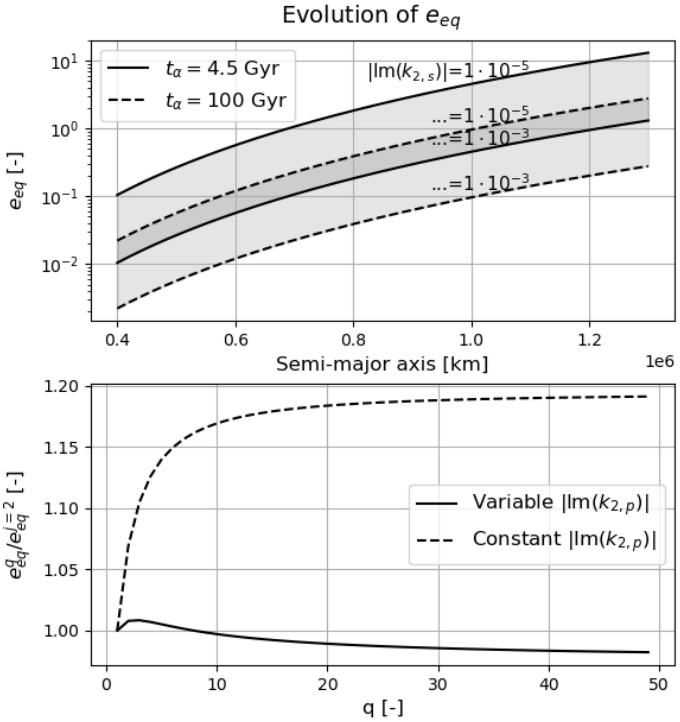

Fig. 11. Equilibrium eccentricity of the 2:1 MMR for different $|\mathrm{Im}(k_{2,s})|$ and t_α with semi-major axis (top), and scaling factor per order of MMR (q, bottom). The equilibrium eccentricity experiences a growth to extreme values. This behaviour will be largely similar for all order MMRs, although the eccentricities will be slightly higher for $q < 8$, and lower for $q \geq 8$.

4.1. Signs for Past Resonance Locks

Some moons have an inexplicably high free eccentricity, higher than the forced eccentricity excited by the MMR they may currently be a part of. This suggests that another process has pushed their eccentricities to higher values in the past. Some examples of these are present in the Jovian and Saturnian system.

The two moons of Jupiter examined here are Ganymede and Callisto. While Ganymede is currently a part of an MMR involving both Io and Europa, its forced eccentricity is only 0.0006, while its free eccentricity is 0.0015 (Yoder & Peale 1981). This remaining, higher free eccentricity has been attributed to a possible past 3:1 commensurability with Europa (Tittemore 1990a; Malhotra 1991; Showman & Malhotra 1997), but the specifics of this interaction remain uncertain. Similarly, Callisto is not involved in the Laplace resonance of the other three Galilean moons, but has a free eccentricity of 0.0073 (Yoder & Peale 1981).

Aside from the Jovian system, the moons of Saturn include some interesting cases as well. The two examples included here are Mimas and Titan. Mimas is not currently in an e-type MMR, similarly to Callisto, but has a free eccentricity of 0.0196. This has been explained using past commensurabilities similarly to Ganymede (Meyer & Wisdom 2008; Tian & Nimmo 2020), where Tian & Nimmo assumed lower Q_p values in line with resonance locking to examine the past resonances encountered. Titan, on the other hand, is in an MMR with Hyperion, but is not significantly affected by this interaction due to its size (Callegari & Yokoyama 2010). Yet, it has an eccentricity of 0.029, perhaps a remainder of a significantly higher primordial eccentricity (Schubert et al. 2010). Schubert et al. explain that this eccentricity has potentially been maintained due to Titan's inte-

rior, which may include a liquid layer, while preserving limited thermal activity for the past 4 Gyr. Another cause may be an MMR with a fast moving object due to interactions with a primordial debris disk (Ćuk et al. 2016). Note that there is evidence of Titan currently being affected by a resonance lock (Lainey et al. 2020), which would allow for a higher than expected forced eccentricity. However, further investigation is necessary to determine whether its current interaction is sufficient to drive this value to 10^{-2}, given Hyperion's much lower mass.

In order to investigate whether a resonance lock could have been responsible for some of these high free eccentricities, the current e_{free} is integrated back in time using Eqs. 2 and 3, to give an approximation for when the resonance lock would have occurred. These simple equations are accurate up to $O(e^2)$, and we assume only equilibrium tides with unchanging planet and moon interiors. In Sec. 3.3 it was shown that in a million years the dynamical tides can force the eccentricity to values 10^{-2} higher than the forced eccentricity resulting from equilibrium tides. This range was assumed to be the case upon exiting the resonance lock, but, as demonstrated in Sec. 3.3, the mechanism does have the potential to drive the eccentricity to much higher values. Note that these results were found using two moons of the same mass (slightly heavier than Io) around a Jupiter-like planet, thus the final eccentricities may not be representative of what might be reached for other bodies. For example, a much larger mass fraction between inner and outer moon can cause the lighter moon to be affected much more drastically, while the heavier moon may not experience a large change in eccentricity at all. This, in combination with the simplifications discussed above, means that the results here are indicative and not final.

When not affected by a mode the $|\mathrm{Im}(k_{2,p})|$ will be the minimum prominent for the majority of frequencies, hence for both Jupiter and Saturn a low value of $1 \cdot 10^{-5}$ is assumed. The imaginary Love numbers of the moons are assumed to be approximately $2 \cdot 10^{-3}$ for Ganymede (Malhotra 1991), 10^{-3} for Callisto (Lari et al. 2020), 10^{-10} for Mimas (Neveu & Rhoden 2019), and $5 \cdot 10^{-4}$ Titan (Ćuk et al. 2016). These values change over time as their interior properties change, e.g. as a result of tidal heating, but this is not considered in the simple toy model presented here.

Fig. 12 shows the evolution from 4.5 Gyr in the past to the present. Note that these trends are heavily dependent on the assumed $\mathrm{Im}(k_{2,s})$, and serve as a more general indication here. The bold solid lines mark the time for which $10^{-2} < e < 10^{-1}$, the assumed value when exiting the resonance lock. This shows that both Titan and Mimas are currently still in a range that could have been excited by an MMR while in a resonance lock, both recently, and much further in the past. This is potentially in line with the theory of Ćuk et al. (2016), where an object migrated at a faster rate due to the presence of a primordial disk, and pushed Titan out in the process, but not requiring the primordial disk to promote the rapid migration. Similarly, the previously mentioned MMR with Hyperion could be the culprit of the higher eccentricity being excited presently, provided Titan is indeed in a resonance lock, which would mean it is forced rather than free. Mimas, being extremely non-dissipative (Neveu & Rhoden 2019), could also have gained this eccentricity upon formation. Similarly, the damping rate of the eccentricity of Callisto is extremely low (as also found by Lari et al. (2020)), only reaching an eccentricity above 10^{-2} 3.5 Gyr ago. Its current eccentricity may therefore not have been excited from a long-term MMR, but passage through resonance while in a resonance lock, as proposed by Downey et al. (2020). For Ganymede, this range occurred between 0.24 and 0.55 Gyr in the past. Since the previous MMR encounters described above also provide a plausible explanation for its current free eccentricity, it cannot be ruled out that a resonance lock was not involved. However, the past resonances as described (Tittemore 1990a; Malhotra 1991; Showman & Malhotra 1997) may have resulted in faster pumping of the eccentricity under the influence of a resonance lock.

On the other hand, an eccentricity excited by an MMR that is now broken, can more quickly be dampened by a resonance lock. Since Ganymede has likely been involved in MMRs throughout its history, its eccentricity would not have dampened when the inner moon of the MMR pair was caught in a resonance lock. However, Callisto may have been free of MMRs for a more extended period of time, and a previously higher eccentricity could have been dampened by a resonance lock in a shorter period of time. However, Callisto's eccentricity has probably never been extremely high, as it shows no signs of resurfacing (Peale 1999).

The corresponding dissipation rates for these four moons can be found in the bottom plot of Fig. 12, and are calculated using Eq. 1 of Yoder & Peale (1981)

$$\frac{\mathrm{d}E}{\mathrm{d}t} = \frac{21}{2}|\mathrm{Im}(k_{2,s})|Mn^3a^2\left(\frac{R_s}{a}\right)^5 e^2 \,. \tag{36}$$

While Callisto, Mimas, and Titan remain at approximately the same heating rate throughout their history, Ganymede shows much larger values in the past. If Ganymede's surface features are a result of internal heating, they are likely caused by a heating rate in the order of 10^{12} W, which is in line with the results of Showman et al. (1997), and the energy required for melting some of Ganymede's material (Hussmann et al. 2010). This is also the order of $\frac{\mathrm{d}E}{\mathrm{d}t}$ reached at 0.24-0.55 Gyr in the past, after a theoretical resonance lock.

This simplified analysis indicates that resonance locking can provide alternative scenarios to the formation of surface features and high eccentricities. While no concrete conclusions can be drawn for the specific bodies considered here, we urge future work dedicated to specific bodies to include resonance locking in their hypotheses.

4.2. Detecting and Constraining Mode Characteristics

A few factors may indicate that a moon is currently affected by one of the planet's frequency modes. A migration rate diverging from the expected rate resulting from the constant Q_p model, as already explained by Fuller et al. (2016), could be an indicator. Here, we can distinguish between simply being affected by a wave, and locking with the wave. In the former case the peak is not sufficiently high, and the passing mode can cause a temporary decrease in t_{tide} which will not be as low as expected from the migration rate of the mode, as discussed in Sec. 3.1. Therefore, the smaller changes occur during a much shorter timescale, and resonance locking does not occur. Similarly, the moon may still be in the process of moving onto the wave, or exiting it. However, when the peak height is sufficiently high, resonance locking occurs which causes the moon to migrate at a faster rate with the mode over a much longer period of time. An additional indicator is an unexpectedly high eccentricity for two moons currently in an MMR, as demonstrated in Sec. 3.3.

The migration rate and therefore the $|\mathrm{Im}(k_{2,p})|$ and the $|\mathrm{Im}(k_{2,s})|$ can be inferred using several methods. First, when observing from Earth, the value of $|\mathrm{Im}(k_{2,p})|$ has typically been constrained by the value corresponding to satellite formation within the Roche limit (Eq. 30, high $|\mathrm{Im}(k_{2,p})|$), and the age of the Solar System (low $|\mathrm{Im}(k_{2,p})|$) (Goldreich 1965), while the $|\mathrm{Im}(k_{2,s})|$ of

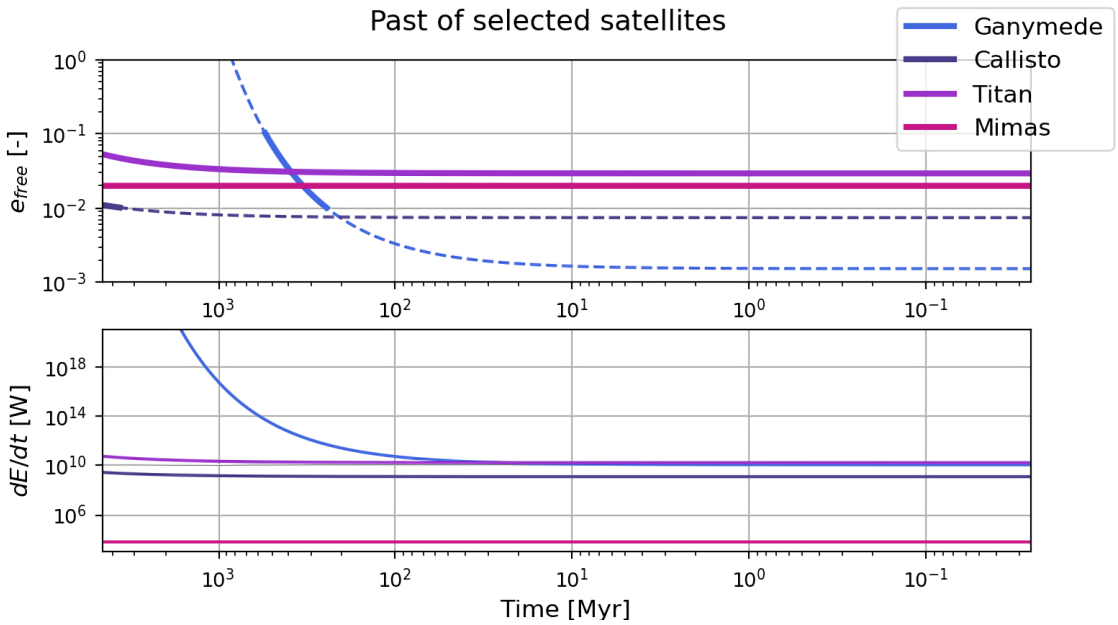

Fig. 12. Evolution of the eccentricity and energy dissipation in a selection of satellites from 4.5 Gyr in the past, to the present. The current free eccentricities were integrated backwards in time, assuming only first order tidal effects. The solid bold segments in the top plot represent the range of eccentricity values likely reached at the end of an extended period in a resonance lock.

a satellite is inferred from despinning rates (Goldreich & Soter 1966). These methods are based on formation theories, and due to the variability of both of these factors, may not be entirely accurate. For example, astrometric measurements have previously been applied by e.g. Lainey et al. (2009) to constrain Saturn's $|\mathrm{Im}(k_{2,p})|$.

A second method includes performing in-situ radio tracking of spacecraft. These data can be used to better constrain the ephemerides of the moons, providing better estimates for $|\mathrm{Im}(k_{2,p})|$ (as done in combination with astrometric data by Lainey et al. (2017, 2020)), but also to determine the gravity field for both the moons and planet. The latter has previously been done by the Galileo spacecraft at Io (e.g. Anderson et al. 2001). Cassini's radio-science provided detailed data for the Saturnian system, and has been used to better constrain the migration rates of the satellites, and in turn internal properties of Saturn itself (Lainey et al. 2017). In addition to the migration rates of the moons, the gravitational coefficients as measured by the spacecraft can be used to find planetary interior models consistent with these coefficients. These interior properties can be used to approximate the $|\mathrm{Im}(k_{2,p})|$ (Lainey et al. 2017). More precise spin rate estimations will also improve the certainty of the interior models, in turn allowing for better characterisation of the mode patterns (Ogilvie & Lin 2004; Fuller et al. 2016; Lainey et al. 2020).

Finally, in-situ altimetry gives the deformation properties, and in turn provides more information about a moon's interior, allowing for a better estimate of the current $k_{2,s}$.

While no relevant mission is currently planned to fly by Saturn, two upcoming missions to Jupiter —JUICE and Europa Clipper— are suitable candidates to provide the necessary, more precise measurements regarding the positions of its moons. Specifically the two radio experiments on JUICE and Europa Clipper can further improve the precision of the ephemerides (Cappuccio et al. 2018; Mazarico et al. 2021). These spacecraft will also provide the opportunity to better constrain the properties of the Galilean satellites: including altimetry using GALA on JUICE (Steinbrügge et al. 2019) or the radio-science by 3GM (Cappuccio et al. 2018, 2020) and PRIDE (Dirkx et al. 2017), and Europa Clipper's gravity/radio-science experiment (Verma & Margot 2018; Mazarico et al. 2021). Radio tracking of these spacecraft will yield additional data regarding Jupiter's gravity field as well.

The two future missions will mainly focus on the properties of the Galilean moons, but Juno's past and upcoming results have been dedicated to Jupiter's interior, gravity field, and tidal response (Iess et al. 2018; Durante et al. 2020). As summarised by Durante et al. (2020), after the halfway mark of Juno's mission lifetime, Jupiter's spherical harmonics up to the 12th degree were identified, with a precision from $1.7{\cdot}10^{-9}$ in J_2, to $1.9{\cdot}10^{-7}$ in J_{12} that include tidal effects. Juno was also able to better constrain the rotational rate of Jupiter, as well as determine the Love numbers up to degree and order 4, where the Love numbers k_{22} and k_{42} with uncertainties of 3 and 15% are relatively well-defined. In addition, a discrepancy was found between the observed Love number of Jupiter and the theoretical value (Durante et al. 2020), which may be an indicator for dynamical tidal activity (e.g. Idini & Stevenson 2021; Lai 2021). Therefore, the data generated by Juno in the coming years are essential for constraining models of the planet, and help predict the mode patterns in the Jovian system.

5. Conclusion

In this study, a numerical model was developed that combines the tidal effects, 2:1 and 3:1 MMRs, and the resonance locking mechanism. This model was used to examine the validity of the theories of Fuller et al. (2016), to test the stability of MMRs, and find the behaviour that can be expected when locked with a mode for a more extended period of time.

In Sec. 3.1 we found that the $|\mathrm{Im}(k_{2,p})|$ required to initiate the resonance lock may be higher than expected due to oscillations in mean motion of the moon. This causes oscillations in the tidal frequency at which the $|\mathrm{Im}(k_{2,p})|$ is evaluated, resulting in rapid motion on and off the wave. Therefore, while Eq. 25 is valid once the moon settles on the wave and the amplitude is small, Eq. 27

gives an upper bound for the value required. This results from twice the amplitude of the mean motion, which is close to the true value for small amplitudes, but is a severe overestimation for wider oscillations. In these cases, the maximum $|\mathrm{Im}(k_{2,p})|$ does not need to be such that the other side of the wave is not reached, since "folding" over the wave as shown in Fig. 6 still results in locking with the mode in the end. Since the conditions required to lock with the wave can diverge up to at least 50% from theory, this effect should be considered when examining this mechanism in the context of a moon's evolution.

Due to the faster migration of the moon while on the wave, the growth in the libration width may be halted or less rapid, causing prolongation of the lifetimes of MMRs, as shown in Sec. 3.3. Aside from this effect, the tested 2:1 and 3:1 MMRs proved very stable in Sec. 3.2. Likely unrealistically low t_α values (down to $7{\cdot}10^{-4}$ Myr) were required to immediately pull the inner moon out of resonance with the outer moon. MMRs closer to the planet are broken at lower t_{tide} than moons farther away, indicating that it becomes easier to break a resonance at larger distances. However, these still correspond to increasing $|\mathrm{Im}(k_{2,p})|$ as shown in Fig. 9. Furthermore, higher order MMRs are more easily broken. When scaling these conditions with the masses of the primary and secondary, it can be seen that realistic conditions are not reached for Solar System planets and moons. However, systems with much heavier gas giants or even Brown dwarfs may allow for this mechanism to destroy MMRs, which is of interest for future exoplanetary systems with masses exceeding $10M$ and $10m$.

When examining the behaviour of the MMR over a longer period of time for a more realistic t_α as done in Sec. 3.3, significant and rapid growth in eccentricity was observed. While the eccentricities of the tested cases could grow to at least twice the original forced eccentricity well within a million years, the mechanism has the potential to grow for the entire duration of the MMR and resonance lock, perhaps reaching escape values. As such, eccentricities between 10^{-2} and 10^{-1} can be reached in a relatively short period of time. If a single moon not affected by an MMR enters a resonance lock, the mechanism has the opposite effect and dampens the eccentricity at a slightly faster rate.

The more rapid growth in eccentricity may explain unexpectedly large free eccentricities or inexplicable surface features, such as for Ganymede, Titan, or Callisto as discussed in Sec. 4.1; but more specific research is required to confirm this for specific bodies. Furthermore, Sec. 4.2 shows that dedicated measurements of the ephemerides, gravity field, and tidal response of Jupiter and its moons by Juno and the upcoming JUICE and Europa Clipper missions can help constrain unknowns about the characteristics of mode patterns and resonance locks.

Some limitations of the current work include the short time periods examined, and the fact that the tidal dissipation within the moon remained unchanged during run time. Specifically the latter effect can change the evolution observed, and possibly lower the eccentricities reached. It is therefore advised to include these effects in future studies to examine their impact more closely. However, overall the mechanism has great implications for the past and future of moons, and the variability of Q_p should not be neglected when examining their properties in work to come.

References

Anderson, J., Jacobson, R., Lau, E., Moore, W., & Schubert, G. 2001, JGR Planets, 106, 32963
Bierson, C. & Nimmo, F. 2016, JGR Planets, 121, 2211
Borderies, N. & Goldreich, P. 1984, Celest. Mech. Dyn. Astron., 32, 127
Boué, G. & Efroimsky, M. 2019, Celest Mech Dyn Astr, 131
Callegari, Jr., N. & Yokoyama, T. 2010, Planet. Space Sci., 58, 1906
Cappuccio, P., Benedetto, M. D., Cascioli, G., & Iess, L. 2018, in Report on JUICE 3GM gravity experiment performance, Vol. 12
Cappuccio, P., Hickey, A., Durante, D., et al. 2020, P&SS, 187
Charnoz, S., Crida, A., Castillo-Rogez, J. C., et al. 2011, Icarus, 216, 535
Charnoz, S., Crida, A., & Hyodo, R. 2018, in Handbook of Exoplanets, ed. H. Deeg & J. Belmonte (Cham, Switzerland: Springer), 375–394
Chen, E. M. A. & Nimmo, F. 2008, Geophys. Res. Lett., 35
Dermott, S. F., Malhotra, R., & Murray, C. D. 1988, Icarus, 76, 295
Dirkx, D., Gurvits, L., Lainey, V., et al. 2017, P&SS, 147, 14
Downey, B., Nimmo, F., & Matsuyama, I. 2020, MNRAS, 499, 40
Durante, D., Parisi, M., Serra, D., et al. 2020, Geophys. Res. Lett., 47
Efroimsky, M. 2012, ApJ, 746
Efroimsky, M. & Makarov, V. V. 2013, ApJ, 764
Ferraz-Mello, S., Rodríguez, A., & Hussmann, H. 2008, Celest Mech Dyn Astr, 101, 171
Fuller, J., Luan, J., & Quataert, E. 2016, MNRAS, 458, 3867–3879
Giese, B., Wagner, R., Neukum, G., Helfenstein, P., & Thomas, P. C. 2007, Geophys. Res. Lett., 34
Goldreich, P. 1965, MNRAS, 130, 159–181
Goldreich, P. & Soter, S. 1966, Icarus, 5, 375
Hussmann, H., Choblet, G., Lainey, V., et al. 2010, Space Sci Rev, 153, 317–348
Hussmann, H., Rodríguez, A., Jr., N. C., & Shoji, D. 2019, Icarus, 319, 407
Hussmann, H. & Spohn, T. 2004, Icarus, 171, 391
Idini, B. & Stevenson, D. 2021, Planet. Sci. J., 2
Iess, L., Folkner, W., Durante, D., et al. 2018, Nature, 555, 220
Jara-Orué, H. & Vermeersen, B. 2011, Icarus, 215, 417
Lai, D. 2021, Planet. Sci. J., 2
Lainey, V., Arlot, J.-E., Özgür Karatekin, & Hoolst, T. V. 2009, Nature Letters, 459, 957–959
Lainey, V., Casajus, L. G., Fuller, J., et al. 2020, Nat. Astron.
Lainey, V., Jacobson, R. A., Tajeddine, R., et al. 2017, Icarus, 281, 286
Lari, G., Saillenfest, M., & Fenucci, M. 2020, A&A, 639
Love, A. E. H. 1909, Proc. R. Soc. Lond., 82, 73–88
Luan, J. & Goldreich, P. 2016, The Astronomical Journal, 153
Makarov, V. V. & Efroimsky, M. 2013, ApJ, 764
Malhotra, R. 1991, Icarus, 94, 399
Mazarico, E., Buccino, D., Castillo-Rogez, J., et al. 2021, in THE EUROPA CLIPPER GRAVITY / RADIO SCIENCE INVESTIGATION
Meyer, J. & Wisdom, J. 2008, Icarus, 193, 213
Moore, W. B. 2001, Icarus, 154, 548
Murray, C. D. & Dermott, S. F. 1999, Solar System Dynamics (Cambridge, UK: Cambridge University Press)
Neveu, M. & Rhoden, A. R. 2019, Nat. Astron., 3, 543–552
Nimmo, F., Barr, A. C., Běhounková, M., & McKinnon, W. B. 2018, in Enceladus and the Icy Moons of Saturn, ed. P. M. Schenk, R. N. Clark, C. J. A. Howett, A. J. Verbiscer, & J. H. Waite (University of Arizona Press), 79–94
Ogilvie, G. I. & Lin, D. N. C. 2004, ApJ, 610, 477
Ojakangas, G. W. & Stevenson, D. J. 1986, Icarus, 66, 341
Peale, S. J. 1999, Annu. Rev. Astron. Astrophys., 37, 533
Peale, S. J., Cassen, P., & Reynolds, R. T. 1979, Science, 203, 892–894
Peterson, G., Nimmo, F., & Schenk, P. 2015, Icarus, 250, 116
Polycarpe, W., Saillenfest, M., Lainey, V., et al. 2018, A&A, 619
Renaud, J. P. & Henning, W. G. 2018, ApJ, 857
Rovira-Navarro, M., der Wal, W. V., Steinke, T., & Dirkx, D. 2021, Planet. Sci. J., 2
Sabadini, R., Vermeersen, B., & Cambiotti, G. 2016, Global Dynamics of the Earth: Applications of Viscoelastic Relaxation Theory to Solid-Earth and Planetary Geophysics, 2nd edn. (Springer)
Schneider, J. 2018, in Handbook of Exoplanets, ed. H. Deeg & J. Belmonte (Cham, Switzerland: Springer), 611–616
Schubert, G., Hussmann, H., Lainey, V., et al. 2010, Space Sci Rev, 153, 447–484
Segatz, M., Spohn, T., Ross, M. N., & Schubert, G. 1988, Icarus, 75, 187–206
Showman, A. P. & Malhotra, R. 1997, Icarus, 127, 93
Showman, A. P., Stevenson, D. J., & Malhotra, R. 1997, Icarus, 129, 367–383
Souček, O., Hron, J., Běhounková, M., & Čadek, O. 2016, Geophys. Res. Lett., 43, 7417
Steinbrügge, G., Steinke, T., Thor, R., Stark, A., & Hussmann, H. 2019, Geosciences, 9, 320
Tian, Z. & Nimmo, F. 2020, MNRAS, 492, 369
Tittemore, W. C. 1990a, Science, 250, 263
Tittemore, W. C. 1990b, Icarus, 87, 110
Verma, A. & Margot, J.-L. 2018, Icarus, 314, 35
Weidenschilling, S., Chapman, C., Davis, D., & Greenberg, R. 1984, in IAU Colloq. 75: planetary rings, ed. R. Greenberg & A. Brahic (IAU), 367–415, IAU Colloq. 75: planetary rings
Yoder, C. F. & Peale, S. J. 1981, Icarus, 47, 1
Zhang, K. & Nimmo, F. 2009, Icarus, 204, 597
Zhang, K. & Nimmo, F. 2012, Icarus, 218, 348
Ćuk, M., Dones, L., & Nesvorný, D. 2016, ApJ, 820

Appendix A: Tidal Equations

The complete expansions of the equations of the tidal equations of motion from Boué & Efroimsky (2019) when assuming a tidally locked moon are given in this appendix:

$$\begin{aligned}\left(\frac{\mathrm{d}a}{\mathrm{d}t}\right)_{l=2} = \\ -3an\left(1-5e^2+\frac{63}{8}e^4\right)\left[\frac{m}{M}\left(\frac{R_p}{a}\right)^5(K_2(2n-2\dot{\theta}_p))\right] \\ -\frac{9}{4}ane^2\left(1+\frac{9}{4}e^2\right)\left[\frac{m}{M}\left(\frac{R_p}{a}\right)^5(K_2(n))+\frac{M}{m}\left(\frac{R_s}{a}\right)^5(K_2'(n))\right] \\ -\frac{3}{8}ane^2\left(1-\frac{1}{4}e^2\right)\left[\frac{m}{M}\left(\frac{R_p}{a}\right)^5(K_2(n-2\dot{\theta}_p))\right. \\ \left.-\frac{M}{m}\left(\frac{R_s}{a}\right)^5(K_2'(n))\right] \\ -\frac{441}{8}ane^2\left(1-\frac{123}{28}e^2\right)\left[\frac{m}{M}\left(\frac{R_p}{a}\right)^5(K_2(3n-2\dot{\theta}_p))\right. \\ \left.+\frac{M}{m}\left(\frac{R_s}{a}\right)^5(K_2'(n))\right] \\ -\frac{867}{2}ane^4\left[\frac{m}{M}\left(\frac{R_p}{a}\right)^5(K_2(4n-2\dot{\theta}_p))\right. \\ \left.+\frac{M}{m}\left(\frac{R_s}{a}\right)^5(K_2'(2n))\right] \\ -\frac{81}{8}ane^4\left[\frac{m}{M}\left(\frac{R_p}{a}\right)^5(K_2(2n))+\frac{M}{m}\left(\frac{R_s}{a}\right)^5(K_2'(2n))\right] \\ +O(i^2)+O(e^6)\end{aligned} \tag{A.1}$$

$$\begin{aligned}\left(\frac{\mathrm{d}e}{\mathrm{d}t}\right)_{l=2} = \\ -ne\frac{m}{M}\left(\frac{R_p}{a}\right)^5\left[-\frac{3}{16}\left(1-\frac{e^2}{4}\right)(K_2(n-2\dot{\theta}_p))\right. \\ -\frac{3}{4}\left(1-\frac{21}{4}e^2\right)(K_2(2n-2\dot{\theta}_p)) \\ +\frac{147}{16}\left(1-\frac{179}{28}e^2\right)(K_2(3n-2\dot{\theta}_p))+\frac{867}{8}e^2(K_2(4n-2\dot{\theta}_p)) \\ \left.+\frac{9}{8}\left(1+\frac{5}{4}e^2\right)(K_2(n))+\frac{81}{16}e^2(K_2(2n))\right]\cdot \\ -ne\frac{M}{m}\left(\frac{R_s}{a}\right)^5\left[\frac{3}{16}\left(1-\frac{e^2}{4}\right)(K_2'(n))\right. \\ +\frac{147}{16}\left(1-\frac{179}{28}e^2\right)(K_2'(n))+\frac{867}{8}e^2(K_2'(2n)) \\ \left.+\frac{9}{8}\left(1+\frac{5}{4}e^2\right)(K_2'(n))+\frac{81}{16}e^2(K_2'(2n))\right] \\ +O(e^5)+O(i^2)\end{aligned} \tag{A.2}$$

Appendix B: Disturbing Function

The averaged disturbing functions used in Eqs. 10 and 11 were derived using Murray & Dermott (1999, App. B). They include secular terms (subscript *sec*), for which $j = 0$, and resonant terms (subscript *res*) for which $j = 2$ or $j = 3$, depending on the resonance considered. The components of the disturbing function for the 2:1 MMR are

$$\begin{aligned}
\langle \mathcal{R}_{D,sec} \rangle^{(j=2)} &= f_1 + (e^2 + e'^2) f_2 + e^4 f_4 + e^2 e'^2 f_5 + e'^4 f_6 + \\
&\quad (e e' f_{10} + e^3 e' f_{11} + e e'^3 f_{12}) \cos(\tilde{\omega}' - \tilde{\omega}) \\
&\quad + e^2 e'^2 f_{17} \cos(2\tilde{\omega}' - 2\tilde{\omega}) \\
&\quad + O(e^5) \,, \\
\langle \mathcal{R}_{D,res} \rangle^{(j=2)} &= (e f_{27} + e^3 f_{28} + e e'^2 f_{29}) \cos(2\lambda' - \lambda - \tilde{\omega}) \\
&\quad + (e' f_{31} + e^2 e' f_{32} + e'^3 f_{33}) \cos(2\lambda' - \lambda - \tilde{\omega}') \\
&\quad + O(e^5) \,, \\
\langle \mathcal{R}_{E,res} \rangle^{(j=2)} &= (-2e' + e^2 e' + \frac{3}{2} e'^3) \cos(2\lambda' - \lambda - \tilde{\omega}') + O(e^5) \,, \\
\langle \mathcal{R}_{I,res} \rangle^{(j=2)} &= \left(-\frac{1}{2} e' + \frac{1}{4} e^2 e' + \frac{3}{8} e'^3 \right) \cos(2\lambda' - \lambda - \tilde{\omega}') + O(e^5) \,.
\end{aligned} \tag{B.1}$$

Here, subscript D is the direct part, and subscripts I and E represent the internal and external indirect contributions, respectively. Then, using Eqs. 12 and 13 to combine the terms, the complete disturbing functions are

$$\begin{aligned}
\langle \mathcal{R} \rangle^{(j=2)} &= \frac{\mu'}{a'} (f_1 + (e^2 + e'^2) f_2 + e^4 f_4 + e^2 e'^2 f_5 + e'^4 f_6 \\
&\quad + (e e' f_{10} + e^3 e' f_{11} + e e'^3 f_{12}) \cos(\tilde{\omega}' - \tilde{\omega}) \\
&\quad + e^2 e'^2 f_{17} \cos(2\tilde{\omega}' - 2\tilde{\omega}) \\
&\quad + (e f_{27} + e^3 f_{28} + e e'^2 f_{29}) \cos(2\lambda' - \lambda - \tilde{\omega}) \,, \\
&\quad + (e' f_{31} + e^2 e' f_{32} + e'^3 f_{33}) \cos(2\lambda' - \lambda - \tilde{\omega}') \\
&\quad + \alpha \left(-2e' + e^2 e' + \frac{3}{2} e'^3 \right) \cos(2\lambda' - \lambda - \tilde{\omega}')) + O(e^5)
\end{aligned} \tag{B.2}$$

$$\begin{aligned}
\langle \mathcal{R}' \rangle^{(j=2)} &= \frac{\mu}{a} (\alpha (f_1 + (e^2 + e'^2) f_2 + e^4 f_4 + e^2 e'^2 f_5 + e'^4 f_6 + \\
&\quad (e e' f_{10} + e^3 e' f_{11} + e e'^3 f_{12}) \cos(\tilde{\omega}' - \tilde{\omega}) \\
&\quad + e^2 e'^2 f_{17} \cos(2\tilde{\omega}' - 2\tilde{\omega}) \\
&\quad + (e f_{27} + e^3 f_{28} + e e'^2 f_{29}) \cos(2\lambda' - \lambda - \tilde{\omega}) \,. \\
&\quad + (e' f_{31} + e^2 e' f_{32} + e'^3 f_{33}) \cos(2\lambda' - \lambda - \tilde{\omega}')) \\
&\quad + \frac{1}{\alpha} \left(-\frac{1}{2} e' + \frac{1}{4} e^2 e' + \frac{3}{8} e'^3 \right) \cos(2\lambda' - \lambda - \tilde{\omega}')) + O(e^5)
\end{aligned} \tag{B.3}$$

The higher order 3:1 resonance is derived and used in the same way, and the components are

$$\begin{aligned}
\langle \mathcal{R}_{D,sec} \rangle^{(j=3)} &= f_1 + (e^2 + e'^2) f_2 + e^4 f_4 + e^2 e'^2 f_5 + e'^4 f_6 + \\
&\quad (e e' f_{10} + e^3 e' f_{11} + e e'^3 f_{12}) \cos(\tilde{\omega}' - \tilde{\omega}) \\
&\quad + e^2 e'^2 f_{17} \cos(2\tilde{\omega}' - 2\tilde{\omega}) \\
&\quad + O(e^5) \,, \\
\langle \mathcal{R}_{D,res} \rangle^{(j=3)} &= (e^2 f_{45} + e^4 f_{46} + e^2 e'^2 f_{47}) \cos(3\lambda' - \lambda - 2\tilde{\omega}) \\
&\quad + (e e' f_{49} + e^3 e' f_{50} + e e'^3 f_{51}) \cos(3\lambda' - \lambda - \tilde{\omega}' - \tilde{\omega}) \\
&\quad + (e'^2 f_{53} + e^2 e'^2 f_{54} + e'^4 f_{55}) \cos(3\lambda' - \lambda - 2\tilde{\omega}') \\
&\quad + O(e^5) \,, \\
\langle \mathcal{R}_{E,res} \rangle^{(j=3)} &= \left(-\frac{27}{8} e'^2 + \frac{27}{16} e^2 e'^2 + \frac{27}{8} e'^4 \right) \cos(3\lambda' - \lambda - 2\tilde{\omega}') \\
&\quad + O(e^5) \,, \\
\langle \mathcal{R}_{I,res} \rangle^{(j=3)} &= \left(-\frac{3}{8} e'^2 + \frac{3}{16} e^2 e'^2 + \frac{3}{8} e'^4 \right) \cos(3\lambda' - \lambda - 2\tilde{\omega}')) \\
&\quad + O(e^5) \,.
\end{aligned} \tag{B.4}$$

Using Eqs. 12 and 13 to combine the separate components into the complete disturbing functions gives

$$\begin{aligned}
\langle \mathcal{R} \rangle^{(j=3)} &= \frac{\mu'}{a'} (f_1 + (e^2 + e'^2) f_2 + e^4 f_4 + e^2 e'^2 f_5 + e'^4 f_6 \\
&\quad + (e e' f_{10} + e^3 e' f_{11} + e e'^3 f_{12}) \cos(\tilde{\omega}' - \tilde{\omega}) \\
&\quad + e^2 e'^2 f_{17} \cos(2\tilde{\omega}' - 2\tilde{\omega}) \\
&\quad + (e^2 f_{45} + e^4 f_{46} + e^2 e'^2 f_{47}) \cos(3\lambda' - \lambda - 2\tilde{\omega}) \,, \\
&\quad + (e e' f_{49} + e^3 e' f_{50} + e e'^3 f_{51}) \cos(3\lambda' - \lambda - \tilde{\omega}' - \tilde{\omega}) \\
&\quad + (e'^2 f_{53} + e^2 e'^2 f_{54} + e'^4 f_{55}) \cos(3\lambda' - \lambda - 2\tilde{\omega}')) \\
&\quad + \alpha \left(-\frac{27}{8} e'^2 + \frac{27}{16} e^2 e'^2 + \frac{27}{8} e'^4 \right) \cos(3\lambda' - \lambda - 2\tilde{\omega}')) + O(e^5)
\end{aligned} \tag{B.5}$$

$$\begin{aligned}
\langle \mathcal{R}' \rangle^{(j=3)} &= \frac{\mu}{a} (\alpha (f_1 + (e^2 + e'^2) f_2 + e^4 f_4 + e^2 e'^2 f_5 + e'^4 f_6 \\
&\quad + (e e' f_{10} + e^3 e' f_{11} + e e'^3 f_{12}) \cos(\tilde{\omega}' - \tilde{\omega}) \\
&\quad + e^2 e'^2 f_{17} \cos(2\tilde{\omega}' - 2\tilde{\omega}) \\
&\quad + (e^2 f_{45} + e^4 f_{46} + e^2 e'^2 f_{47}) \cos(3\lambda' - \lambda - 2\tilde{\omega}) \,. \\
&\quad + (e e' f_{49} + e^3 e' f_{50} + e e'^3 f_{51}) \cos(3\lambda' - \lambda - \tilde{\omega}' - \tilde{\omega}) \\
&\quad + (e'^2 f_{53} + e^2 e'^2 f_{54} + e'^4 f_{55}) \cos(3\lambda' - \lambda - 2\tilde{\omega}'))) \\
&\quad + \frac{1}{\alpha} \left(-\frac{3}{8} e'^2 + \frac{3}{16} e^2 e'^2 + \frac{3}{8} e'^4 \right) \cos(3\lambda' - \lambda - 2\tilde{\omega}')) + O(e^5)
\end{aligned} \tag{B.6}$$

The relations to find the coefficients f_k used in these equations are listed in Tabs. B.4., B.7., and B.11. of Murray & Dermott (1999), and the table containing the outcomes of Eq. 21 described in Sec. 2.3 is used to calculate their values.

Appendix C: Initial Conditions

This appendix includes the full sets of initial conditions, that were presented in context of Solar System moons in Fig. 4.

Table C.1. List of initial conditions used for experiments related to the 2:1 resonance. They are referred to in text by condition 1 to 9 from top to bottom.

n [rad/s]	e [-]	e′ [-]	ω [rad]	ω' [rad]	V_1 [rad]	v [rad/s]
2.9917923375519558e-05	0.007148944996094326	0.0025108557812175357	1.431521114700963	-1.7003570367784704	284476.0866303902	1.1642662573883272e-07
2.288787242225023e-05	0.0465694324229524	0.015865704366062272	1.5167669990371349	-1.6286176661370912	634405.1193012318	9.690760379799866e-09
2.2741641378975644e-05	0.02234906202445254	0.007841233596259371	0.7581147957492198	-2.382713545496043	629109.1182106257	3.532681838759125e-08
1.9811215223575074e-05	0.04789701327978026	0.016231750015167877	2.2051106876780144	-0.9284101349801053	3793.712279995337	-2.546594367695956e-09
1.8275142497595097e-05	0.03826255205224648	0.013292080932099907	-1.6603420978276222	1.4935514972063184	617984.2275131779	4.682777731464943e-08
1.7339728907784328e-05	0.03936006934787577	0.013198994659234211	2.198863125325634	-0.9313716705461401	733177.2455010877	-2.3488852229756494e-09
1.6639837630209837e-05	0.024571146519688388	0.00836445821780626	1.1620348197676142	-2.004867415036554	640989.7304544552	1.819052598701142e-08
1.1709375245210858e-05	0.0025741497491035326	0.0009337826771381625	0.5282981946420969	-2.6315987959074856	32662579.062531095	1.424623446597257e-07
1.0020346005665353e-05	0.01005743232339052	0.0035292568629203885	-2.426801843518189	0.7419772700679407	126017.91239963434	4.634487707118204e-08

Table C.2. List of initial conditions used for experiments related to the 3:1 resonance. They are referred to in text by condition 1 to 4 from top to bottom.

n [rad/s]	e [-]	e′ [-]	ω [rad]	ω' [rad]	V_1 [rad]	v [rad/s]
2.4240432602683356e-05	0.1417576964018174	0.18419754901038163	0.7107354788940278	-0.5530068560586314	-29206.385260124734	-5.7276345718907697e-08
2.26497814198837e-05	0.14876942817839128	0.19425960535542602	-2.6366756597363232	2.8043375188857054	-73857.8389118119	-3.958843333341195e-08
2.1348300326114678e-05	0.12789445336815528	0.15052345872194933	0.7627833972139063	1.9225867031203678	-61485.07831632349	-5.863018662856682e-08
2.005514116604567e-05	0.14558401697838041	0.14671019266328025	-2.013537892538594	-1.0798561610281396	-9610.893112922295	1.1488809211579698e-08

3

Conclusions and Recommendations

The results from Sec. 3 and 4 of the paper showed that resonance locking can significantly affect the evolution scenarios of moons. In Chapter 1, the main research question was divided into three sub-questions. These questions are answered here in Section 3.1, while some recommendations for future work can be found in Section 3.2.

3.1. Conclusions

One of the goals of this thesis was to develop a numerical model capable of combining the tidal effects with MMRs of varying order and the resonance locking mechanism. The development of this model was successful, although the resulting model is less efficient than the original version presented by Rovira-Navarro et al. (2021) that was built on. However, more detailed changes are simulated in this case, which introduced some behaviour that warranted further investigation, such as the process of capture into the resonance lock. Additionally, the evolution while on the wave was identified as another interesting phase. The questions introduced in Chapter 1 will therefore be answered in this context. Starting with the first two questions:

1. What are the possible outcomes of the capture, evolution, and escape under the influence of tidal migration, e-type MMR of first to second order, and tidal locking combined?;

2. How do the capture, evolution, and escape mechanisms in the extended model differ from classical results found in literature?

While the capture process of the MMRs themselves was not examined, the capture into the resonance lock has been studied in detail in Sec. 3.1 of the paper. The initial predictions made by Fuller et al. (2016) regarding required $|\mathrm{Im}(k_{2,p})|$ values for locking with the wave are accurate, when not taking the oscillations in mean motion into account. These oscillations cause the required value to be higher than expected, observed to even reach 50% past the prediction, resulting in the resonance lock to potentially being missed when not considering this effect. While this may still give the moons a jump in mean motion and eccentricity, the tidal migration rate will never be able to match that of the wave itself, and can therefore not be considered resonance locking. However, when the peak is sufficiently high, resonance locking does occur as described by Fuller et al. (2016), confirming that the mechanism works.

Escape from the MMR due to a resonance lock proved to be difficult to achieve in Sec. 3.2, requiring very high values for $|\mathrm{Im}(k_{2,p})|$ and unrealistic migration rates for the wave. However, this is the case for planets and moons similar to those in our Solar System. The picture may be different for bodies of much higher masses, therefore this mechanism may be the cause of MMRs breaking prematurely in massive exoplanetary systems. More realistic ranges of $|\mathrm{Im}(k_{2,p})|$ in particular were reached for $10M$ and $10m$ or higher, indicating that resonances may be broken by a passing mode in systems with massive gas giants or Brown dwarfs.

Finally, the evolution of a set of moons in MMR when encountering a resonance lock as examined in Sec. 3.3 results in an eccentricity up to double the original forced value after a million years (reaching the range 10^{-2}-10^{-1}). However, this growth is theoretically boundless for as long as the MMR and resonance lock last, possibly reaching escape values. This can result in much more intense heating for a period of time than when considering the constant Q_p model, as shown in Sec. 4.1. Furthermore, the secondary's migration rate

drastically increases. Once this resonance lock is passed, the two moons resume their interaction from prior to the passing wave with this increased eccentricity, which is slowly dampened back to the equilibrium value. When considering a single moon that is not in an MMR, the faster outward migration is similar to the multiple moon case mentioned previously, but its eccentricity will continue to be dampened, at a slightly faster rate than the constant Q_p model. A second effect of the resonance lock is the reduced growth in libration width compared to the lower $|\mathrm{Im}(k_{2,p})|$ from equilibrium tides, causing the MMRs to persist for a longer time.

> 3. What are the implications of these differences on some of the explanations for currently observed features of real systems in the Solar System?

As briefly touched upon in Sec. 4.1 of the paper, the mechanism can potentially explain the high free eccentricities of certain bodies. Particularly Titan, whose eccentricity is barely affected by the MMR with Hyperion, has a high free eccentricity that could be the result of a past or current MMR combined with a resonance lock. The latter is especially relevant for Titan as evidence pointing to this being the case exists. For bodies such as Ganymede, plausible explanations are given that solely require MMR encounters, but the combination with a resonance lock would help speed up the process. However, these results were found from a simplified toy model, assuming constant values for both $\mathrm{Im}(k_{2,s})$ and $\mathrm{Im}(k_{2,p})$, and may therefore not be entirely representative of the true evolution.

These periods of high eccentricity as a result from the coupled MMR and resonance locking interactions can result in periods of high heat production, which was shown in particular for Ganymede. Therefore, it provides an alternative explanation to some surface features.

Finally, using the conclusions above, the main question can be answered:

> How does the frequency-dependent Q_p affect the history and future of moons in MMRs?

Due to encounter with a mode, bodies may have migrated at much faster rates in the past, or could start to do so in the future. This can change formation scenarios, since a secondary may not be as old as initially assumed. In addition, these differences in migration rate change the history of MMRs encountered, meaning that some secondaries never encountered any of the MMRs that are assumed to be responsible for current surface and/or orbital features.

The outcome of these past MMR encounters can differ as well. It was shown that the lower Q_p results in a growth in eccentricity far past the initial value. MMRs previously assumed to not have been strong enough to pump the eccentricity to the value required from current observations, may meet these requirements when a resonance lock was or is involved. Conversely, a theoretical analysis demonstrated that the eccentricities that may be reached for different order MMRs do not differ as significantly as for the constant Q_p model, meaning that either a first- or high-order MMR can be responsible for approximately the same eccentricity. Furthermore, theoretically, the growth in eccentricity has no maximum value, therefore the eccentricities of secondaries presently affected by both —such as Titan and by extension Hyperion— could be increasing still. Values resulting in escape of moons could occur as well, but this requires the MMR and resonance lock to persist even for high eccentricities. However, should this be the case, some of the satellites may have eccentricities excited by MMRs with moons that are no longer present in the system. To examine the plausibility of this scenario, studies must be conducted that examine the evolution over several millions or billions of years.

Finally, due to the great implications the mechanism has on the past and future of satellites, the variable Q_p should be considered in models used by future studies, and not solely as a lower assumed constant Q_p. The latter is not an apt description of the resonance locking mechanism, and will result in underestimations in equilibrium eccentricities.

3.2. Recommendations

Some parts of the evolution in a resonance lock have been examined in this study. However, it would be impossible to study all possible scenarios in one thesis. Many uncertainties remain regarding the exact properties of modes, and how these would differ for different planets. Similarly, focused applications to existing bodies are required to confirm or reject this process as a possible explanation for some of their features. Therefore, a list of recommendations for future studies is given here, in descending order of importance.

- Improve the efficiency of the model.

As mentioned throughout the process, relatively small timesteps are required to reach a sufficiently low error in the results. Some steps have been taken to improve the models efficiency, such as calculating the Laplace coefficients only when a sufficient change in α is experienced. However, more work is required to allow for simulations in the order of millions to billions of years over which these processes occur. The ability to run the model for much more extended periods of time will demonstrate whether the theory of unending growth in eccentricity is true, and for how long this would continue.

- Include the changes in the moon's interior during integration.

  The original model includes detailed calculations that allow for changes in interior properties of the moons during run time. The current model is capable of doing so, but this has been ignored in this study. The interior properties are only calculated once at the start of integration. However, the large increase in eccentricity can result in a much hotter interior, potentially increasing the thickness of a liquid layer. Coupling the interior with the orbital evolution must be done to see how this affects the long-term evolution.

- Further examine the behaviour in a wider variety of scenarios.

  Firstly, how the interactions affect the capture probability of MMRs has not been examined. Specifically when close to both the resonance lock and the MMR, but also how the migration rate when already in a resonance lock affects the possibility of capture should be studied. The results could change the history of MMRs encountered and the possibility to be caught in some of these MMRs. This would again offer the possibility to provide alternative explanations to periods of heating in a moon's past.

  The long term evolution, but also capture and escape scenarios, should be examined in the context of different moon masses. In this study, the masses were kept constant and identical to one another, but cases with much heavier inner or outer moons likely affect the found behaviour. For example, a much more massive inner moon with a much smaller outer moon may affect the requirements for breaking resonance, and the minimum $|\mathrm{Im}(k_{2,p})|$ required to lock with the wave.

- Apply the model to existing Solar System bodies.

  Expanding on the varying masses, it would be interesting to examine an existing system in detail. Specifically moons that show inexplicable eccentricities and surface features, e.g. Ganymede or Titan, could benefit from these extended studies.

- Use future observations and models to better constrain mode characteristics and current migration rates.

  Following the discussion in Sec. 4.2 of the paper, results from future and past missions can help constrain some of the relevant properties of planets and moons. The ephemerides of Saturn's moons were better constrained using Cassini's data. The same opportunity will arise when JUICE and Europa Clipper are launched, where the former will be focused on Ganymede, and the latter on Europa. Aside from the ephemerides from these future missions, the gravity and tidal measurements of Juno have proved essential to improve models of the gas giants' interiors. It will continue to provide these types of data, which will help further constrain these models and potentially result in better estimates for the mode characteristics. As such, data from these missions should be examined to find moons that may currently be in a resonance lock, and improve on interior models.

- Apply the mechanisms to the Laplace resonance.

  One of the most interesting MMR interactions in our Solar System is the 3-body Laplace resonance of Io, Europa, and Ganymede. In this thesis, only two-body interactions have been examined, therefore not much can be said about the scenario with more moons in resonance. Specifically, how high should the peak be in this case? How are the eccentricities affected? Is it easier to break the resonance in this case? And would this break only the first pair, or all three?

- Extend the model to include the inclination.

  The focus here was on e-type MMRs which are most common in our Solar System, but the inclination can also affect the dissipation within the moon. It is therefore required to find how the resonance locking mechanism affects the inclination of the moons' orbits, such that this study can be applied to the past and current i-type MMRs in our Solar System, or exomoons that may be identified in the future.

- Examine even higher order MMRs.

  In this study, up to the 3:1 MMRs was examined, and it was shown that these react slightly differently from the 2:1 MMRs. Still, it would be interesting to examine the differences between the different order MMRs in more detail, and see whether the fractions of eccentricity growth hold true, but also to determine capture probabilities, or requirements to break resonance.

Therefore, this is only the start of the aspects that can and should be studied regarding the resonance locking mechanism. It would be beneficial for future studies to expand on the model developed here, and work with measurements of unprecedented precision to match the observations to results from the model.

A

Increased Order of Equations & Model Development

The extended model described in Sec. 2 of the paper includes higher order equations, and uses a much smaller time step than the original model. While some steps of the process have already been described in this section, in this appendix the higher order equations are discussed and derived in more detail in Section A.1 and A.2. These sections also include verification and validation for the relevant model components, and error analyses.

A.1. Tidal Migration

The code upon which is built only includes the relations for tidal migration up to second-order in eccentricity and the assumption is made that $\mathrm{Im}(k_{2,p})$ is negligible compared to $\mathrm{Im}(k_{2,s})$. The latter may not be true in case of resonance locking, and the former can cause large errors when the eccentricity becomes more significant or experiences a quicker growth —which may again occur in a resonance lock. Finally, for higher order MMRs it is advised to include higher order terms in eccentricity (Murray and Dermott, 1999, Ch. 6). Due to these reasons, the code will be adjusted to allow for these terms to be included. In this section, the tidal migration equations are presented and adjusted in subsection A.1.1, and the necessary adjustments made to the Love numbers are discussed in subsection A.1.2. These Love numbers are verified in subsection A.1.3, and the entire tidal part of the code is validated in subsection A.1.4. For these last two subsections, the initial conditions are as presented in Table A.1.

Table A.1: Settings used for verification & validation runs.

Initial mantle temperature [K]	1500
Initial eccentricity [-]	1e-4
Initial mean motion [rad/s]	1.0778e-4
Maxwell or Andrade rheology?	Maxwell
Interior model	Io
Heat flux approach	Fischer & Spohn
Im(k_2) (planet)	1e-5

A.1.1. Boué and Efroimsky's Equations

Boué and Efroimsky (2019) present a corrected set of equations that have been used in the code of Rovira-Navarro et al. (2021). In order to accommodate for the higher order terms, the $\mathrm{Im}(k_{2,s})$ must be calculated at different frequencies. Furthermore, no resonance lock will be included yet, therefore $\mathrm{Im}(k_{2,p})$ is assumed to be constant. The initial relations present in the original model were previously presented in Eqs. 2 and 3 of the paper. These are based on

$$
\begin{aligned}
\left(\frac{\mathrm{d}a}{\mathrm{d}t}\right)_{l=2} = \\
-3an\left(1-5e^2+\frac{63}{8}e^4\right)\left[\frac{m}{M}\left(\frac{R_p}{a}\right)^5(K_2(2n-2\dot{\theta}_p))+\frac{M}{m}\left(\frac{R_s}{a}\right)^5(K_2'(2n-2\dot{\theta}_s))\right] \\
-\frac{9}{4}ane^2\left(1+\frac{9}{4}e^2\right)\left[\frac{m}{M}\left(\frac{R_p}{a}\right)^5(K_2(n))+\frac{M}{m}\left(\frac{R_s}{a}\right)^5(K_2'(n))\right] \\
-\frac{3}{8}ane^2\left(1-\frac{1}{4}e^2\right)\left[\frac{m}{M}\left(\frac{R_p}{a}\right)^5(K_2(n-2\dot{\theta}_p))+\frac{M}{m}\left(\frac{R_s}{a}\right)^5(K_2'(n-2\dot{\theta}_s))\right] \text{ (Boué and Efroimsky, 2019, Eq. 143),} \\
-\frac{441}{8}ane^2\left(1-\frac{123}{28}e^2\right)\left[\frac{m}{M}\left(\frac{R_p}{a}\right)^5(K_2(3n-2\dot{\theta}_p))+\frac{M}{m}\left(\frac{R_s}{a}\right)^5(K_2'(3n-2\dot{\theta}_s))\right] \\
-\frac{867}{2}ane^4\left[\frac{m}{M}\left(\frac{R_p}{a}\right)^5(K_2(4n-2\dot{\theta}_p))+\frac{M}{m}\left(\frac{R_s}{a}\right)^5(K_2'(4n-2\dot{\theta}_s))\right] \\
-\frac{81}{8}ane^4\left[\frac{m}{M}\left(\frac{R_p}{a}\right)^5(K_2(2n))+\frac{M}{m}\left(\frac{R_s}{a}\right)^5(K_2'(2n))\right]+\mathcal{O}(i^2)+\mathcal{O}(i'^2)+\mathcal{O}(e^6)
\end{aligned}
\tag{A.1}
$$

$$
\begin{aligned}
\left(\frac{\mathrm{d}e}{\mathrm{d}t}\right)_{l=2} = \\
-ne\frac{m}{M}\left(\frac{R_p}{a}\right)^5\left[-\frac{3}{16}\left(1-\frac{e^2}{4}\right)(K_2(n-2\dot{\theta}_p))-\frac{3}{4}\left(1-\frac{21}{4}e^2\right)(K_2(2n-2\dot{\theta}_p))\right. \\
+\frac{147}{16}\left(1-\frac{179}{28}e^2\right)(K_2(3n-2\dot{\theta}_p))+\frac{867}{8}e^2(K_2(4n-2\dot{\theta}_p))+\frac{9}{8}\left(1+\frac{5}{4}e^2\right)(K_2(n)) \\
\left.+\frac{81}{16}e^2(K_2(2n))\right] \text{ (Boué and Efroimsky, 2019, Eq. 155),} \\
-ne\frac{M}{m}\left(\frac{R_s}{a}\right)^5\left[-\frac{3}{16}\left(1-\frac{e^2}{4}\right)(K_2'(n-2\dot{\theta}_s))-\frac{3}{4}\left(1-\frac{21}{4}e^2\right)(K_2'(2n-2\dot{\theta}_s))\right. \\
+\frac{147}{16}\left(1-\frac{179}{28}e^2\right)(K_2'(3n-2\dot{\theta}_s))+\frac{867}{8}e^2(K_2'(4n-2\dot{\theta}_s))+\frac{9}{8}\left(1+\frac{5}{4}e^2\right)(K_2'(n)) \\
\left.+\frac{81}{16}e^2(K_2'(2n))\right] \\
+\mathcal{O}(e^5)+\mathcal{O}(i^2)+\mathcal{O}(i'^2)
\end{aligned}
\tag{A.2}
$$

where K_2 is related to the imaginary Love number $\mathrm{Im}(k_2)$ as defined in Eq. 6 of the paper, and $\dot{\theta}_s$ is the rotational rate of the secondary.

Here, the full relations up to fourth-order will be included in the code. However, first some simplifications can be made. As discussed in Sec. 2.1 of the paper, it is assumed that the moons are locked to their primary and the same side faces it at all times, as such $n = \dot{\theta}_s$. $K_2'(\omega)$ can therefore be simplified, in this case to either $K_2'(n)$, $K_2'(2n)$, $K_2'(-n)$, or $K_2'(0)$. $K_2'(\omega)$ is an odd function (see Eq. 6 of the paper), as such $K_2'(-n)$=$-K_2'(n)$ and $K_2'(0)$=0 (Boué and Efroimsky, 2019). Applying this to Equation A.1 and A.2 results in Eqs. A.1 and A.2 of the paper.

Since the mean motion is used in the evolution, $\frac{\mathrm{d}a}{\mathrm{d}t}$ must first be converted to $\frac{\mathrm{d}n}{\mathrm{d}t}$, which can be done using the fact that $n = \sqrt{\frac{\mu}{a^3}}$ and therefore $\frac{\mathrm{d}n}{\mathrm{d}t}$ is as defined in Eq. 7 of the paper.

A.1.2. Love Numbers

Due to the inclusion of higher order terms in e, the Love number $k_{2,s}$ must now be calculated at different frequencies, specifically $\mathrm{Im}(k_{2,s}(-n))$ and $\mathrm{Im}(k_{2,s}(2n))$. The former is simply equal to $-\mathrm{Im}(k_{2,s}(n))$, but can be used as a check to make sure that the method is correct. The Love numbers were initially calculated in

the same function as the dissipation. In order to make sure that the dissipation is only found once, and only the calculation of the Love numbers is done multiple times, the part of the code that determines the Love numbers has been removed from the function that calculates the dissipation, and is now its own function. This function is called once prior to calculating the dissipation, and once prior to updating the orbit, allowing for multiple Love numbers for different frequencies to be found. Here, the distinction is still made between Maxwell and Andrade rheology. The way *calc_love* is called is illustrated in the model flowchart in Figure B.4 of Section B.3.

A.1.3. Verification: Love Numbers

For the Love numbers, the results should be that of an odd function, and correspond to the results expected from a Maxwell rheology. Since the initial mean motion times the number of seconds in a kilo year (and thus frequency) is far greater than 1, and will remain to be so as time progresses, the fraction of $\frac{\mathrm{Im}(k_{2,s}(\omega))}{\mathrm{Im}(k_{2,s}(2\omega))}$ should be approximately 2:

$$\begin{aligned} -\mathrm{Im}(k_2(\omega)) &= \frac{3}{2}\frac{J_U\eta_S\omega\tilde{\mu}}{1+(J_U\eta_S\omega)^2(\tilde{\mu}+1)^2} \\ -\mathrm{Im}(k_2(2\omega)) &= \frac{3}{2}\frac{J_U\eta_S 2\omega\tilde{\mu}}{1+(J_U\eta_S 2\omega)^2(\tilde{\mu}+1)^2} \text{ (Renaud and Henning, 2018, Tab. 3)} \\ \frac{\mathrm{Im}(k_{2,s}(\omega))}{\mathrm{Im}(k_{2,s}(2\omega))} &\approx \frac{1+4\omega^2}{2+2\omega^2} \approx 2 \end{aligned} \tag{A.3}$$

Looking at the results from the first three time steps presented in Table A.2 it can be seen that this holds.

Table A.2: Comparison of Love numbers at different frequencies per time step.

$\mathbf{Im(k_2(n))}$	$\mathbf{Im(k_2(-n))}$	$\mathbf{Im(k_2(2n))}$
-1.18182524496E-03	1.18182524496E-03	-5.91021376397E-04
-9.00956438933E-05	9.00956438933E-05	-4.50478220876E-05
-9.00969134867E-05	9.00969134867E-05	-4.50484568843E-05
...	...	...

A.1.4. Validation: Comparison to Rovira-Navarro et al. (2020)

When not including resonance locking —meaning that $|\mathrm{Im}(k_{2,p}(\omega))| \ll |\mathrm{Im}(k_{2,s}(\omega))|$— the adjustment made previously should not visibly affect the results. This is due to the eccentricity being small, causing higher order terms to be approximately 0, and the planet's tides being an order of magnitude lower than the moon's. Indeed, when comparing the results in Figure A.1 (assuming the set-up presented in Table A.1), no difference can be seen. An excerpt of the data can be found in Table A.3, and shows no difference either, since $e \approx 10^{-4}$ and $\left(10^{-4}\right)^3 = 10^{-12}$, which is beyond the precision shown in Tab. A.3. Note that this will differ for higher $|\mathrm{Im}(k_{2,p}(\omega))|$ as a result of the frequency dependency introduced by dynamical tides, and the increase in e that may follow.

Table A.3: Comparison of results from the baseline and extended model.

Base			**Extended**		
Time [Myr]	**e**	**Period**	**Time [Myr]**	**e**	**Period**
1.00000E-03	1.25995E-04	6.74742E-01	1.00000E-03	1.25995E-04	6.74742E-01
6.00000E-03	1.26028E-04	6.74819E-01	6.00000E-03	1.26028E-04	6.74819E-01
1.00600E+00	1.32822E-04	6.89630E-01	1.00600E+00	1.32822E-04	6.89630E-01
2.00600E+00	1.39863E-04	7.03456E-01	2.00600E+00	1.39863E-04	7.03457E-01
3.00600E+00	1.47188E-04	7.16438E-01	3.00600E+00	1.47188E-04	7.16438E-01
...	...	...	...	...	...

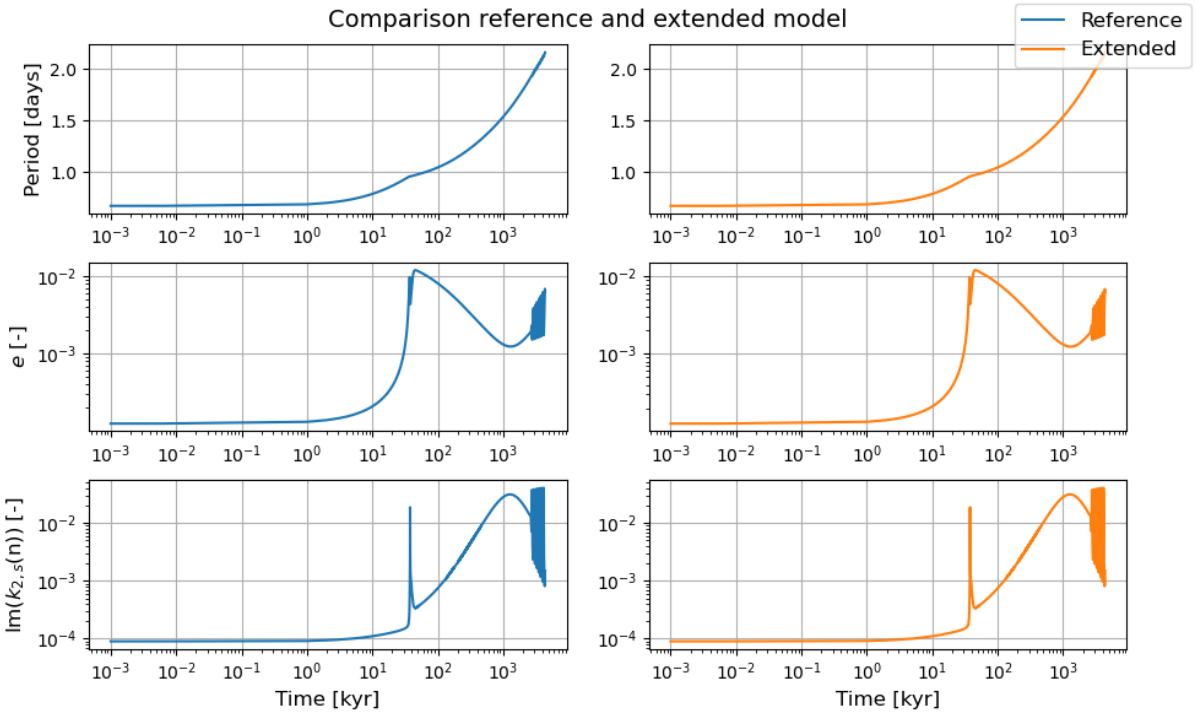

Figure A.1: Results from base run with the model in Rovira-Navarro et al. (2021) (left) and the results from the extended model (right). The results are identical.

A.2. Mean Motion Resonance

A 2:1 MMR was already modelled in the original version of the code of Rovira-Navarro et al. (2021), but is again accurate up to $\mathcal{O}(e)$. In this section, the equations will be expanded to include terms until the fourth-order in subsection A.2.1. The equations for the 3:1 and 4:1 resonances that are both present in the extended model are derived in subsection A.2.2, but due to difficulties finding suitable initial conditions the 4:1 resonance is not used further. The new additions are verified in subsection A.2.3, and validated against existing models in subsection A.2.4. Finally, the methods of finding initial conditions for the 2:1 and 3:1 MMR are discussed in subsection A.2.5.

A.2.1. Equations

The relations here are derived based on the method presented in Yoder and Peale (1981), who make use of $\frac{\mathrm{d}n}{\mathrm{d}t}$ and $\frac{\mathrm{d}p}{\mathrm{d}t}$ (where $p = e\exp(-i\tilde{\omega})$), and these derivatives can be found using Eqs. 10 and 11 of the paper. The disturbing function was found as described in App. B. Starting with the 2:1 resonance, which can directly be checked with results from the base code of Rovira-Navarro et al. for validity, the factors f_k in Eqs. B.2 and B.3

of the paper are

$$
\begin{aligned}
f_1 &= \frac{1}{2} A_j \\
f_2 &= \frac{1}{8}\left[-4j^2 + 2\alpha D + \alpha^2 D^2\right] A_j \\
f_4 &= \frac{1}{128}\left[-9j^2 + 16j^4 - 8j^2\alpha D - 8j^2\alpha^2 D^2 + 4\alpha^3 D^3 + \alpha^4 D^4\right] A_j \\
f_5 &= \frac{1}{32}\left[16j^4 + 4\alpha D - 16j^2\alpha D + 14\alpha^2 D^2 - 8j^2\alpha^2 D^2 + 8\alpha^3 D^3 \right. \\
&\qquad \left. + \alpha^4 D^4\right] A_j \\
f_6 &= \frac{1}{128}\left[-17j^2 + 16j^4 + 24\alpha D - 24j^2\alpha D + 36\alpha^2 D^2 - 8j^2\alpha^2 D^2 \right. \\
&\qquad \left. + 12\alpha^3 D^3 + \alpha^4 D^4\right] A_j \\
f_{10} &= \frac{1}{4}\left[2 + 6j + 4j^2 - 2\alpha D - \alpha^2 D^2\right] A_{j+1} \\
f_{11} &= \frac{1}{32}\left[-6j - 26j^2 - 36j^3 - 16j^4 + 6j\alpha D + 12j^2\alpha D - 4\alpha^2 D^2 \right. \\
&\qquad \left. + 7j\alpha^2 D^2 + 8j^2\alpha^2 D^2 + 8j^2\alpha^2 D^2 - 6\alpha^3 D^3 - \alpha^4 D^4\right] A_{j+1} \\
f_{12} &= \frac{1}{32}\left[4 + 2j - 22j^2 - 36j^3 - 16j^4 - 4\alpha D + 22j\alpha D + 20j^2\alpha D \right. \\
&\qquad \left. - 22\alpha^2 D^2 + 7j\alpha^2 D^2 + 8j^2\alpha^2 D^2 + 8j^2\alpha^2 D^2 - 10\alpha^3 D^3 - \alpha^4 D^4\right] A_{j+1} \\
f_{17} &= \frac{1}{64}\left[12 + 64j + 109j^2 + 72j^3 + 16j^4 - 12\alpha D - 28j\alpha D - 16j^2\alpha D \right. \\
&\qquad \left. + 6\alpha^2 D^2 - 14j\alpha^2 D^2 - 8j^2\alpha^2 D^2 + 8\alpha^3 D^3 + \alpha^4 D^4\right] A_{j+2} \\
f_{27} &= \frac{1}{2}\left[-2j - \alpha D\right] A_j \\
f_{28} &= \frac{1}{16}\left[2j - 10j^2 + 8j^3 + 3\alpha D - 7j\alpha D + 4j^2\alpha D - 2\alpha^2 D^2 - 2j\alpha^2 D^2 \right. \\
&\qquad \left. - \alpha^3 D^3\right] A_j \\
f_{29} &= \frac{1}{8}\left[8j^3 - 2\alpha D - 4j\alpha D + 4j^2\alpha D - 4\alpha^2 D^2 - 2j\alpha^2 D^2 - \alpha^3 D^3\right] A_j \\
f_{31} &= \frac{1}{2}\left[-1 + 2j + \alpha D\right] A_{j-1} \\
f_{32} &= \frac{1}{8}\left[4 - 16j + 20j^2 - 8j^3 - 4\alpha D + 12j\alpha D - 4j^2\alpha D + 3\alpha^2 D^2 \right. \\
&\qquad \left. + 2j\alpha^2 D^2 + \alpha^3 D^3\right] A_{j-1} \\
f_{33} &= \frac{1}{16}\left[-2 - j + 10j^2 - 8j^3 + 2\alpha D + 9j\alpha D - 4j^2\alpha D + 5\alpha^2 D^2 \right. \\
&\qquad \left. + 2j\alpha^2 D^2 + \alpha^3 D^3\right] A_{j-1}
\end{aligned}
\tag{A.4}
$$

(Murray and Dermott, 1999, Tab. B.4. & B.7.).

For a 2:1 MMR $j = 2$, D is the differential operator $\frac{\mathrm{d}}{\mathrm{d}\alpha}$ and A_j is found from $b_{1/2}^{(j)}(\alpha)$, which is defined in Eq. 21. The quickest way to solve this is by numerical integration. For example, when in vicinity of the 2:1 MMR, $\alpha \approx 0.63$ (Yoder and Peale, 1981), and $b_{1/2}^{(2)}(0.63) \approx 0.3654$. The derivatives of the Laplace coefficients can be found using the following relations originally given in Brouwer and Clemence (1961):

$$b_s^{(-j)} = b_s^{(j)} \text{ (Murray and Dermott, 1999, Eq.6.69),} \tag{A.5}$$

$$D b_s^{(j)} = s\left(b_{s+1}^{(j-1)} - 2\alpha b_{s+1}^{(j)} + b_{s+1}^{(j+1)}\right) \text{ (Murray and Dermott, 1999, Eq.6.70),} \tag{A.6}$$

$$
\begin{aligned}
D^n b_s^{(j)} = s\Big(&D^{n-1} b_{s+1}^{(j-1)} - 2\alpha D^{n-1} b_{s+1}^{(j)} \\
&+ D^{n-1} b_{s+1}^{(j+1)} - 2(n-1) D^{n-2} b_{s+1}^{(j)}\Big)
\end{aligned}
\text{ (Murray and Dermott, 1999, Eq.6.71).} \tag{A.7}
$$

Rovira-Navarro et al. (2021), following Yoder and Peale (1981), assume the factors f_i are constant, and therefore that α does not change. When placing the moons close to (but not in) MMR, α may change over time

as the moons move towards resonance. To accommodate for this, the factors are computed during run time. Furthermore, when a factor includes a fourth derivative, $b_s^{(j)}$ must be calculated up to $b_{(s+4)}^{j\pm4}$. Since Eq. 21 can only be solved numerically or as a sum, the simplest solution is to discretely solve the equation for all possible values of α, and interpolate to find the values for the exact input α. This will be compatible with $j = 2,3,4$. The data table which is fed into the code has the following format:

$$\begin{pmatrix} b_{1/2}^{(0)}(0) & \cdots & b_{1/2}^{(8)}(0) & b_{3/2}^{(0)}(0) & \cdots & b_{3/2}^{(8)}(0) & \cdots & b_{9/2}^{(0)}(0) & \cdots & b_{9/2}^{(8)}(0) \\ \vdots & \ddots & \vdots & \vdots & \ddots & \vdots & \ddots & \vdots & \ddots & \vdots \\ b_{1/2}^{(0)}(0.9999) & \cdots & b_{1/2}^{(8)}(0.9999) & b_{3/2}^{(0)}(0.9999) & \cdots & b_{3/2}^{(8)}(0.9999) & \cdots & b_{9/2}^{(0)}(0.9999) & \cdots & b_{9/2}^{(8)}(0.9999) \end{pmatrix} \tag{A.8}$$

Since the coefficients must be found for $b_{(s+4)}^{j\pm4}$, Equation A.5 can be exploited to limit j to the range 0 to 8 in the array. These values are found until $s+4 = 9/2$. This results in an array of 10,000 rows (a step size of ~1e-04 for α) and 45 columns, excluding α, and is accurate up to the eighth decimal after linear interpolation.

Next, Eqs. 10 and 11 must be applied to Eqs. B.2 and B.3 of the paper. For $\frac{\mathrm{d}n}{\mathrm{d}t}$ and $\frac{\mathrm{d}n'}{\mathrm{d}t}$, this gives

$$\begin{aligned} \frac{\mathrm{d}n}{\mathrm{d}t} = \frac{3n'^2m'}{\alpha^2 M}\Bigg(\Bigg(f_{33}e'^3 + \frac{3\alpha}{2}e'^3 + f_{32}e^2e' + \alpha e^2e' + f_{31}e' - 2\alpha e'\Bigg)\sin\left(-2\lambda' + \lambda + \tilde{\omega}'\right) \\ + \left(f_{28}e^3 + f_{29}ee'^2 + f_{27}e\right)\sin\left(-2\lambda' + \lambda + \tilde{\omega}\right)\Bigg) + \mathscr{O}(e^5) \end{aligned}, \tag{A.9}$$

$$\begin{aligned} \frac{\mathrm{d}n'}{\mathrm{d}t} = -\frac{6n'^2m}{M\alpha^2}\Bigg(\Bigg(\alpha^2 f_{33}e'^3 + \frac{3}{8}e'^3 + \alpha^2 f_{32}e^2e' + \alpha^2 f_{31}e' + \frac{1}{4}e^2e' - \frac{1}{2}e'\Bigg)\sin\left(-2\lambda' + \lambda + \tilde{\omega}'\right) \\ + \alpha^2\left(f_{28}e^3 + f_{29}ee'^2 + f_{27}e\right)\sin\left(-2\lambda' + \lambda + \tilde{\omega}\right)\Bigg) + \mathscr{O}(e^5) \end{aligned}. \tag{A.10}$$

The following relations were used to simplify the equation: $a = \alpha a'$, $a' = \left(\frac{\mu_\mathrm{p}}{n'^2}\right)^{1/3}$, $\mu_\mathrm{p} = GM$, $\mu = Gm$, and $\mu' = Gm'$.

In order to find $\frac{\mathrm{d}p}{\mathrm{d}t}$ and $\frac{\mathrm{d}p'}{\mathrm{d}t}$, the disturbing functions must first be converted to exponential functions, since $q = e\exp(i\tilde{\omega})$. This means that

$$\begin{aligned} \langle\mathscr{R}\rangle^{(j=2)} = \frac{\mu'}{a'}\Bigg(f_1 + \left(e^2 + e'^2\right)f_2 + e^4 f_4 + e^2e'^2 f_5 + e'^4 f_6 \\ + \left(ee' f_{10} + e^3e' f_{11} + ee'^3 f_{12}\right)\left(\frac{\exp i(-\tilde{\omega}' + \tilde{\omega}) + \exp -i(-\tilde{\omega}' + \tilde{\omega})}{2}\right) \\ + \left(e^2e'^2 f_{17}\right)\left(\frac{\exp i(-2\tilde{\omega}' + 2\tilde{\omega}) + \exp -i(-2\tilde{\omega}' + 2\tilde{\omega})}{2}\right) \\ + \left(ef_{27} + e^3 f_{28} + ee'^2 f_{29}\right)\left(\frac{\exp i(-2\lambda' + \lambda + \tilde{\omega}) + \exp -i(-2\lambda' + \lambda + \tilde{\omega})}{2}\right) \\ + \left(e' f_{31} + e^2e' f_{32} + e'^3 f_{33}\right)\left(\frac{\exp i(-2\lambda' + \lambda + \tilde{\omega}') + \exp -i(-2\lambda' + \lambda + \tilde{\omega}')}{2}\right) \\ + \alpha\left(-2e' + e^2e' + \frac{3}{2}e'^3\right)\left(\frac{\exp i(-2\lambda' + \lambda + \tilde{\omega}') + \exp -i(-2\lambda' + \lambda + \tilde{\omega}')}{2}\right)\Bigg) + \mathscr{O}(e^5) \end{aligned} \tag{A.11}$$

$$\begin{aligned}\langle \mathscr{R}' \rangle^{(j=2)} = \frac{\mu}{a}\Bigg(\alpha\Bigg(f_1 + \left(e^2 + e'^2\right) f_2 + e^4 f_4 + e^2 e'^2 f_5 + e'^4 f_6 \\ + \left(e e' f_{10} + e^3 e' f_{11} + e e'^3 f_{12}\right)\left(\frac{\exp i(-\tilde{\omega}' + \tilde{\omega}) + \exp -i(-\tilde{\omega}' + \tilde{\omega})}{2}\right) \\ + \left(e^2 e'^2 f_{17}\right)\left(\frac{\exp i(-2\tilde{\omega}' + 2\tilde{\omega}) + \exp -i(-2\tilde{\omega}' + 2\tilde{\omega})}{2}\right) \\ + \left(e f_{27} + e^3 f_{28} + e e'^2 f_{29}\right)\left(\frac{\exp i(-2\lambda' + \lambda + \tilde{\omega}) + \exp -i(-2\lambda' + \lambda + \tilde{\omega})}{2}\right) \\ + \left(e' f_{31} + e^2 e' f_{32} + e'^3 f_{33}\right)\left(\frac{\exp i(-2\lambda' + \lambda + \tilde{\omega}') + \exp -i(-2\lambda' + \lambda + \tilde{\omega}')}{2}\right)\Bigg) \\ + \frac{1}{\alpha}\left(-\frac{1}{2}e' + \frac{1}{4}e^2 e' + \frac{3}{8}e'^3\right)\left(\frac{\exp i(-2\lambda' + \lambda + \tilde{\omega}') + \exp -i(-2\lambda' + \lambda + \tilde{\omega}')}{2}\right)\Bigg) + \mathscr{O}(e^5)\end{aligned} \tag{A.12}$$

and applying Eq. 11 gives

$$\begin{aligned}\frac{\mathrm{d}p}{\mathrm{d}t} = -\frac{i m' n'^2}{n\alpha^2 M}\Big(\left(f_{11} e^2 e' + f_{12} e'^3 + f_{10} e'\right)\exp -i\tilde{\omega}' \\ + 2 f_{17} e e'^2 \exp -2i\tilde{\omega}' \exp i\tilde{\omega} \\ + \left(f_{32} e^2 + f_{33} e'^2 + f_{31}\right)\exp i(-2\lambda' + \lambda)\Big) + \mathscr{O}(e^5)\end{aligned} \tag{A.13}$$

$$\begin{aligned}\frac{\mathrm{d}p'}{\mathrm{d}t} = -\frac{i m n'}{M}\Big(\left(f_{11} e^3 + f_{12} e e'^2 + f_{10} e\right)\exp -i\tilde{\omega} \\ + 2 f_{17} e^2 e' \exp -2i\tilde{\omega} \exp i\tilde{\omega}' \\ + \left(f_{32} e^2 + f_{33} e'^2 + f_{31}\right)\exp i(-2\lambda' + \lambda) \\ + \frac{1}{\alpha^2}\left(-\frac{1}{2} + \frac{1}{4}e^2 + \frac{3}{8}e'^2\right)\exp i(-2\lambda' + \lambda)\Big) + \mathscr{O}(e^5)\end{aligned} \tag{A.14}$$

The total derivatives of these elements are combined using Eqs. 16 and 17 to find the complete equations of motion.

The resulting $\frac{\mathrm{d}p}{\mathrm{d}t}$ and $\frac{\mathrm{d}p'}{\mathrm{d}t}$ are more complex than in Yoder and Peale (1981), and will be solved numerically rather than analytically. As a consequence, the "fast-changing variables" —i.e. $\tilde{\omega}$, $\tilde{\omega}'$, and V_1— are not removed from the equations, and must be integrated along with n, n', p, and p'. $\tilde{\omega}$ and $\tilde{\omega}'$ follow directly from p and p' along with e and e', as the former are the arguments of p and p', while the latter are the moduli. This leaves V_1. V_1 is the resonant argument, and is equal to $-j\lambda' + \lambda$. Yoder and Peale (1981) give that $\frac{\mathrm{d}V_1}{\mathrm{d}t} = \nu$, and $\frac{\mathrm{d}\nu}{\mathrm{d}t} = -j\frac{\mathrm{d}n'}{\mathrm{d}t} + \frac{\mathrm{d}n}{\mathrm{d}t}$ (see also Eq. 19 of the paper), where in this example $j = 2$. This can be used to integrate the value along with the aforementioned variables. It should be noted that initial conditions are now required for $\tilde{\omega}$, $\tilde{\omega}'$, and V_1 as well.

A second consequence of the "fast-changing variables" not being removed, is that the integration time step must be reduced significantly. For example, Lari et al. (2020) have used a step size of 11 days, which is significantly shorter than the current 10^3 years in Rovira-Navarro et al. (2021). The integration of the orbit is therefore embedded within the integration of the interior properties, since these are still changing very slowly. An analysis of the error as a function of time step can be found in Figure A.2. The largest time step of minimum error is around $8 \cdot 10^{-10}$ Myr, which corresponds to approximately every 7 hours. This step size is much smaller than before, limiting the maximum amount of time that can be examined with a single run.

The integration of the orbit uses the Runge-Kutta 4 integration scheme:

$$\begin{aligned}y_{n+1} = y_n + \frac{1}{6}\Delta t\left(k_1 + 2k_2 + 2k_3 + k_4\right) \\ k_1 = f\left(t_n, y_n\right) \\ k_2 = f\left(t_n + \frac{\Delta t}{2}, y_n + \Delta t\frac{k_1}{2}\right) \\ k_3 = f\left(t_n + \frac{\Delta t}{2}, y_n + \Delta t\frac{k_2}{2}\right) \\ k_4 = f\left(t_n + \Delta t, y_n + \Delta t k_3\right)\end{aligned} \tag{A.15}$$

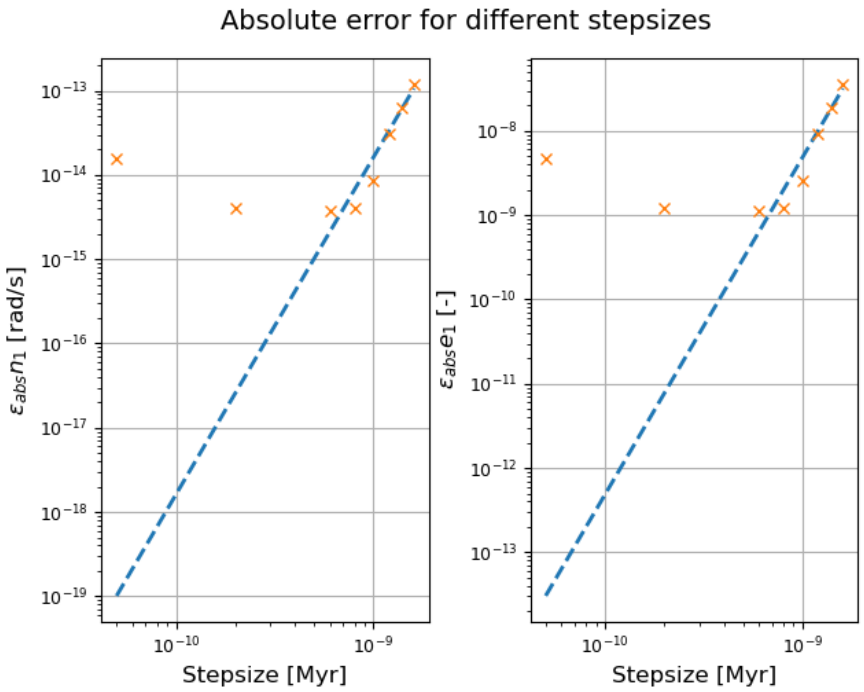

Figure A.2: Behaviour of the absolute error as a function of time step in Myr. The optimum time step is approximately $8 \cdot 10^{-10}$ Myr, which corresponds to approximately 7 h.

where the states to be integrated can be found in Eq. 20 of the paper.

Finally, the change in α tends to be small in a single time step. It may therefore not be necessary to recalculate the Laplace coefficients or search through the table every step, but only if α has changed sufficiently compared to an initial value. The results can be found in Figure A.3, which shows the errors in behaviour for different $\Delta\alpha$, specifically the amplitude of n (left) and dominant frequency (right). For $\Delta\alpha = 10^{-6}$ the error in amplitude is significantly lower than $\sim 10^{-5}$, which is the order of n values considered in this thesis. Similarly, the error in dominant frequency of the evolution is much lower than the magnitude of the orbital elements n and e typically assumed. This gives an improvement in run time of a factor 1.5 for this specific case, but this depends entirely on the rate at which α changes for a specific problem.

A.2.2. Higher Order Resonances

The higher order resonances that have been included in the model are the 3:1 and the 4:1 resonances. However, for the 4:1 MMR it proved challenging to find initial conditions that resulted in resonance, and it has therefore not been analysed further. Regardless, it is present in the model, and its equations of motion are presented at the end of this section. The process of the derivation for the equations of motion of both higher order resonances is the same as for the 2:1 resonance discussed in subsection A.2.1. Starting from the final disturbing functions for the 3:1 MMR in Eqs. B.5 and B.6 of the paper, applying Eqs. 10 and 11 results in the time derivatives:

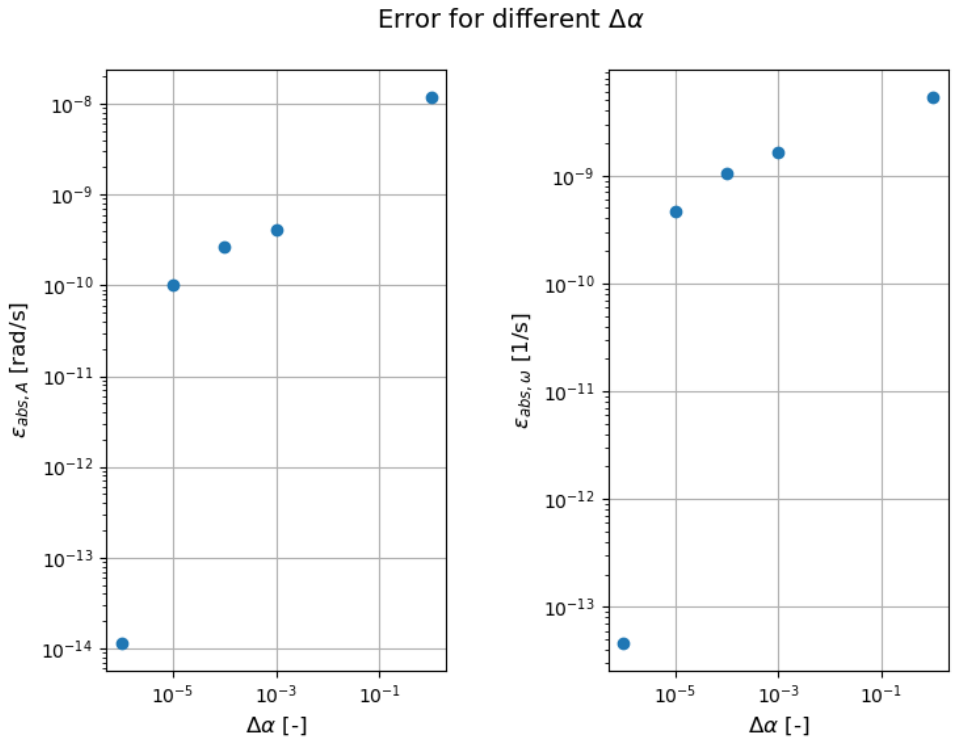

Figure A.3: Comparison of the absolute error in amplitude of n (left) and dominant frequency of the behaviour (right) for different $\Delta\alpha$. $\Delta\alpha = 10^{-6}$ results in the lowest error, and therefore is closest to the reference case for which the coefficients are recalculated at every step in terms of behaviour.

$$\begin{aligned}\frac{\mathrm{d}n}{\mathrm{d}t} = \frac{3n'^2m'}{\alpha^2 M}\Big(&\left(f_{45}e^2 + f_{46}e^4 + f_{47}e^2e'^2\right)\sin\left(-3\lambda' + \lambda + 2\tilde{\omega}\right)\\ &+ \left(f_{49}ee' + f_{50}e^3e' + f_{51}ee'^3\right)\sin\left(-3\lambda' + \lambda + \tilde{\omega} + \tilde{\omega}'\right)\\ &+ \left(f_{53}e'^2 + f_{54}e^2e'^2 + f_{55}e'^4\right)\sin\left(-3\lambda' + \lambda + 2\tilde{\omega}'\right)\\ &+ \alpha\left(-\frac{27}{8}e'^2 + \frac{27}{16}e^2e'^2 + \frac{27}{8}e'^4\right)\sin\left(-3\lambda' + \lambda + 2\tilde{\omega}'\right)\Big) + \mathcal{O}(e^5)\end{aligned}, \tag{A.16}$$

$$\begin{aligned}\frac{\mathrm{d}n'}{\mathrm{d}t} = -\frac{9n'^2m'}{\alpha M}\Big(&\alpha\Big(\left(f_{45}e^2 + f_{46}e^4 + f_{47}e^2e'^2\right)\sin\left(-3\lambda' + \lambda + 2\tilde{\omega}\right)\\ &+ \left(f_{49}ee' + f_{50}e^3e' + f_{51}ee'^3\right)\sin\left(-3\lambda' + \lambda + \tilde{\omega} + \tilde{\omega}'\right)\\ &+ \left(f_{53}e'^2 + f_{54}e^2e'^2 + f_{55}e'^4\right)\sin\left(-3\lambda' + \lambda + 2\tilde{\omega}'\right)\Big)\\ &+ \frac{1}{\alpha}\left(-\frac{3}{8}e'^2 + \frac{3}{16}e^2e'^2 + \frac{3}{8}e'^4\right)\sin\left(-3\lambda' + \lambda + 2\tilde{\omega}'\right)\Big) + \mathcal{O}(e^5)\end{aligned}, \tag{A.17}$$

$$\begin{aligned}\frac{\mathrm{d}p}{\mathrm{d}t} = -\frac{im'n'^2}{n\alpha^2 M}\Big(&\left(f_{10}e' + f_{11}e^2e' + f_{12}e'^3\right)\exp -i\tilde{\omega}' \\ &+2f_{17}ee'^2\exp -2i\tilde{\omega}'\exp i\tilde{\omega} \\ &+2\left(f_{45}e + f_{46}e^3 + f_{47}ee'^2\right)\exp i(-3\lambda' + \lambda)\exp i\tilde{\omega} \\ &+\left(f_{49}e' + f_{50}e^2e' + f_{51}e'^3\right)\exp i(-3\lambda' + \lambda)\exp i\tilde{\omega}'\Big) \\ &+\mathcal{O}(e^5)\end{aligned} \tag{A.18}$$

$$\begin{aligned}\frac{\mathrm{d}p'}{\mathrm{d}t} = -\frac{imn'}{M}\Bigg(&\left(f_{10}e + f_{11}e^3 + f_{12}ee'^2\right)\exp -i\tilde{\omega} + \\ &+2f_{17}e^2e'\exp -2i\tilde{\omega}\exp i\tilde{\omega}' \\ &+\left(f_{49}e + f_{50}e^3 + f_{51}ee'^2\right)\exp i(-3\lambda' + \lambda)\exp i\tilde{\omega} \\ &+2\left(f_{53}e' + f_{54}e^2e' + f_{55}e'^3\right)\exp i(-3\lambda' + \lambda)\exp i\tilde{\omega}' \\ &+\frac{2}{\alpha^2}\left(-\frac{3}{8}e' + \frac{3}{16}e^2e' + \frac{3}{8}e'^3\right)\exp i(-3\lambda' + \lambda)\exp i\tilde{\omega}'\Bigg) \\ &+\mathcal{O}(e^5)\end{aligned} \tag{A.19}$$

Aside from the factors up to f_{17} associated with the secular terms, previously defined in Equation A.4, the extra relevant factors f_k corresponding to the 3:1 resonance are:

$$\begin{aligned}f_{45} &= \frac{1}{8}\left[-5j + 4j^2 - 2\alpha D + 4j\alpha D + \alpha^2 D^2\right]A_j \\ f_{46} &= \frac{1}{96}\left[22j - 64j^2 + 60j^3 - 16j^4 + 16\alpha D - 46j\alpha D + 48j^2\alpha D\right. \\ &\quad \left. -16j^3\alpha D - 12\alpha^2 D^2 + 9j\alpha^2 D^2 + 4j\alpha^3 D^3 + \alpha^4 D^4\right]A_j \\ f_{47} &= \frac{1}{32}\left[20j^3 - 16j^4 - 4\alpha D - 2j\alpha D + 16j^2\alpha D -\right. \\ &\quad \left. 16j^3\alpha D - 2\alpha^2 D^2 + 11j\alpha^2 D^2 + 4\alpha^3 D^3 + 4j\alpha^3 D^3 + \alpha^4 D^4\right]A_j \\ f_{49} &= \frac{1}{4}\left[-2 + 6j - 4j^2 + 2\alpha D - 4j\alpha D - \alpha^2 D^2\right]A_{j-1} \\ f_{50} &= \frac{1}{32}\left[20 - 86j + 126j^2 - 76j^3 + 16j^4 - 20\alpha D\right. \\ &\quad +74j\alpha D - 64j^2\alpha D + 16j^3\alpha D + 14\alpha^2 D^2 \\ &\quad \left. -17j\alpha^2 D^2 - 2\alpha^3 D^3 - 4j\alpha^3 D^3 - \alpha^4 D^4\right]A_{j-1} \\ f_{51} &= \frac{1}{32}\left[-4 + 2j + 22j^2 - 36j^3 + 16j^4 + 4\alpha D\right. \\ &\quad +6j\alpha D - 32j^2\alpha D + 16j^3\alpha D - 2\alpha^2 D^2 \\ &\quad \left. -19j\alpha^2 D^2 - 6\alpha^3 D^3 - 4j\alpha^3 D^3 - \alpha^4 D^4\right]A_{j-1} \\ f_{53} &= \frac{1}{8}\left[2 - 7j + 4j^2 - 2\alpha D + 4j\alpha D + \alpha^2 D^2\right]A_{j-2} \\ f_{54} &= \frac{1}{32}\left[-32 + 144j - 184j^2 + 92j^3 - 16j^4 + 32\alpha D\right. \\ &\quad -102j\alpha D + 80j^2\alpha D - 16j^3\alpha D - 16\alpha^2 D^2 \\ &\quad \left. +25j\alpha^2 D^2 + 4\alpha^3 D^3 + 4j\alpha^3 D^3 + \alpha^4 D^4\right]A_{j-2} \\ f_{55} &= \frac{1}{96}\left[12 - 14j - 40j^2 + 52j^3 - 16j^4\right. \\ &\quad -12\alpha D - 10j\alpha D + 48j^2\alpha D - 16j^3\alpha D + 6\alpha^2 D^2 \\ &\quad \left. +27j\alpha^2 D^2 + 8\alpha^3 D^3 + 4j\alpha^3 D^3 + \alpha^4 D^4\right]A_{j-2}\end{aligned} \tag{A.20}$$

(Murray and Dermott, 1999, Tab. B.11.).

The disturbing function of the 4:1 MMR is:

$$\begin{aligned}\langle \mathscr{R} \rangle^{(j=4)} = \frac{\mu'}{a'}(&f_1 + (e^2+e'^2)f_2 + e^4 f_4 + e^2 e'^2 f_5 + e'^4 f_6 + (ee' f_{10} + e^3 e' f_{11} + ee'^3 f_{12})\cos(\tilde{\omega}' - \tilde{\omega}) \\ &+ e^2 e'^2 f_{17}\cos(2\tilde{\omega}' - 2\tilde{\omega}) + e^3 f_{82}\cos(4\lambda' - \lambda - 3\tilde{\omega}) \\ &+ e^2 e' f_{83}\cos(4\lambda' - \lambda - \tilde{\omega}' - 2\tilde{\omega}) + ee'^2 f_{84}\cos(4\lambda' - \lambda - 2\tilde{\omega}' - \tilde{\omega}) + e'^3 f_{85}\cos(4\lambda' - \lambda - 3\tilde{\omega}') \\ &+ \alpha(-\frac{16}{3}e'^3\cos(4\lambda' - \lambda - 3\tilde{\omega}'))) + \mathscr{O}(e^5)\end{aligned} \tag{A.21}$$

$$\begin{aligned}\langle \mathscr{R}' \rangle^{(j=4)} = \frac{\mu}{a}(&\alpha(f_1 + (e^2+e'^2)f_2 + e^4 f_4 + e^2 e'^2 f_5 + e'^4 f_6 + (ee' f_{10} + e^3 e' f_{11} + ee'^3 f_{12})\cos(\tilde{\omega}' - \tilde{\omega}) \\ &+ e^2 e'^2 f_{17}\cos(2\tilde{\omega}' - 2\tilde{\omega}) + e^3 f_{82}\cos(4\lambda' - \lambda - 3\tilde{\omega}) \\ &+ e^2 e' f_{83}\cos(4\lambda' - \lambda - \tilde{\omega}' - 2\tilde{\omega}) + ee'^2 f_{84}\cos(4\lambda' - \lambda - 2\tilde{\omega}' - \tilde{\omega}) + e'^3 f_{85}\cos(4\lambda' - \lambda - 3\tilde{\omega}'))) \\ &+ \frac{1}{\alpha}(-\frac{1}{3}e'^3\cos(4\lambda' - \lambda - 3\tilde{\omega}')) + \mathscr{O}(e^5)\end{aligned} \tag{A.22}$$

when applying the same methods as before, the equations of motion become

$$\begin{aligned}\frac{\mathrm{d}n}{\mathrm{d}t} = \frac{3n'^2 m'}{\alpha^2 M}\Big(&f_{82}e^3\sin(-4\lambda' + \lambda + 3\tilde{\omega}) + f_{83}e^2 e'\sin(-4\lambda' + \lambda + \tilde{\omega}' + 2\tilde{\omega}) \\ &+ f_{84}ee'^2\sin(-4\lambda' + \lambda + 2\tilde{\omega}' + \tilde{\omega}) + f_{85}e'^3\sin(-4\lambda' + \lambda + 3\tilde{\omega}') \\ &+ \alpha\left(-\frac{16}{3}e'^3\right)\sin(-4\lambda' + \lambda + 3\tilde{\omega}')\Big) + \mathscr{O}(e^5)\end{aligned} \tag{A.23}$$

$$\begin{aligned}\frac{\mathrm{d}n'}{\mathrm{d}t} = -\frac{12n'^2 m'}{\alpha M}\Big(&\alpha\left(f_{82}e^3\sin(-4\lambda' + \lambda + 3\tilde{\omega}) + f_{83}e^2 e'\sin(-4\lambda' + \lambda + \tilde{\omega}' + 2\tilde{\omega})\right. \\ &\left. + f_{84}ee'^2\sin(-4\lambda' + \lambda + 2\tilde{\omega}' + \tilde{\omega}) + f_{85}e'^3\sin(-4\lambda' + \lambda + 3\tilde{\omega}')\right) \\ &+ \frac{1}{\alpha}\left(-\frac{1}{3}e'^3\right)\sin(-4\lambda' + \lambda + 3\tilde{\omega}')\Big) + \mathscr{O}(e^5)\end{aligned} \tag{A.24}$$

$$\begin{aligned}\frac{\mathrm{d}p}{\mathrm{d}t} = -\frac{im'n'^2}{n\alpha^2 M}\Big(&\left(f_{10}e' + f_{11}e^2 e' + f_{12}e'^3\right)\exp -i\tilde{\omega}' \\ &+ 2f_{17}ee'^2\exp -2i\tilde{\omega}'\exp i\tilde{\omega} \\ &+ 3f_{82}e^2\exp i(-4\lambda' + \lambda)\exp 2i\tilde{\omega} \\ &+ 2f_{83}ee'\exp -i(-4\lambda' + \lambda)\exp i\tilde{\omega}'\exp i\tilde{\omega} \\ &+ f_{84}e'^2\exp i(-4\lambda' + \lambda)\exp 2i\tilde{\omega}'\Big) \\ &+ \mathscr{O}(e^5)\end{aligned} \tag{A.25}$$

$$\begin{aligned}\frac{\mathrm{d}p'}{\mathrm{d}t} = -\frac{imn'}{M}\Big(&\left(f_{10}e + f_{11}e^3 + f_{12}ee'^2\right)\exp -i\tilde{\omega} + \\ &+ 2f_{17}e^2 e'\exp -2i\tilde{\omega}\exp i\tilde{\omega}' \\ &+ f_{83}e^2\exp i(-4\lambda' + \lambda)\exp 2i\tilde{\omega} \\ &+ 2f_{84}ee'\exp i(-4\lambda' + \lambda)\exp 2i\tilde{\omega}\exp i\tilde{\omega}' \\ &+ 3f_{85}e'^2\exp i(-4\lambda' + \lambda)\exp 2i\tilde{\omega}' \\ &+ \frac{3}{\alpha^2}\left(-\frac{1}{3}e'^2\right)\exp i(-4\lambda' + \lambda)\exp 2i\tilde{\omega}'\Big) \\ &+ \mathscr{O}(e^5)\end{aligned} \tag{A.26}$$

Again a different set of Laplace coefficients is required in these sets of equations. Due to the increased order

of the resonance, the terms that are in $\mathcal{O}(e^4)$ and lower are limited, and the number of factors is small:

$$\begin{aligned}
f_{82} &= \frac{1}{48}\left[-26j+30j^2-8j^3-9\alpha D+27j\alpha D\right.\\
&\quad\left.-12j^2\alpha D+6\alpha^2D^2-6j\alpha^2D^2-\alpha^3D^3\right]A_j\\
f_{83} &= \frac{1}{16}\left[-9+31j-30j^2+8j^3+9\alpha D-25j\alpha D\right.\\
&\quad\left.+12j^2\alpha D-5\alpha^2D^2+6j\alpha^2D^2+\alpha^3D^3\right]A_{j-1}\\
f_{84} &= \frac{1}{16}\left[8-32j+30j^2-8j^3-8\alpha D+23j\alpha D\right.\\
&\quad\left.-12j^2\alpha D+4\alpha^2D^2-6j\alpha^2D^2-\alpha^3D^3\right]A_{j-2}\\
f_{85} &= \frac{1}{48}\left[-6+29j-30j^2+8j^3+6\alpha D-21j\alpha D\right.\\
&\quad\left.+12j^2\alpha D-3\alpha^2D^2+6j\alpha^2D^2+\alpha^3D^3\right]A_{j-3}
\end{aligned} \quad \text{(Murray and Dermott, 1999, Tab. B.15.).} \tag{A.27}$$

A.2.3. Verification: Coefficients and Behaviour

As mentioned in subsection A.2.2, the 4:1 resonance is included, but not considered further. As such, the behaviour of only the 2:1 and 3:1 resonances are examined here. First, the Laplace coefficients are discussed, after which it is checked whether libration of the resonant angles can be achieved. Finally, the periodic behaviour of the orbital elements is presented.

Laplace Coefficients

For the 2:1 resonance, a range of coefficients —though not all that are used in this study— is given in Yoder and Peale (1981, Eq. 12), while only the first-order resonant terms are further considered in their study, corresponding to C_1 and C_2. As such, the other factors are unnamed. The comparison to the factors resulting from the code can be found in Table A.4. While the numbers resulting from the code are far more precise, it can be seen that their rounded values correspond to the factors given in the reference.

Table A.4: Comparison of coefficients resulting from the model, and the coefficients given in Yoder and Peale (1981, Eq. 12) at α=0.63.

Reference		**Code**	
-	-0.58	f_{10}	-0.575888920189879
C_1	-1.19	f_{27}	-1.19070021551407
-	-0.20	f_{28}	-0.197495820381562
-	0.87	f_{29}	0.865967316132110
C_2	0.43	$f_{31}-2\alpha$	0.428499784003556
-	2.20	$f_{32}+\alpha$	2.19729922950788
-	1.17	$f_{33}+\frac{3}{2}\alpha$	1.17234418284710

Moving on to the 3:1 resonance, a number of coefficients, but again not all that are used in this thesis, are presented in Murray and Dermott (1999, Tab. 6.1). The factors presented in Equation A.20 that correspond to A_3, A_5, A_6, and A_7 given in the table are shown in Table A.5. Similarly to the Laplace coefficients of the 2:1 resonance, the ones resulting from the code are more precise, but are the same as those in Murray and Dermott when rounded.

Table A.5: Comparison of coefficients resulting from the model, and the coefficients given in Murray and Dermott (1999, Tab. 6.1) at α=0.480597.

Reference		**Code**	
A_3	-0.165406	f_{10}	-0.165406261739014
A_5	0.598100	f_{45}	0.598100077365647
A_6	-2.21124	f_{49}	-2.21124340097412
A_7	0.362954	$f_{53}-\frac{27}{8}\alpha$	0.362954177472744

Resonant Angles

When resonance is reached, the angles corresponding to that resonance should start to librate, rather than circulate. These angles, for the 2:1 resonance, are $2\lambda' - \lambda - \tilde{\omega}$ and $2\lambda' - \lambda - \tilde{\omega}'$, while for the 3:1 resonances these are $3\lambda' - \lambda - 2\tilde{\omega}$, $3\lambda' - \lambda - 2\tilde{\omega}'$, and $3\lambda' - \lambda - \tilde{\omega}' - \tilde{\omega}$. For the 2:1 resonances, it was found that generally both angles librate simultaneously. This is not the case for the 3:1 resonance, however, for which resonant conditions are more difficult to achieve. This will be discussed further in subsection A.2.4 and A.2.5. Note that in order to yield libration of the 3:1 resonant angles, the oblateness modifications mentioned in subsection A.2.4 have already been applied. While no conditions were found for which $3\lambda' - \lambda - 2\tilde{\omega}$ or $3\lambda' - \lambda - 2\tilde{\omega}'$ are librating, several conditions resulted in libration of $3\lambda' - \lambda - \tilde{\omega}' - \tilde{\omega}$. This behaviour is shown in Figure A.4.

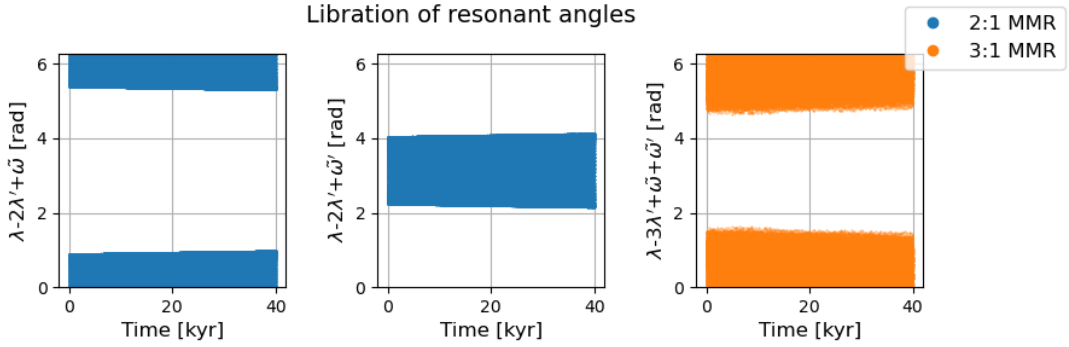

Figure A.4: Libration of resonant angles about 0 or π. The first two correspond to the 2:1 resonance (condition 4 in Tab. C.1 of the paper), while the last to the 3:1 resonance (condition 2 in Tab. C.2 of the paper) with $|\mathrm{Im}(k_{2,p})| = 1 \cdot 10^{-5}$.

Periodic Behaviour

Due to the inclusion of smaller changes, the periodic behaviour of the solutions can be examined. The variation of the elements now depends on $\exp(iV_1)$, $\exp(-i\omega)$, and $\exp(-i\omega')$. The first results in short-period oscillations, while the latter two correspond to long-period secular changes. The most dominant should be the natural frequency of $v/2\pi$ (Yoder and Peale, 1981), resulting from $\exp(iV_1)$, since $\dot{V}_1 = v$. When first analysing the frequencies present in the 2:1 solution, as shown in the top two plots of Figure A.5, it is clear that there is indeed a peak at this frequency. When examining the 3:1 resonance, presented on the bottom row, it can also be seen that the strongest peak is at the natural frequency. However, there are a variety of peaks present in the surrounding frequencies, showing that the 3:1 resonance is generally weaker and more chaotic.

A.2.4. Validation: Comparison to Rovira-Navarro et al. (2020) & Dermott et al. (1988)

For the 2:1 resonance, the results are checked directly with a reference run using the original model of Rovira-Navarro et al. (2021), as this is readily available. The 3:1 resonance will be compared qualitatively against some of the behaviour shown in Dermott et al. (1988).

2:1 MMR

The code of Rovira-Navarro et al. (2021) uses equations accurate up to second-order to find the evolution of the orbit. The combined tidal and resonance equations (Eqs. 25a-c and 26) from Rovira-Navarro et al. for a 2:1 MMR are:

$$\frac{\mathrm{d}n}{\mathrm{d}t} = \frac{n}{\tau_n} + \frac{e^2 n}{\tau_e}\left(\left(3+\frac{57}{7}\right) + 3\frac{\tau_e}{\tau_{e'}}\frac{m}{m'}\left(\frac{C_2}{C_1}\right)^2 \alpha^{1/2}\right) + 3\frac{m'}{M}\alpha\left(\frac{n}{v}\right)^2 \dot{v}\left(C_1 e - C_2 e'\right), \tag{A.28}$$

$$(1+K(e,e'))\,\dot{v} = n\left[\frac{1}{\tau_n}\left(1-\frac{\tau_n}{\tau_{n'}}\right) + \frac{e^2}{\tau_e}\left(\left(3+\frac{57}{7}\right) + 12\frac{m}{m'}\alpha^2 + \frac{\tau_e}{\tau_{e'}}\left(\frac{m}{m'}\right)^2\left(\frac{C_2}{C_1}\right)^2\left(2\left(6-\frac{57}{7}\right)\alpha^{5/2} + 3\frac{m'}{m}\alpha^{1/2}\right)\right)\right], \tag{A.29}$$

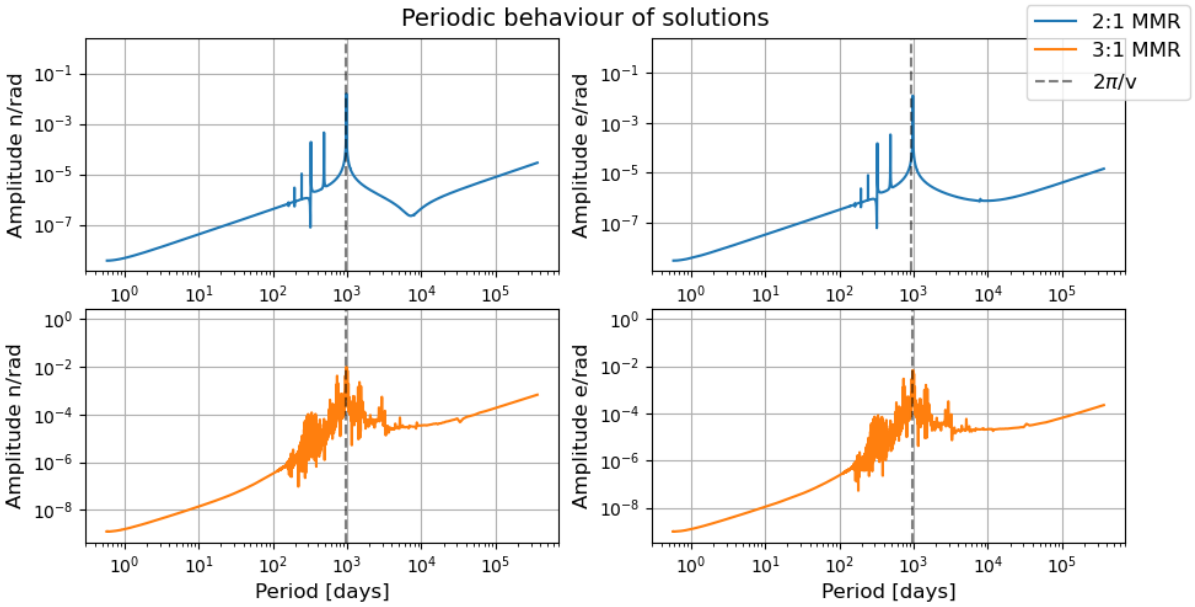

Figure A.5: Fourier analysis of the evolution of the mean motion (left) and eccentricity (right) as a result of the higher order MMR equations. The most dominant peaks correspond to the natural frequency of $\nu/2\pi$. The 3:1 resonance is weaker, and shows a more chaotic distribution around the dominant frequency. Again, condition 4 in Tab. C.1 of the paper was used for the 2:1 resonance, and the condition 2 for the 3:1 resonance in Tab. C.2 with $|\mathrm{Im}(k_{2,p})| = 1 \cdot 10^{-5}$.

where the accent $'$ indicates it is a property of the outer moon, $C_1 = -1.19$ and $C_2 = 0.43$ (Yoder and Peale, 1981),

$$\begin{aligned} K(e,e') = -6\frac{M}{m'}\frac{1}{C_1}\left[\alpha^{1/2} + \left(\frac{C_2}{C_1}\right)^2 \frac{m}{m'}\alpha\right] e^3 \\ +12\frac{M}{m}\frac{1}{C_2}\left[1 + \left(\frac{C_1}{C_2}\right)^2 \frac{m'}{m}\alpha^{-1/2}\right] e'^3 \end{aligned}, \tag{A.30}$$

and

$$\begin{aligned} e &= -\frac{m'}{M}\frac{n}{\nu}\alpha C_1 \\ e' &= \frac{m}{M}\frac{n}{\nu}\alpha^{3/2} C_2 \end{aligned}. \tag{A.31}$$

When running the new equations and comparing them to the results from Equation A.28 to A.31, the results presented in Figure A.6 are found. While the general trend of the orbital elements remains the same, high-frequency oscillations are now included as well. The previous method used simpler equations which allowed for averaging of the changes, but the more complicated relations used here did not allow for this treatment. Note that α is kept at a constant value of 0.63, to match the assumed value in Rovira-Navarro et al. (2021) and yield the same behaviour. The first set of initial conditions in Tab. C.1 of the paper were used here, making sure to place the initial conditions of the reference around the mean of n, e, and ν, resulting in $n = 2.9919332610813467 \cdot 10^{-5}$ rad/s, $e = 0.0089885565637483$, and $\nu = 1.2006207887376313 \cdot 10^{-7}$ rad/s. The initial e' is then found using Equation A.31, with the remaining conditions as presented in Table A.1. While the oscillations are significant, the general trend is the same as the reference.

3:1 MMR

Here two scenarios were explored: one where the moons are relatively close to the planet, and one where the moons were placed farther away, with otherwise random initial conditions. The former results in the behaviour shown in Figure A.7, while the latter in Figure A.8.

When placed closer to the planet, it seems to be easier to achieve resonance, and the resonances are already better separated. While the motion is still preceded by a chaotic period, where the elements switch between different resonances, the angles librate for a longer period of time after. This is similar to the behaviour

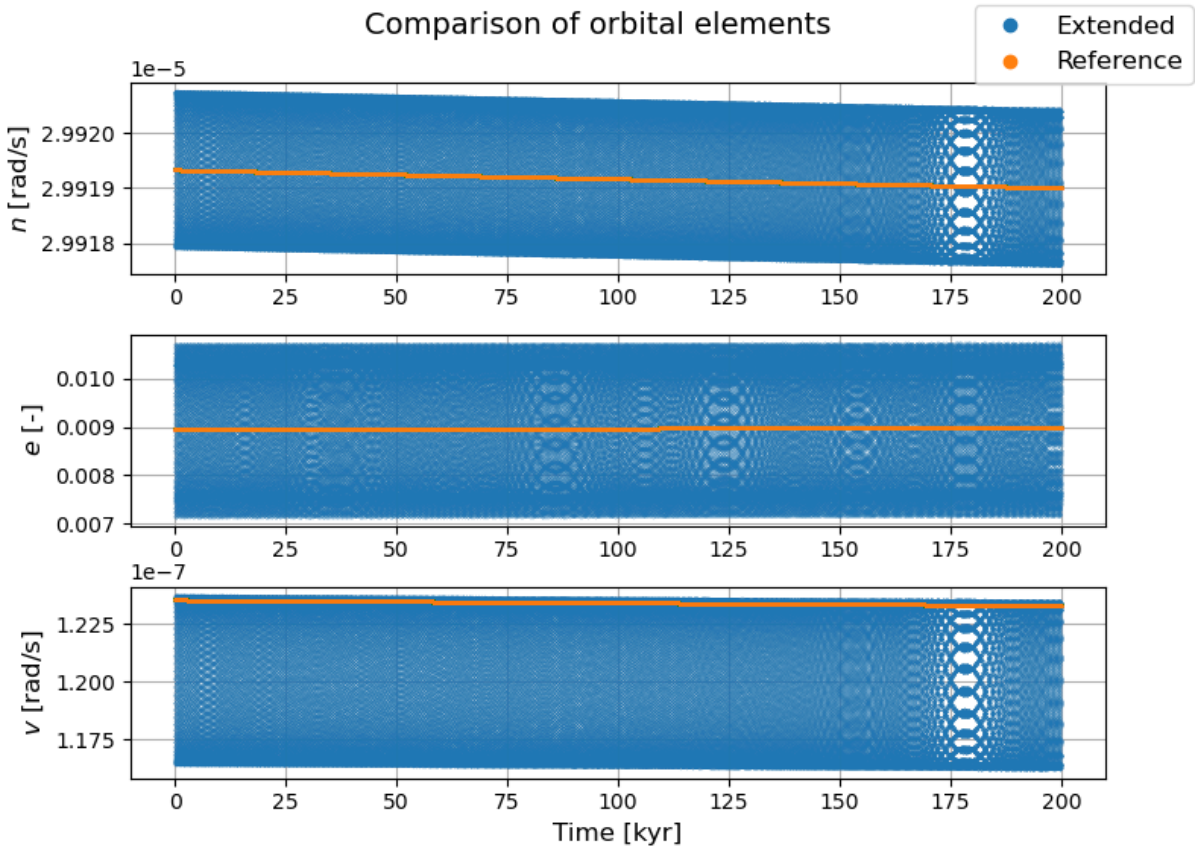

Figure A.6: Comparison of orbital elements resulting from the original code, and the inclusion of higher order terms. Low period oscillations are now included, but the overall trend remains the same.

presented in Fig 11. of Dermott et al. (1988), where they have included a sufficiently large J_2 to separate the resonances. Note that this has not yet been applied here.

When moving away from the planet, this quickly changes. Figure A.8 shows behaviour similar to Fig. 12 and 14 in Dermott et al. (1988), where the elements jump between different resonances, but none hold. This indicates that at farther distances the resonances are not well separated for the approximately Jupiter- and Io-mass planet and moons considered here. This is in line with Dermott et al., who show that for a constant J_2 a sufficient degree of separation is more likely to be reached at smaller a, since it is inversely proportional. However, due to this added difficulty, the oblateness as proposed by Dermott et al. will be used further. Using Eq. 15 from Yoder and Peale (1981), previously presented in Eq. 18 of the paper, the oblateness is included in Eq. 17. Adding these terms allows for resonance farther from the planet, as presented in Figure A.9, using initial conditions #4 in Tab. C.2 of the paper.

A.2.5. Exploration of Initial Conditions

To make sure that the systems considered are already in resonance at the start of integration, initial conditions were generated that exhibited the correct behaviour. For the 2:1 MMR this process is relatively straightforward, as the capture probability for these cases is high. However, finding the correct conditions for the 3:1 resonance required more work. Here, the method used to speed up the process for the generation of initial conditions for the 2:1 MMR are described first, after which the 3:1 MMR is treated.

2:1 MMR

As mentioned above, finding resonant conditions for the 2:1 resonance is relatively straightforward. As long as the eccentricity remains sufficiently small and the integration time is long enough, eventually resonance will be reached. In order to speed up this process, the method of scaling Q is used. Scaling the values of Q for the planet and the moon can allow for evaluating the problem over longer timescales. Due to the extended run time of the model, a limited amount of time can be examined, a problem that may be overcome using this scaling method. However, the examined situation must adhere to the following conditions:

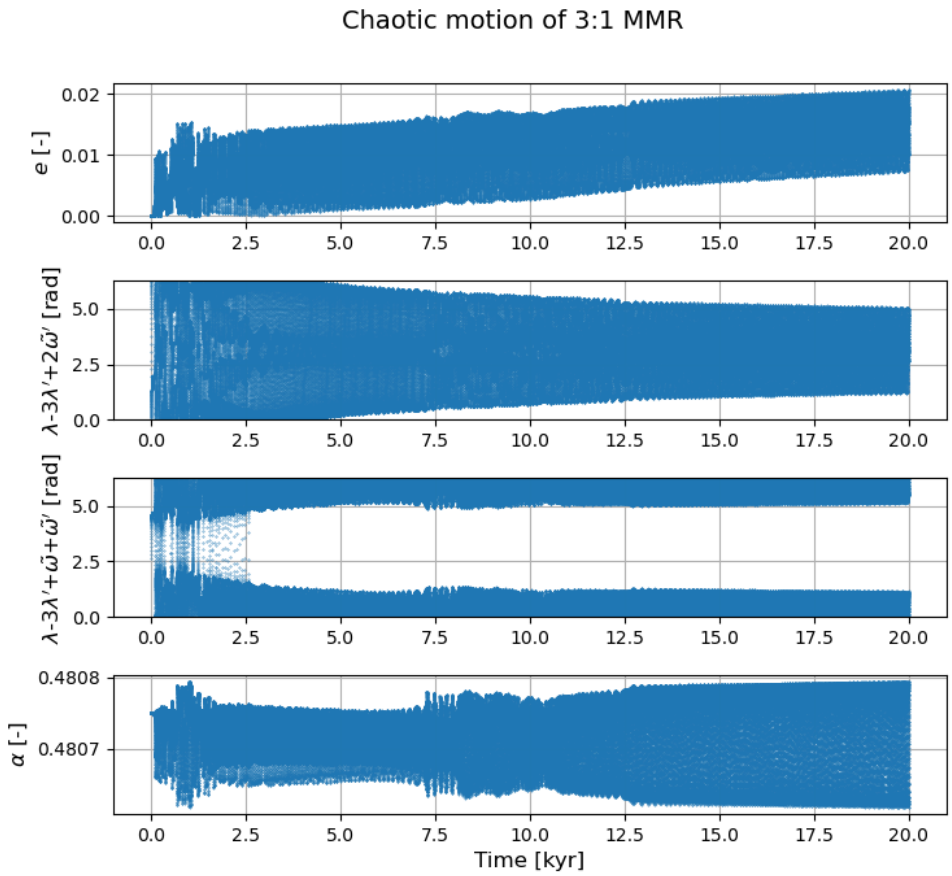

Figure A.7: Behaviour of the 3:1 resonance when relatively close to the planet ($n = 1.0778 \cdot 10^{-4}$ rad/s). After a period of chaotic motion, the angles start to librate.

1. Only the timescale is changed (Lari et al., 2020);
2. After chaotic motion, the statistics are unchanged (Lari et al., 2020);
3. Change in a due to tides must be significantly smaller than the amplitude of the oscillations due to resonance (Dermott et al., 1988).

The scaling is done as follows. First of all, the real time examined is equal to the time of the model multiplied by a factor C:

$$t \approx C\tilde{t}. \tag{A.32}$$

In order to achieve this, the $\mathrm{Im}(k_2)$ values of planet and moon are also multiplied by C. This is simplified by

$$\begin{aligned} \left(\frac{\mathrm{d}n}{\mathrm{d}t}\right)_T &= C\left(\frac{\mathrm{d}n}{\mathrm{d}\tilde{t}}\right)_T, \\ \left(\frac{\mathrm{d}e}{\mathrm{d}t}\right)_T &= C\left(\frac{\mathrm{d}e}{\mathrm{d}\tilde{t}}\right)_T. \end{aligned} \tag{A.33}$$

The results for a variety of C values can be found in Figure A.10, where the eccentricity is highlighted, but the outcome is similar for the other orbital elements. The behaviour of the scaling method is in agreement with the findings of Lari et al. (2020), who show that the scaling is very stable up to $C = 10^5$. The overall behaviour remains the same for the different scaling factors, the results are simply found in a shorter amount of time; in other words, only the timescale is changed, therefore adhering to the first condition mentioned above. Chaotic motion was not encountered, meaning that the second condition is irrelevant. Finally, not meeting the third condition results in deviations in behaviour, as will be shown in Section B.4, which is not the case here.

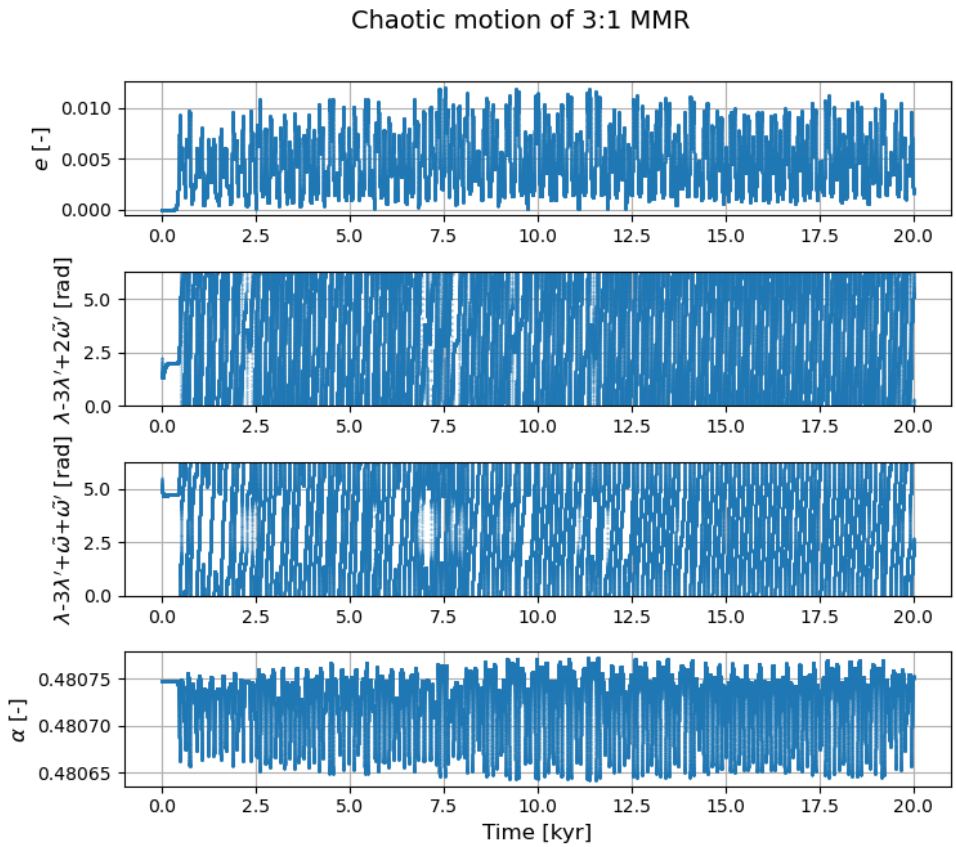

Figure A.8: Behaviour of the 3:1 resonance when farther from the planet ($n = 2 \cdot 10^{-5}$ rad/s). The elements are shown to "hop" between different resonances, and it becomes difficult to find conditions for which one holds.

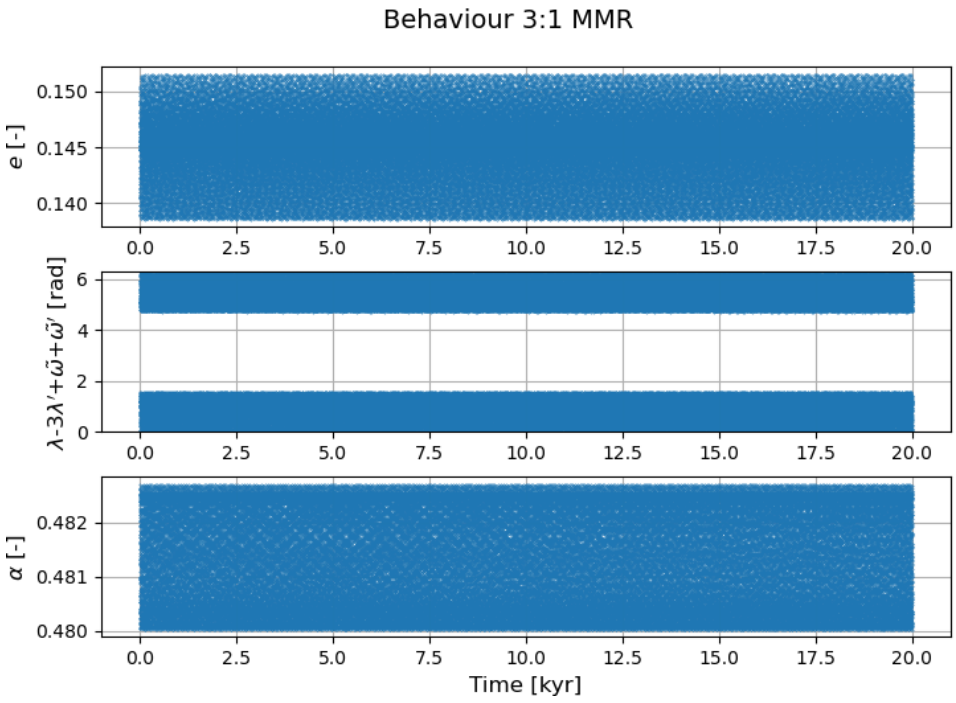

Figure A.9: Behaviour of the 3:1 resonance when farther from the planet, now including oblateness. The behaviour is much more periodic and stable, and one of the three resonant angles librates over a longer period of time.

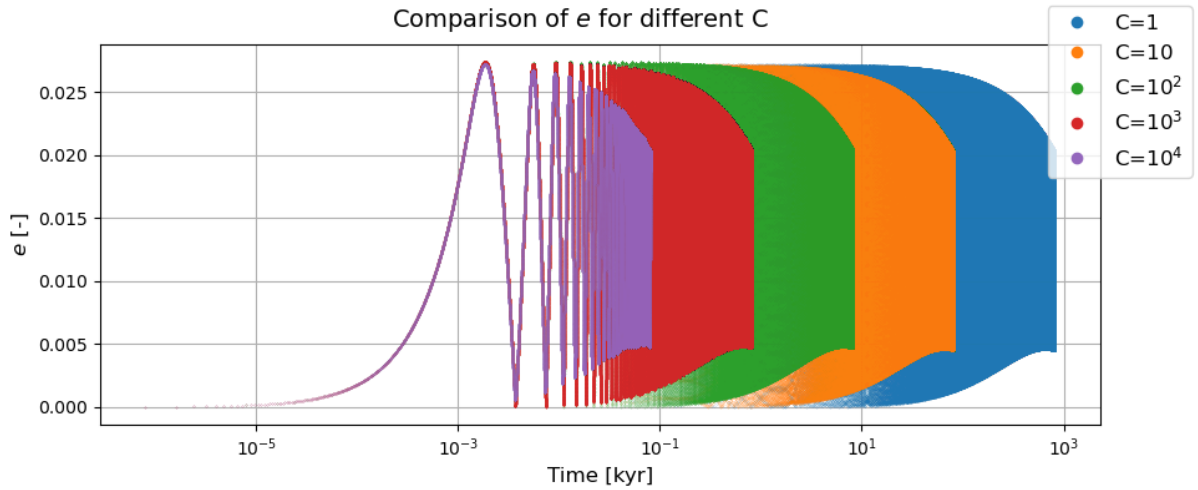

Figure A.10: Comparison of behaviour of e for different scaling factors C. For higher scaling factors the same results are found in a shorter amount of time, which approximately match the outcome for $C = 1$ when multiplied by C.

Since the method of scaling using Q is so robust, it was used to quickly find initial conditions corresponding to the 2:1 MMR. In the end, nine different sets of conditions for mean motions ranging from $3 \cdot 10^{-5}$ rad/s to $1 \cdot 10^{-5}$ rad/s were found. These sets can be found in Tab. C.1 of the paper, and have already been used in some parts of the preceding sections.

3:1 MMR

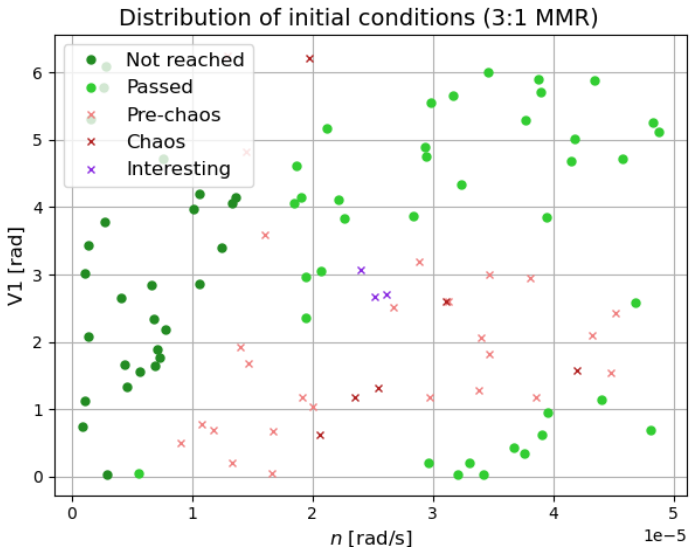

Figure A.11: Distribution of outcomes of random initial conditions. The green circles indicate areas that were not explored further, either due to the resonance not being reached, or because it was simply passed. The red crosses are areas that could still contain initial conditions for resonance, as they resulted either in chaotic behaviour, or behaviour that could become chaotic. The purple crosses are points for which the resonant angle $3\lambda' - \lambda - \tilde{\omega}' - \tilde{\omega}$ was librating at the end of the integration period.

While for the 2:1 MMR finding conditions of resonance is a matter of placing the two moons close enough and running the evolution for a sufficient amount of time (resulting in the sets of initial conditions in Tab. C.1 of the paper), the 3:1 resonance is subject to lower probabilities of capture (Borderies and Goldreich, 1984; Dermott et al., 1988). This means that choosing a random set of initial conditions may not result in the desired outcome. Therefore, a larger sample of random conditions was examined. The summary of the outcome of the behaviour is presented in Figure A.11. The best correlation between different types of behaviour and orbital elements was between n and V_1, where n was uniformly distributed between 0 and $5 \cdot 10^{-5}$ rad/s, and V_1 from 0 to 2π. The moons were placed at $v = 1 \cdot 10^{-11}$ rad/s, and therefore close, but not in, resonance. The other ranges of initial conditions can be found in Sec. 2.4 of the paper. The cases where the moons were placed rather far from the planet were not able to reach a sufficiently small v (left of the plot, darker green dots), while other cases moved quickly through resonance (lighter green dots). Neither of these cases were examined further. The crosses represent cases that either showed resonant behaviour, or could possibly show this after a bit more time. Therefore, this area was examined more closely, and four interesting cases were identified here. These initial conditions are presented in Tab. C.2 of the paper.

B

Resonance Locking

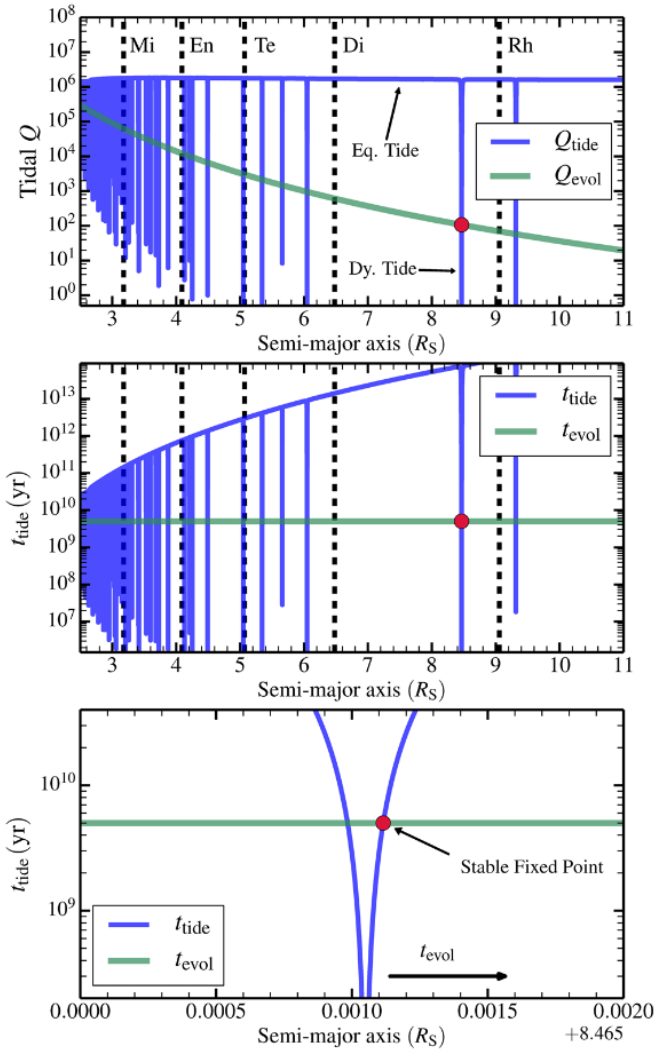

Figure B.1: Migration timescale and planetary Q change as a function of semi-major axis (Fuller et al., 2016, Fig. 1).

The final addition to the model is the resonance locking mechanism. It was originally proposed by Fuller et al. (2016), based on mechanisms likely to occur in stars (Ioannou and Lindzen, 1993a,b; Ogilvie and Lin, 2004). The mechanism affects the $|\mathrm{Im}(k_{2,p})|$ directly, and causes more rapid migration. The method of including this mechanism was already explained in Sec. 2.2 of the paper, but is elaborated upon in Section B.1 and verified in Section B.2. The flowchart of the model is presented in Section B.3. Finally, a possible scaling method is explored in Section B.4.

B.1. Modelling the Wave

The presence of the internal waves causes dips in the planetary Q at specific frequencies, as opposed to a constant Q in the entirety of the system. This pattern is presented in Fuller et al. (2016), and repeated here in Figure B.1. Note that Q_p and $\mathrm{Im}(k_{2,p})$ have the opposite effect, therefore peaks in $\mathrm{Im}(k_{2,p})$ are considered instead. In order to simulate the passage of such a wave through a moon's frequency, the shape is assumed to be gaussian, and the corresponding K_2 is calculated as defined in Eq. 9.

The modes evolve as the planet evolves. The timescale at which this occurs is likely similar to the age of the planet, and denoted by t_α and defined in Eq. 8 of the paper. Similarly, the rotational rate of the planet changes as time passes as well, at a timescale t_p which is assumed to be infinite (see Sec. 2.2 of the paper).

Looking back at Eq. A.1 of the paper, it can be seen that the most dominant term of the tidal migration equation depends on $K_2(2n - 2\dot{\theta}_p)$. Since for the giant planets $\dot{\theta}_p \gg n$, this

frequency is negative and results in a negative value for $\mathrm{Im}(k_{2,p})$. Therefore, it causes the outward migration of the moon (a decrease in n). Increasing this value $|\mathrm{Im}(k_{2,p})|$ results in the strongest increase in outward migration. Furthermore, since the spin rate of giant planets is generally expected to increase (Fuller et al., 2016; Lainey et al., 2020), the decrease in n and increase in $\dot{\theta}_p$ results in a growth in the absolute value of the frequency, similarly to ω_α. When the rate is such that the two are approximately equal, the moon will "ride the wave," and migrate outward at a rate similar to t_α. An illustration of this process was previously shown in Fig. 2 of the paper.

B.2. Verification: Expected Behaviour

Theoretically, including the resonance locking mechanism should have the following effects on the evolution of the system (Fuller et al., 2016):

1. The migration rate of the moon's tidal frequency should equal that of the wave;
2. When in an MMR, the migration rate of the outer moon should also be approximately equal to that of the wave;
3. Due to the transfer of angular momentum, the $|\mathrm{Im}(k_{2,p})|$ required to match the wave's migration rate becomes larger when in MMR.

Furthermore, from Eq. A.2 of the paper it can be seen that increasing the term $K_2(2n - 2\dot{\theta}_p)$ causes slightly stronger damping of the eccentricity due to tides. The $|\mathrm{Im}(k_{2,p})|$ required to lock with the wave was given in Fuller et al. (2016), and can be found using Eq. 22 of the paper. A comparison of the predicted value from

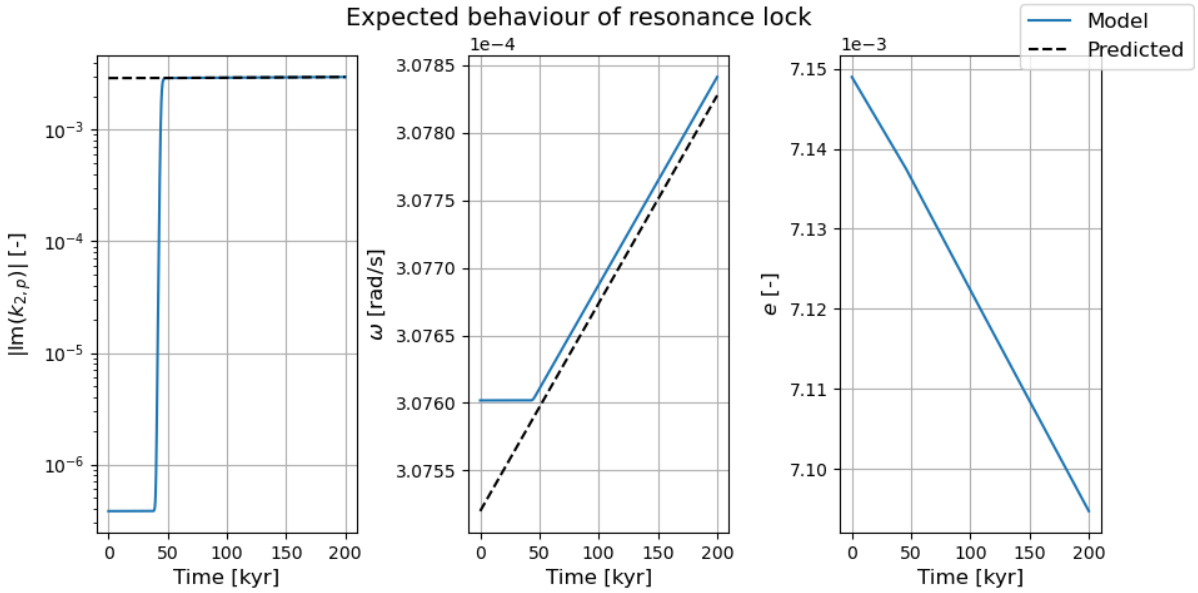

Figure B.2: Comparison of model results with predicted values when assuming a single moon affected by tides alone. The assumed t_α is 200 Myr, and $t_\alpha \ll t_p$. The initial n and e are from set 1 of Tab. C.1 of the paper.

Eq. 22 with the results from the model can be found in the first plot of Figure B.2, and shows that, after the equilibrium value on the wave is found, these two values are approximately equal. Similarly, once the moon is on the wave, its frequency will change at the same rate as ω_α, as visible in the second plot of Figure B.2, which is in line with point 1. above. Finally, the eccentricity should continue to be dampened by the tides. The final plot in Figure B.2 shows that this is indeed the case.

The second and third points related to the interactions with an MMR are examined in Figure B.3. The second effect states that the outer moon should migrate at the same faster rate as the inner moon. In the second and third plot of Figure B.3 it can be seen that, as the inner moon migrates faster, the outer moon slowly follows until it matches the migration rate of the inner moon. In order to achieve this, an appropriate increase in $|\mathrm{Im}(k_{2,p})|$ to accommodate for the shared angular momentum occurs, and the $|\mathrm{Im}(k_{2,p})|$ reached must be higher than that of a single moon (point 3.). In the first plot of Figure B.3, the results of both the tides

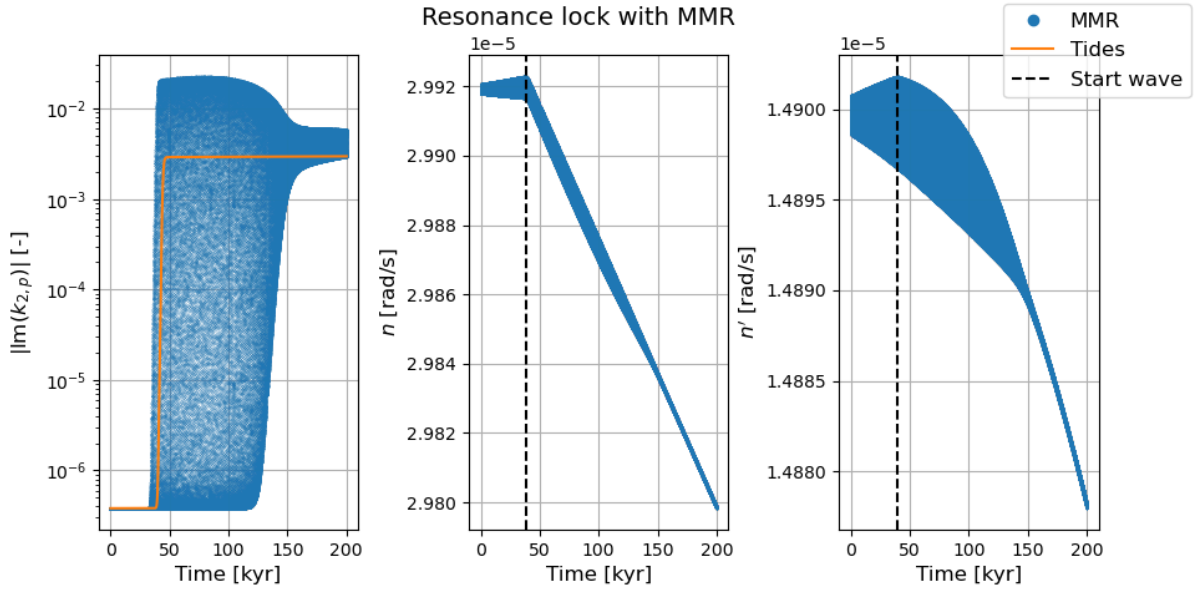

Figure B.3: Model results when assuming two moons in a 2:1 MMR affected by tides alone. The assumed t_α is 200 Myr, and $t_\alpha \ll t_p$. The initial conditions are set 1 of Tab. C.1 of the paper.

alone and the MMR are plotted. Clearly, the final value reached by the moons in MMR is higher than the value for the single moon.

Since the behaviour is as expected, the addition seems to work as it should. As it is a relatively new mechanism that has not been explored yet, no other references were found to compare the outcome to.

B.3. Model Flowchart

All adjustments made to the model have now been discussed. The flowchart of these extensions can be found in Figure B.4. The simplified flowchart of the original model by Rovira-Navarro et al. (2021) is presented on the left, where only *compute_tidal_dissipation* is shown in more detail since *calc_love* is needed in *update_orbit_extended* as well. Once the internal properties have been calculated, the orbit is integrated. In the *main* subroutine, first *calc_love* is called to find the Love number of the moon at $\omega = 2n$ in addition to $\omega = n$, see Eq. A.1 and A.2 of the paper. Once this is found, the required $b_s^{(j)}(\alpha)$ values are retrieved in *retrieve_bs* and the required derivatives $Db_s^{(j)}$ are calculated, provided that $\Delta\alpha > 10^{-6}$, as discussed in subsection A.2.1. From these, the coefficients of Equation A.4 and A.20 are found in *factor*. Then, the state as presented in Eq. 20 of the paper is integrated following Equation A.15 by finding the derivatives per step in *orbit_calc*. In case of resonance locking, *k2_planet* is called to find the $\mathrm{Im}(k_{2,p})$ per tidal frequency. Steps 9 through 17 are iterated until either the next step of the interior integration is reached, or the total time, depending on whether the change in the moon's interior properties is considered.

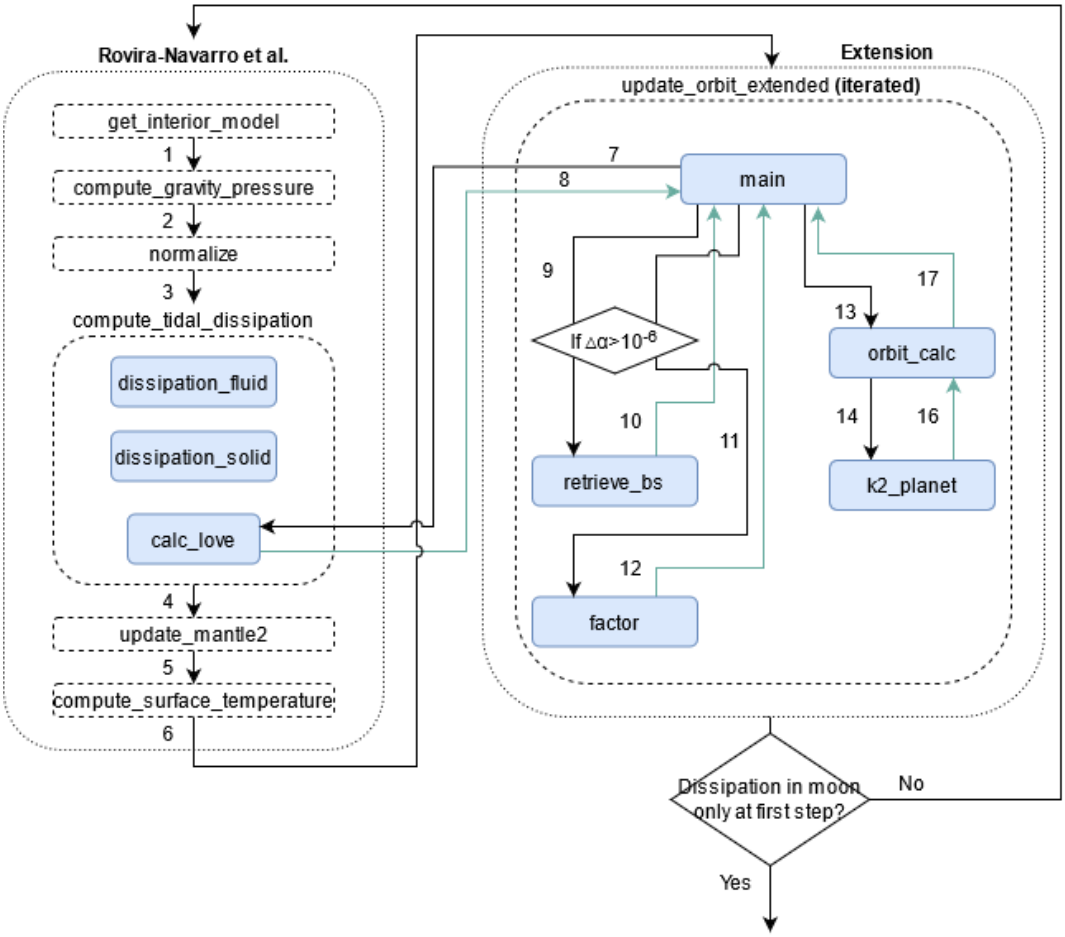

Figure B.4: Flowchart of the model extension. The blue boxes are subroutines. On the left the components of the original model are presented, with exception that the calculation of $k_{2,s}$ is now split. The Laplace coefficients (*retrieve_bs*) and corresponding coefficients (*factor*) are only found once $\Delta\alpha > 10^{-6}$. *main* and the other components are integrated until the final time. This final time is either the next step for the interior integration, or the end of the run.

B.4. Scaling *Q*

As discussed throughout Appendix A, the time period examined per run is much shorter than possible with the original code of Rovira-Navarro et al. (2021). In subsection A.2.5 a method to shorten the total run time was introduced, which worked well for the standard case without the resonance locking mechanism. In an attempt to overcome the run time problem, this method was tested when including the resonance lock as well.

In addition to the adjustments described in subsection A.2.5, the timescales associated with the migration of the wave are multiplied by this factor C. The increase in peak height is already achieved by applying Equation A.33, and requires no further alterations. Therefore,

$$\begin{aligned} t_\alpha &= C\tilde{t}_\alpha, \\ t_p &= C\tilde{t}_p. \end{aligned} \tag{B.1}$$

While previously approximately the same behaviour was found when scaling Q (see Figure A.10), introducing the resonance lock causes a different outcome. This sudden large decrease in migration timescale causes the change in semi-major axis due to tides to be closer to the amplitude of the oscillations (criterion 3 in subsection A.2.5), and the scaling method becomes invalid rather quickly. First, small changes in behaviour can be seen for $t_\alpha = 10$ Myr in the second plot in Figure B.5. For $t_\alpha = 1$ Myr the behaviour changes more rapidly and drastically, as shown in the first plot of Figure B.5. While these timescales are extremely low, one of the goals is to experiment with a variety of values to examine what may be required to break resonance. Since the behaviour is more heavily dependent on the scaling factor than the case without resonance locking,

it will not be applied when a wave is included.

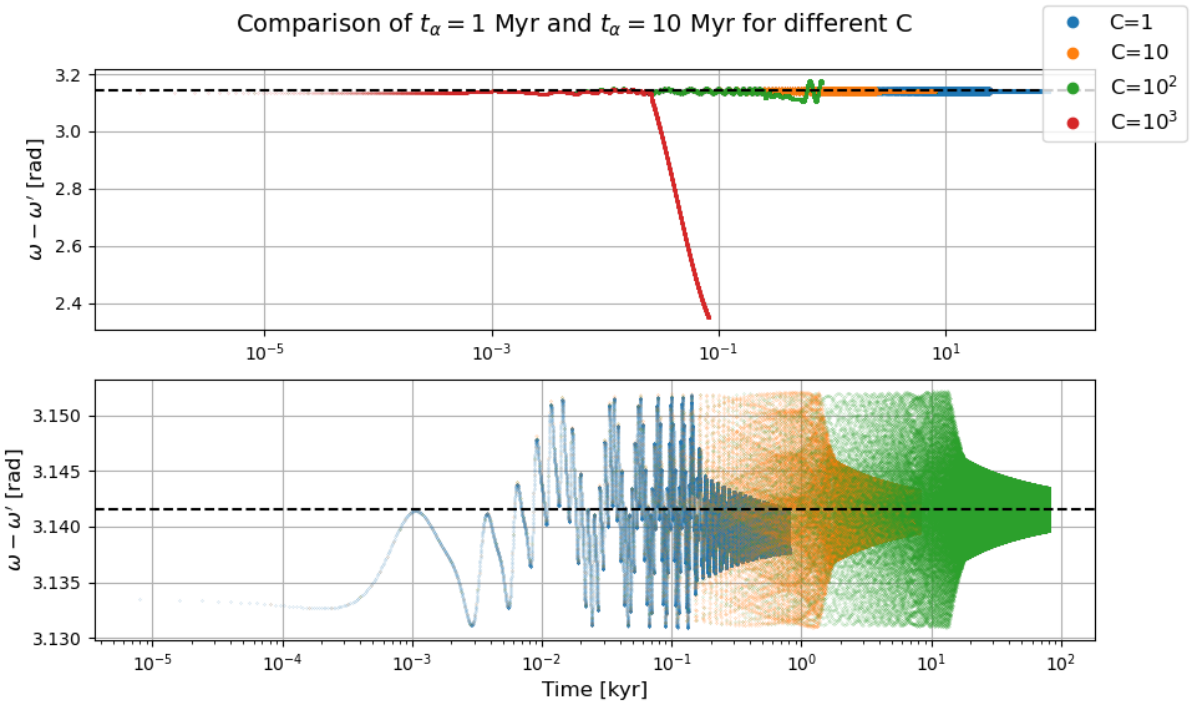

Figure B.5: Behaviour of $\omega - \omega'$ for various scaling factors (C), when considering a wave with $t_\alpha = 1$ Myr (top) and $t_\alpha = 10$ Myr (bottom). The behaviour already changes for $C = 10^2$, and the scaling method is not stable enough to be applied.

Bibliography

N. Borderies and P. Goldreich. A simple derivation of capture probabilities for the J+1:J and J+2:J orbit-orbit resonance problems. *Celest. Mech. Dyn. Astron.*, 32:127–136, 1984.

G. Boué and M. Efroimsky. Tidal evolution of the Keplerian elements. *Celest Mech Dyn Astr*, 131(30), 2019. doi: 10.1007/s10569-019-9908-2.

D. Brouwer and G. M. Clemence. *Methods of Celestial Mechanics*. Academic Press, 1961. ISBN 978-1-4832-0075-0. doi: 10.1016/C2013-0-08160-1.

A. Celletti, F. Paita, and G. Pucacco. The dynamics of Laplace-like resonances. *Chaos*, 29, 2019. doi: 10.1063/1.5087253.

S. F. Dermott, R. Malhotra, and C. D. Murray. Dynamics of the Uranian and Saturnian Satellite Systems: A Chaotic Route to Melting Miranda? *Icarus*, 76:295–334, 1988. doi: 10.1016/0019-1035(88)90074-7.

J. Fuller, J. Luan, and E. Quataert. Resonance locking as the source of rapid tidal migration in the Jupiter and Saturn moon systems. *MNRAS*, 458:3867–3879, 2016. doi: 10.1093/mnras/stw609.

P. Goldreich. An Explanation of the Frequent Occurrence of Commensurable Mean Motions in the Solar System. *MNRAS*, 130(3):159–181, 1965. doi: 10.1093/mnras/130.3.159.

P. Goldreich and S. Soter. Q in the Solar System. *Icarus*, 5:375–389, 1966. doi: 10.1016/0019-1035(66)90051-0.

J. Hillier and S. W. Squyres. Thermal Stress Tectonics on the Satellites of Saturn and Uranus. *J. Geophys. Res.*, 96(E1):15665–15674, 1991. doi: 10.1029/91je01401.

H. Hussmann and T. Spohn. Thermal-orbital evolution of Io and Europa. *Icarus*, 171:391–410, 2004. doi: 10.1016/j.icarus.2004.05.020.

H. Hussmann, G. Choblet, V. Lainey, D. L. Matson, Ch. Sotin, G. Tobie, and T. Van Hoolst. Implications of Rotation, Orbital States, Energy Sources, and Heat Transport for Internal Processes in Icy Satellites. *Space Sci Rev*, 153:317–348, 2010. doi: 10.1007/s11214-010-9636-0.

P. J. Ioannou and R. S. Lindzen. Gravitational Tides in the Outer Planets. I. Implications of Classical Tidal Theory. *ApJ*, 406:252–265, 1993a. doi: 10.1086/172437.

P. J. Ioannou and R. S. Lindzen. Gravitational Tides in the Outer Planets. II. Interior Calculations and Estimation of the Tidal Dissipation Factor. *ApJ*, 406:266–278, 1993b. doi: 10.1086/172438.

V. Lainey, R. A. Jacobson, R. Tajeddine, N. J. Cooper, C. Murray, V. Robert, G. Tobie, T. Guillot, S. Mathis, F. Remus, J. Desmars, J.-E. Arlot, J.-P. De Cuyper, V. Dehant, D. Pascu, W. Thuillot, Ch. Le Poncin-Lafitte, and J.-P. Zahn. New constraints on Saturn's interior from Cassini astrometric data. *Icarus*, 281:286–296, 2017. doi: 10.1038/s41550-020-1120-5.

V. Lainey, L. Gomez Casajus, J. Fuller, M. Zannoni, P. Tortora, N. Cooper, C. Murray, D. Modenini, R. S. Park, V. Robert, and Q. Zhang. Resonance locking in giant planets indicated by the rapid orbital expansion of Titan. *Nat. Astron.*, 2020. doi: 10.1038/s41550-020-1120-5.

G. Lari, M. Saillenfest, and M. Fenucci. Long-term evolution of the Galilean satellites: the capture of Callisto into resonance. *A&A*, 639(A40), 2020. doi: 10.1051/0004-6361/202037445.

A. E. H. Love. The Yielding of the Earth to Disturbing Forces. *Proc. R. Soc. Lond.*, 82(551):73–88, 1909. doi: 10.1098/rspa.1909.0008.

J. Luan and P. Goldreich. Classification of Satellite Resonances in the Solar System. *The Astronomical Journal*, 153(1), 2016. doi: 10.3847/1538-3881/153/1/17.

R. Malhotra. Orbital resonances in planetary systems. In *UNESCO-EOLSS*. Eolss Publishers, Paris, France, 2012. URL `https://www.eolss.net`. Revised in 2017.

C. D. Murray and S. F. Dermott. *Solar System Dynamics*. Cambridge University Press, Cambridge, UK, 1999. ISBN 0-521-57297-4.

G. I. Ogilvie and D. N. C. Lin. Tidal dissipation in rotating giant planets. *ApJ*, 610(1):477–509, 2004. doi: 10.1086/421454.

G. W. Ojakangas and D. J. Stevenson. Episodic Volcanism of Tidally Heated Satellites with Application to Io. *Icarus*, 66(2):341–358, 1986. doi: 10.1016/0019-1035(86)90163-6.

R.T. Pappalardo, M.J.S. Belton, H.H. Breneman, M.H. Carr, C.R. Chapman, G.C. Collins, T. Denk, S. Fagents, P.E. Geissler, B. Giese, R. Greeley, R. Greenberg, J.W. Head, P. Helfenstein, G. Hoppa, S.D. Kadel, K.P. Klaasen, J.E. Klemaszewski, K. Magee, A.S. McEwen, J.M. Moore, W.B. Moore, G. Neukum, C.B. Phillips, L.M. Prockter, G. Schubert, D.A. Senske, R.J. Sullivan, B.R. Tufts, E.P. Turtle, R. Wagner, and K.K. Williams. Does Europa have a subsurface ocean? Evaluation of the geological evidence. *J. Geophys. Res. Planets*, 104(E10):24015–24055, 1999. doi: 10.1029/1998JE000628.

S. J. Peale. Origin and Evolution of the Natural Satellites. *Annu. Rev. Astron. Astrophys.*, 37:533–602, 1999. doi: 10.1146/annurev.astro.37.1.533.

S. J. Peale, P. Cassen, and R. T. Reynolds. Melting of Io by Tidal Dissipation. *Science*, 203(4383):892–894, 1979. doi: 10.1126/science.203.4383.892.

G. Peterson, F. Nimmo, and P. Schenk. Elastic thickness and heat flux estimates for the uranian satellite Ariel. *Icarus*, 250:116–122, 2015. doi: 10.1016/j.icarus.2014.11.007.

W. Polycarpe, M. Saillenfest, V. Lainey, A. Vienne, B. Noyelles, and N. Rambaux. Strong tidal energy dissipation in Saturn at Titan's frequency as an explanation for Iapetus orbit. *A&A*, 619, 2018. doi: 10.1051/0004-6361/201833930.

J. P. Renaud and W. G. Henning. Increased Tidal Dissipation Using Advanced Rheological Models: Implications for Io and Tidally Active Exoplanets. *ApJ*, 857(2), 2018. doi: 10.3847/1538-4357/aab784.

M. Rovira-Navarro, W. Van der Wal, T. Steinke, and D. Dirkx. Tidally Heated Exomoons around Gas Giants. *Planet. Sci. J.*, 2(3), 2021. doi: 10.3847/PSJ/abf6cb.

G. Schubert, H. Hussmann, V. Lainey, D. L. Matson, W. B. McKinnon, F. Sohl, C. Sotin, G. Tobie, D. Turrini, and T. Van Hoolst. Evolution of Icy Satellites. *Space Sci Rev*, 153:447–484, 2010. doi: 10.1007/s11214-010-9635-1.

M. Segatz, T. Spohn, M. N. Ross, and G. Schubert. Tidal Dissipation, Surface Heat Flow, and Figure of Viscoelastic Models of Io. *Icarus*, 75(2):187–206, 1988. doi: 10.1016/0019-1035(88)90001-2.

W. C. Tittemore. Chaotic Motion of Europa and Ganymede and the Ganymede-Callisto Dichotomy. *Science*, 250(4978):263–267, 1990a. doi: 10.1126/science.250.4978.263.

W. C. Tittemore. Tidal Heating of Ariel. *Icarus*, 87(1):110–139, 1990b. doi: 10.1016/0019-1035(90)90024-4.

C. F. Yoder and S. J. Peale. The Tides of Io. *Icarus*, 47(1):1–35, 1981. doi: 10.1016/0019-1035(81)90088-9.